Master of Science Thesis

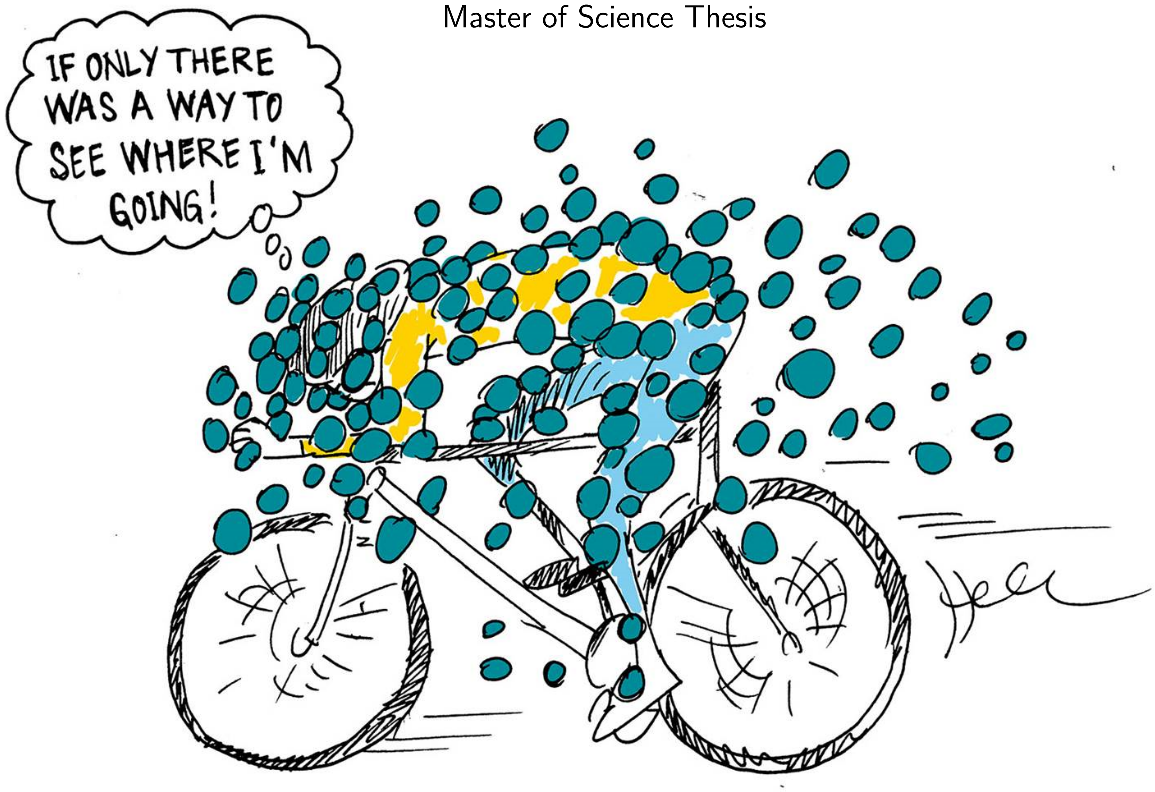

Aerodynamics of transiting objects via large-scale PIV - the Ring of Fire Concept

Alexander Spoelstra

October 24, 2017

Faculty of Aerospace Engineering

Delft University of Technology

Aerodynamics of transiting objects via large-scale PIV - the Ring of Fire Concept

Master of Science Thesis

To obtain the degree of Master of Science
at the Delft University of Technology,
to be defended publicly on Tuesday October 24, 2017 at 13:30 PM.

Alexander Spoelstra

October 24, 2017

Faculty of Aerospace Engineering · Delft University of Technology

Delft University of Technology

Front cover page image credits: Erwin Suvaal

DELFT UNIVERSITY OF TECHNOLOGY
DEPARTMENT OF AERODYNAMICS

The undersigned hereby certify that they have read and recommend to the Faculty of Aerospace Engineering for acceptance the thesis entitled **"Aerodynamics of transiting objects via large-scale PIV - the Ring of Fire Concept"** by **Alexander Spoelstra** in fulfillment of the requirements for the degree of **Master of Science**.

Dated: October 24, 2017

Thesis committee:

Prof. Dr. F. Scarano

Dr. A. Sciacchitano, supervisor

Dr. B. W. van Oudheusden

Ir. W. A. Nando Timmer

Ir. W. Terra, supervisor

Preface

This M.Sc. thesis concludes the Aerodynamics and Wind Energy master program at Delft University of Technology: faculty of Aerospace Engineering, and summarizes the research work that has been done during the thesis project. During the thesis I have been able to follow my interest for applied experimental aerodynamics and sports. I would to thank my supervisors Dr. Andrea Sciacchitano and Ir. Wouter Terra for giving me this opportunity as well as for involving me in the wind tunnel tests of Team Sunweb, the research exhibition at TU Delft and the production of the HFSB seeding system.

I am grateful to Prof. Scarano and all the members of the Large scale PIV group for including me in the group and providing their valuable inputs and assistance during the course of this thesis. I thank Toine Hooijen for his assistance during the experimental campaign.

Additionally, I would like to thank Peter Duyndam, Nico van Beek, Frits Donker, Dennis Bruikman, Henk-Jan Siemer, Colette Russo and rest of the support staff at the Aerodynamics Lab for all their aid.

Lastly, and most importantly I would like to thank my family for supporting me during my studies in Delft to become an engineer. Also I would like to thank all my friends for making my time in Delft very enjoyable. Thanks for all the great memories!

Alexander Spoelstra
Delft, The Netherlands
24th October, 2017

Abstract

Experimental aerodynamic studies in speed sports are conventionally performed by force balances or pressure taps to evaluate changes in aerodynamic drag due to geometry variations. In order to get a better understanding about the flow structures responsible for the generation of the drag force, in recent years the amount of aerodynamic studies that make use of local flow measurements increased, either by pressure probes or by particle based velocimetry. In case of the latter, the development of the neutrally buoyant Helium-Filled Soap Bubbles allows for much larger scattering cross-sections thus enabling even whole-field measurements (Scarano et al. (2015)). These experiments are typically conducted on stationary models in wind tunnels allowing accurate conditioning of the flow environment leading to repeatable measurements. Wind tunnel testing, however, can be expensive and technically challenging, for example when requiring a rolling floor. Furthermore, in the wind tunnel environment it is unfeasible to investigate the flow over an accelerating athlete or one that follows a curvilinear path.

The present work, therefore, introduces a new measurement system for in-field aerodynamic investigation in speed sports: the Ring of Fire. The approach makes use of large-scale stereoscopic particle image velocimetry (stereo-PIV), which provides the desired velocity information and allows to estimate the aerodynamic drag of the moving athlete by a control volume approach invoking the conservation of momentum (Terra et al. (2017)). In order to assess the practical implementation and accuracy of the proposed technique, experiments are conducted on a cyclist riding through a duct at a velocity of $8m/s$ measuring the flow before and after the passage of the rider in an area of $1000 \times 1700mm^2$.

Velocity statistics in the wake have been obtained from a set of ten passages of the athlete. The non-dimensional, phase-locked, time-averaged streamwise velocity fields show great similarity to the ones found in literature. The peak momentum deficit is comparable to the ones reported earlier and behind the stretched leg the amount of momentum deficit is larger than behind the raised leg. Furthermore, the vortices originating from the hips and thighs as well as from the feet are observed, which is in agreement with literature.

The drag force on the cyclist is computed from a control volume approach by utilising the flow field before and after passage of the athlete (van Oudheusden et al. (2007)) and is compared to balance measurements in the wind tunnel. Furthermore, the drag associated with variations in the athletes posture are compared. From five length scales in the wake onwards, the averaged drag area, obtained from ten individual runs, exhibits a rather constant value along the wake with an uncertainty of about 5%. The drag measured by the Ring of Fire does not directly match that the data from the balance measurements, which may be partly explained by differences in experimental setup. Conversely, the differences in drag associated with variations in the athletes posture are accurately estimated.

Table of Contents

List of Figures

List of Tables

Nomenclature

$2D-2C$	two dimensional and two component	-
$2D-3C$	two dimensional and three component	-
$3D-3C$	three dimensional and three component	-
$\bar{u}, \bar{v}, \bar{w}$	Time averaged velocity components	m/s
δ_z	Depth of Field	m
λ	Wavelength of laser light	m
μ	Dynamic viscosity of air	kg/ms
ν	Kinematic viscosity of air	m^2/s
ρ_f	Flow Density	kg/m^3
ρ_p	Tracer particle Density	kg/m^3
τ	Viscous stress	N/m^2
τ_f	Flow characteristic time	m
τ_p	Tracer particle response time	s
θ	Crank angle	deg
$\vec{\omega_x}, \vec{\omega_y}, \vec{\omega_z},$	Vorticity components in x, y and z respectively	$1/s$
$\vec{n}$	Normal vector	-
A	Frontal Area	m^2
C_D	Drag coefficient	-
C_DA	Drag area	m^2
C_p	Coefficient of pressure	-
D	Diameter of sphere	m
d_p	Tracer particle diameter	m
d_τ	Image particle diameter	m
d_{diff}	Diffraction diameter	m
d_{geom}	Geometrical particle diameter	m
DSR	Dynamic Spatial Range	-
DVR	Dynamic Velocity Range	-
$f_\#$	f-number	-

f_c	Focal length of objective	m
M	Magnification	-
$MART$	Multiplicative Algebraic Reconstruction Technique	-
N	Number of samples considered for time-averaging	-
$Nd:YAG$	Neodymium-doped Yttrium Aluminium Garnet	-
$Nd:YLF$	Neodymium-doped Yttrium Lithium Fluoride	-
p	Static pressure	N/m^2
p_∞	Freestream pressure	N/m^2
PIV	Particle Image Velocimetry	-
ppp	Particles per pixel	-
Q	Q-criterion	-
Re	Reynolds Number	-
u', v', w'	Fluctuating part of velocity components respectively	m/s
UCI	Union Cycliste Internationale	-
Z_0	Distance from lens to Measurement Plane	m
z_0	Distance from lens to Image Plane	m
CFD	Computational Fluid Dynamics	-
FSU	Fluid Supply Unit	-
HFSB	Helium-filled soap bubbles	-
PTV	Particle Tracking Velocimetry	-
SMTE	Sequential Motion Tracking Enhancement	-
SNR	Signal to Noise Ratio	-

Chapter 1

Introduction

In the history of many speed-sports such as running, cycling, speed-skating, skiing or bob-sleighing, examples are found where aerodynamics played a crucial role in the outcome of a race, as they are often decided by only fractions of a second. A body moving through a fluid experiences aerodynamic forces such as lift and drag. The contribution of the aerodynamic drag in each speed-sports is different, e.g. in bobsleighing it is equal to 25% (Winkler and Pernpeintner (2008)), in speed skating it is already about 80% (Sætran and Oggiano (2008)) and in time-trial cycling races it can even go up to 90% of the total force that the athlete has to overcome (Gibertini and Grassi (2008)).

The winning margins for these speed-sports are within fractions of the total race time, e.g. on average a bobsleigh race takes about $60s$ where the top three ends within a few seconds of each other. Another example can be found in cycling, more specific in the Tour de France, the winner of 2017 finished in $86h20m55s$, the runner-up finished within one minute (le Tour de France (2017)). Improving the aerodynamics of both the runner-ups by only 1% would have made them victorious. Aerodynamic investigation is thus needed to minimize drag and maximize velocity. In multiple sports, such as for example cycling, team coaches and athletes know this and the last few decades a lot of research has been done towards improving the aerodynamics of the athlete. A good reference to measure the effect of this research is the evolution of the 1-h time-trial record in cycling. Between 1905 and 1972 the record increased linearly from $40.78km/h$ to $49.43km/h$. This record stood till 1984, when Francesco Moser used disk wheels and a skin suit to break the record. This proved the importance of aerodynamics in cycling and opened the doors for further research and innovations. This period reached its peak in 1996 when Chris Boardman set the world record to $56.38km/h$ riding the 'superman-position'. Following this record the UCI decided to set some regulations to the equipment used for a world record and divided the records into separate "best human effort" and "world record" categories. The record of Boardman was classified under the former and the world record was set back to $49.43km/h$. From 2014 onwards the UCI allowed the use of technologies currently available in endurance track events to improve the world record, which led to the current world record of $54.53km/h$.

Currently most sport aerodynamics investigations are conducted by means of Computational Fluid Dynamics (CFD) simulations or by balance measurements in the wind tunnel. The wind tunnel is the most common used tool for the assessment of sport aerodynamics because it provides a controlled and repeatable wind environment for a wide range of conditions, which makes it possible to perform precise and on-demand measurements. However, often a static and scaled model, which suffers from Reynolds effects, is used for whole field measurements, whereas full-scale tests are mostly limited to studies on local flow features. Gibertini and Grassi (2008) performed balance measurements in the wind tunnel in order to investigate the effect of the athletes′ position on the aerodynamic performance. Figure 1.1 depicts some of these positions. A reduction in aerodynamic drag of 20% was found going from "drops position" to "time trial" position, furthermore they concluded that the position of the head effected the total drag by only 1%.

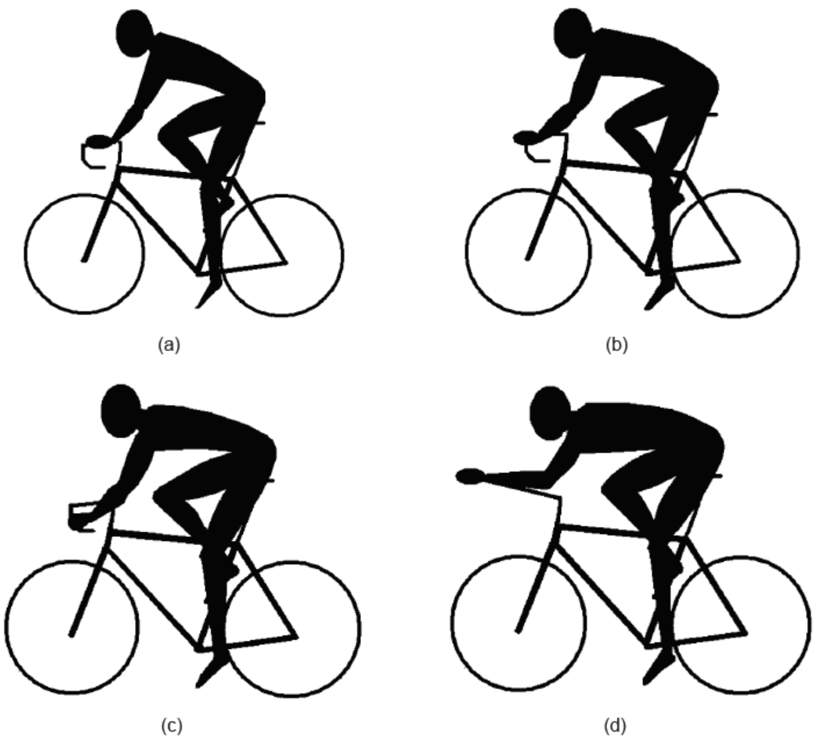

Figure 1.1: (a) Upright Position (b) Hoods (c) Drops (d) Time-trial position. Adapted from Gibertini and Grassi (2008)

Another study, performed by Meile et al. (2008), characterized the aerodynamics of ski-jumping by comprehensive wind tunnel experiments, which covered the widest possible range of flight positions of the jumper. The major finding is the relative influence of the skis on the overall aerodynamic forces, the relative lift area is found to be significantly larger than the drag area within the investigated regime. A third example of sport aerodynamic experiments can be found in the Formula One of winter sports, boblseigh. Winkler and Pernpeintner (2008) carried out wind tunnel measurements on a 1:3 scaled model of a bobsleigh in order to improve its aerodynamic performance. They managed to decrease the drag by 13% compared to the existing bobsleigh. Also it was discovered that the position of the brakeman has a significant influence on the total aerodynamic drag.

The above mentioned studies were performed by using a force balance in the wind tunnel. This is one of the most accurate methods currently available, however, these are only 'blind' measurements and they do not give you any information on flow field around the athlete. In order to optimize the aerodynamics of the athlete, understanding of the flow field around the athlete is of paramount importance. One way to visualize the flow field is to use CFD tools. With increasing computational power, better meshing methods and improved turbulence models, CFD is increasingly applied to sports aerodynamic problems, varying from motor sports or ball sports till swimming or cycling (Hanna (2002)). The main advantages of CFD are that it has the potential to solve the entire flow field in space and time and in the same time it is able to determine the aerodynamic forces acting on the object of interest and decompose them into the viscous and pressure components. However, the flow around athletes and their equipment in sport aerodynamics can be categorized as bluff-body aerodynamics, which has the key feature of flow separation, leading to a large turbulent wake. Currently CFD tools are not yet capable to fully calculate such a three-dimensional, unsteady flow field and thus, in order to predict the effect of turbulence in the wake, CFD simulations make use of turbulence models. As a consequence one should be careful when interpreting the results of CFD when applying it to sport aerodynamic applications. Griffith et al. (2012) uses CFD to investigate the flow topology in the wake of a cyclist in time trial position for different static leg positions. The flow structures observed are similar to the ones obtained experimentally. Furthermore a dependence of the drag on the crank angle was observed, with high drag measurements corresponding to geometries where the athlete has one leg extended, however, the drag area is under-predicted by roughly 15%. A CFD study into the aerodynamics of wheelchair racers by Hart (2014) pointed out that the aerodynamic drag of the wheelchair and athlete can account for up to three quarters of the total resistive force. Implementing a streamlined chair with aerodynamically optimised frame sections, aero wheels, and fairings would already significantly reduce the drag as well as the use of aerodynamically optimised helmets would. Another branch of sport where the use of CFD for aerodynamic investigations is gaining in popularity, is motor sports. Mariani et al. (2015) analysed the external aerodynamics of a Formula Student Racing Car (figure 1.2). The study mainly focuses on the comparison of the car with and without adding some appropriate aerodynamic elements such as: front wing, headrest, rear engine hood and aerodynamic extractor. All these aerodynamic features lead to an overall drag reduction of 15% and 342% extra down force.

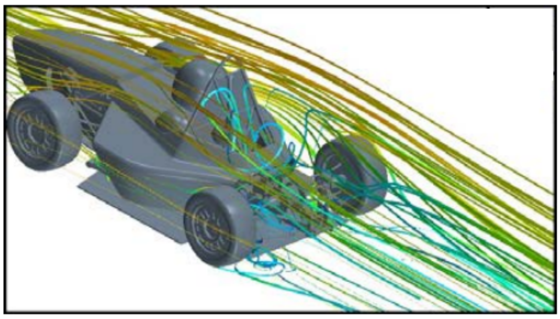

Figure 1.2: Stream lines around the car before the adoption of a rear hood calculated by CFD. (Mariani et al. (2015))

The previous mentioned studies show that, despite the still increasing computational power, currently CFD is not able accurately predict the drag. On the other hand, the studies performed in the wind tunnel using a balance give very accurate force measurements, however, they lack to tell us anything about the flow field that causes the drag and are often performed on static scaled models. A third option is to perform local flow measurements either by scanning through the measurement area with pressure probes (Crouch et al. (2014),Crouch et al. (2014)) or conducting whole-field measurements using particle based velocimetry (Barry et al. (2016), Jux (2017)), leading to increased understanding of the human body aerodynamics. These experiments are typically conducted on stationary models in wind tunnels allowing accurate conditioning of the flow environment leading to repeatable measurements. Wind tunnel testing, however, can be expensive and technically challenging, for example when requiring a rolling floor. Furthermore, in the wind tunnel environment it is unfeasible to investigate the flow over an accelerating athlete or one that follows a curvilinear path. This shows us that, within the scope of measurement techniques for sport aerodynamic investigation, there is the necessity for an experimental system that is able to investigate large-scale flows of sports aerodynamic applications in their race environment, resulting in both drag force measurements as well as flow visualisation.

With this in mind, the idea of the Ring of Fire, a quantitative flow visualization technique for on-site sport aerodynamics optimization, arose and was first reported on by Sciacchitano et al. (2015). The concept: perform large-scale Tomographic PIV measurements, with Helium-Filled Soap Bubbles (HFSB) as flow tracers, during the athletes$'$ training in a velodrome, thus reproducing the same flow conditions met during races. From the obtained velocity fields, the aerodynamic forces acting on the athlete can then be extracted by making use of the flow dynamics equations. A first proof of concept was performed by Terra et al. (2017) on a transiting sphere with a diameter of 10cm at a velocity of $1.5m/s$. The obtained time-average drag coefficient, evaluated via a control volume approach, was found to fall within the range of reported values in literature. Furthermore it was observed that from 5 diameters in the wake, only the momentum term and the Reynolds stresses affect the drag coefficient, the pressure term can be neglected. The works of Sciacchitano et al. (2015) and Terra et al. (2017) are the starting point of this master thesis and provide the author with the correct ingredients to formulate the following research objective:

"Assess the feasibility of an on-site aerodynamic measurement system (Ring of Fire) based on large-scale PIV for full-scale applications in speed sports. Further, test the accuracy of the system by comparing the drag values obtained at multiple different velocities from a scaled test setup."

The research objective of this thesis consists of two parts, on one side the accuracy of the system needs to be tested and analysed on a small scale and on the other side the feasibility of the full-scale system has to be assessed. To successfully fulfil both parts of the research objective, two experimental campaigns are designed and executed. The experimental setup of both experiments can be found in chapter 5. The results of the small-scale experiment are presented in chapter 6, the results of the full-scale experiment are presented in chapter 7. The small-scale experiment is similar to the experiment of Terra et al. (2017), measuring a 10cm sphere at five different velocities to determine the accuracy of the system. The conclusions on the accuracy of the system are reported in chapter 6. The full-scale experiment measures the flow in the wake of a full-scale, transiting cyclist. Given the complex and turbulent flow, including multiple vortices, in the wake of a athlete, this application is considered a suitable test case for the proposed system. Furthermore chapter 2 presents previous work relevant to the topic of this thesis, chapter 3 presents the experimental techniques used during both experiments and the data reduction techniques are presented in chapter 4.

Chapter 2

PIV applications for sports and transiting objects

The Ring of Fire is a new concept for quantitative on-site aerodynamic flow visualization on transiting objects by large-scale PIV. The working principle of PIV and its large-scale version will be discussed in detail in chapter 3. The system consists out of four parts: 1.Large-scale Particle Image Velocimetry for flow visualization; 2.Particle Image Velocimetry measurements on transiting objects; 3.On-site Particle Image Velocimetry measurements; 4.Loads determination from Particle Image Velocimetry. Each of these individual cases can found in literature, so before putting them together into one system, the Ring of Fire, the previous work done in these fields is discussed in this chapter. Section 2.1 starts with an overview of Large-scale PIV applications in sports, followed by PIV measurements on transiting object in section 2.2. Section 2.3 then focuses on applications of the measurement technique on-site and finally section 2.4 takes a closer look into the work on determining loads from PIV.

2.1 Application of Particle Image Velocimetry in Sports

To date many of the studies where PIV has been used for flow visualization in sport aerodynamics have been conducted on scaled models. Barry et al. (2014) investigate the aerodynamics of slipstreaming cyclists by planar PIV measurements. Two 1:7 scaled cyclists were placed in a water tunnel, resulting in a Reynolds number which was an order of magnitude smaller then the real case. This indicates the need for more realistic, full-scale measurements, however, not many full-scale PIV studies have been performed on a full-scale sport application and to date most of the full-scale studies are limited to local flow features. The works of Matsuuchi et al. (2009) and Takagi et al. (2014) are nice examples of this as they investigate the local flow features around the hand of a swimmer. Both experiments acquired planar PIV data on a measurement area of $500 \times 500mm$ at a velocity of $1.2m/s$ with $50\mu m$-diameter nylon particles as tracers in the flow. The experimental setup of Takagi et al. (2014) is shown in figure 2.1(a) and some of the results are shown in 2.1(b).

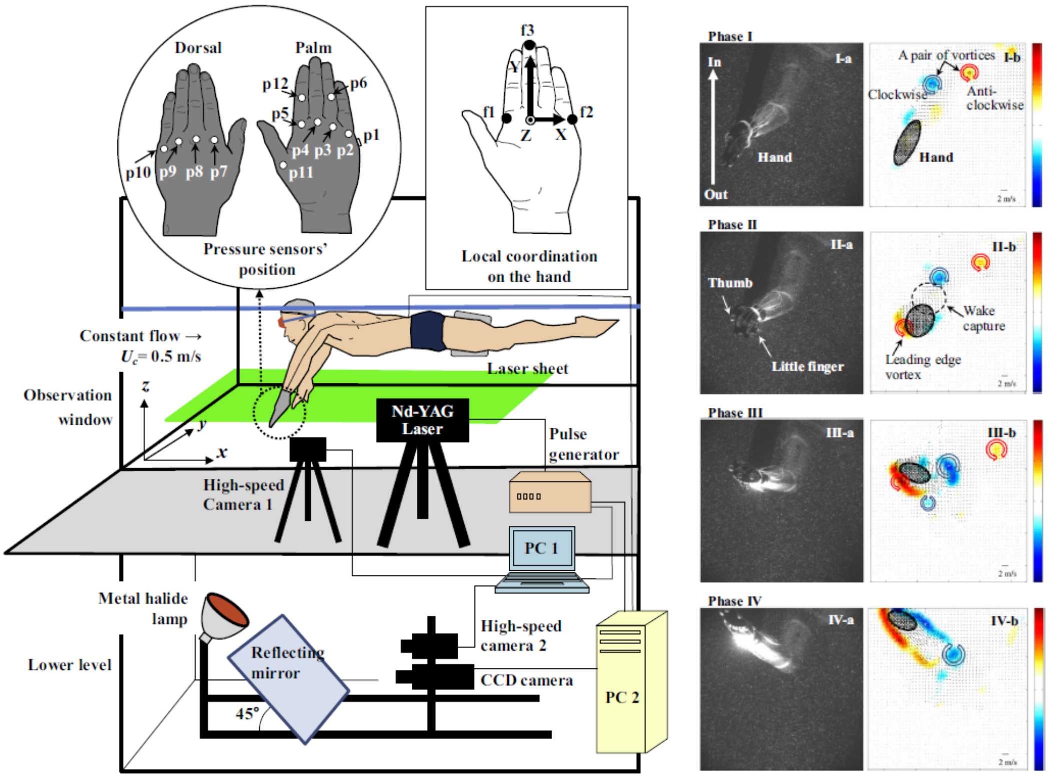

(a) Schematic of the experimental setup

(b) Maps of vorticity and velocity around the hand

Figure 2.1: Illustration of measurement setup and corresponding results presented by Takagi et al. (2014)

Other examples of the uses of planar PIV in sport aerodynamic research are found in the works of Celis and Ubbens (2016) and Leong et al. (2010). The former showed that with the use of PIV, the effect of small geometrical changes on cycling aerodynamics can be investigated. They have done this by investigating the effect of adding a groove in the seat post of a bicycle. Figures 2.2(a) and 2.2(b) show respectively the windtunnel test section where the PIV system is setup and the obtained result.
Leong et al. (2010) investigated the effect of the head position on the aerodynamics of Olympic Skeleton Athletes. A mock section of a bobsled track is placed at the exit of an open loop windtunnel and planar PIV measurements were made along with video recordings of the position of the head. A picture of the athlete during the measurement campaing is presented in figure 2.3(a) and an instantaneous vorticity field in the wake of the helmet is shown in 2.3(b).
However both studies are performed on a full-scale test object, the measurement areas are still small since they study only local flow features. The measurement area of both studies is in the order of $200 \times 200mm$.

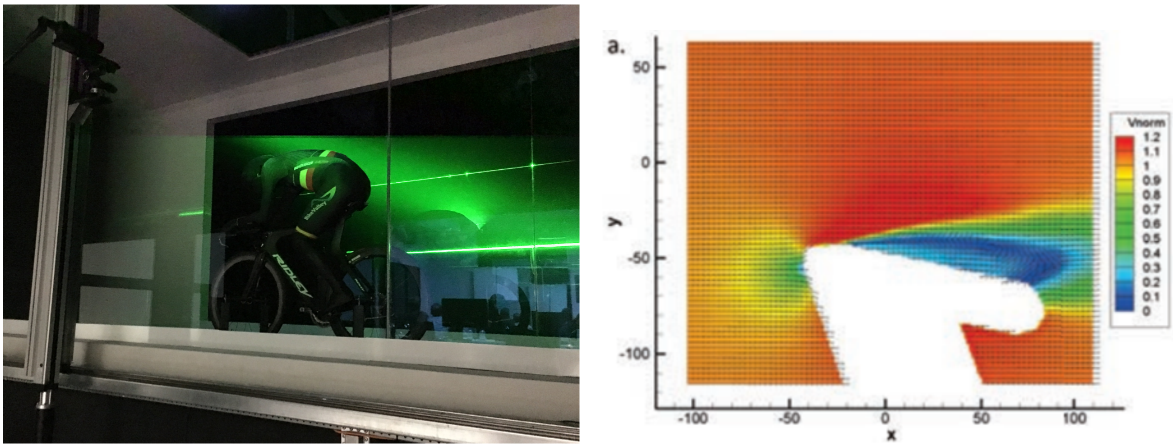

(a) Picture of the PIV setup

(b) Resulting velocity magnitude measurements of the seat post of the bike

Figure 2.2: Picture of measurement setup and corresponding results presented by Celis and Ubbens (2016)

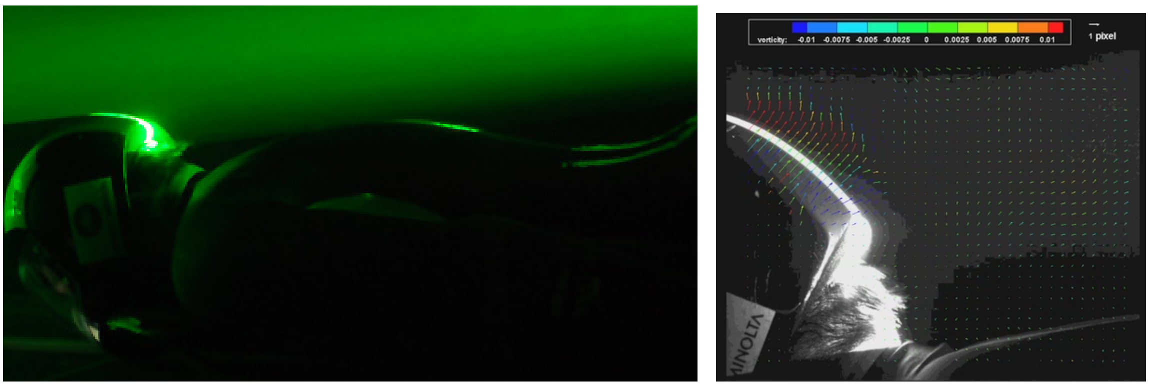

(a) Picture of a PIV experiment on a skeleton athlete

(b) Resulting vorticity measurements in the wake of the helmet

Figure 2.3: Picture of the measurement and corresponding results presented by Leong et al. (2010)

Chabroux et al. (2010) also acquired full-scale PIV data of local flow features, however instead of planar measurements, they chose to perform stereoscopic PIV. The experimental setup of this study is given in figure 2.4. They gathered multiple planar measurements in the wake of the helmet of a replica time-trialling cyclist. The different planes are separated by a 50mm increment in the out-of-plane direction. This experiment shows the ambition of the community to acquire data in a three dimensional volume and already comes closer to how the Ring-of-Fire PIV setup is imagined.
Recently the research group at the Technical University of Delft investigated the

flow field around a static, full-scale model of Tom Dumoulin in time trial position. Three different experiments were conducted at different wind velocities, two of them obtained data from a tomographic PIV/PTV setup in the wake of the model (Terra et al. (2016) and Shah (2017)), the third experiment acquired tomographic PTV data all around the model with a robotic coaxial PIV system (Jux (2017)). In the first experiment Terra et al. (2016) were able to scan an area of $1.0 \times 1.7m^2$ with a thickness of $3cm$ in the wake of a full-scale model. This meant a giant increase in the measurement volume, which was made possible by the use of HFSB tracers. The data was acquired at $4m/s$ and similar results were found compared to the ones of Crouch et al. (2014), PIV made it even possible to get a higher resolution. The tested speed is low compared to race conditions, this was due to the need of achieving sufficient seeding concentration. The results and experimental setup can be seen in figure 2.5. These measurements were conducted at a non-realistic low Reynolds number so the experiment was repeated and and the results were confirmed at more realistic speeds of 14 m/s by Shah (2017).

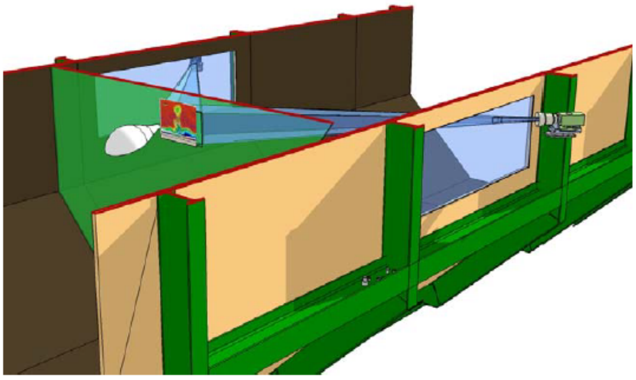

Figure 2.4: Illustration of measurement setup presented by Chabroux et al. (2010)

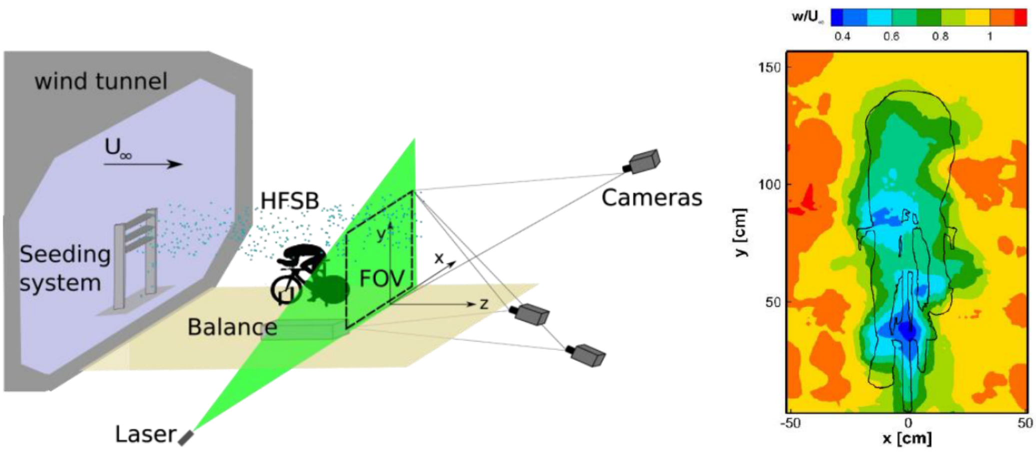

(a) Illustration of the test setup

(b) Wake measurements showing (normalised) streamwise velocity

Figure 2.5: Illustration of measurement setup and results presented by Terra et al. (2016)

In comparison to the previous two studies, the study of Jux (2017) does not look in the wake of the cyclist but rather investigates the flow field around the athlete in a $2m^3$ domain. The whole domain is scanned with 450 individual coaxial PTV measurements and is stitched together afterwards. The flow topology, evaluated in terms of velocity and vorticity fields, is comparable to the wake measurements of Crouch et al. (2014) and Shah (2017). The three dimensional measurement domains in these studies on the 3D-printed model of Tom Dumoulin show that tomographic PIV/PTV is still improving, however, there are still a few shortcomings. For example the test setup shown in figure 2.5(a), used by Terra et al. (2016) and Shah (2017), is very complex to build up and calibrate. The coaxial robotic PTV system used by Jux (2017) does not have this problem, however obtaining the 450 runs to cover the whole measurement domain is very time consuming. Furthermore both experiments are performed on a static model and are still composed of multiple individual PIV acquisitions, given that the full measurement domain cannot be seeded with sufficient HFSB concentration at the same time.

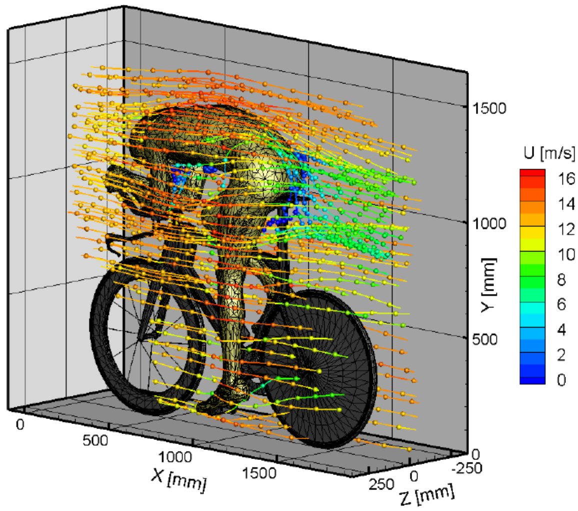

Figure 2.6: Streamline contours around the full-scale cyclist at $U_0 = 14m/s$ presented by Jux (2017)

2.2 Application of Particle Image Velocimetry on Transiting Objects

Testing models in a windtunnel with a fixed floor and model supports often leads to interaction of the flow field with the floor that does not occur in real life. To avoid this sometimes an expensive moving belt is used to simulate the moving floor underneath the object. Another option that is often applied, is the use of towing tank facilities.
The work presented by Scarano et al. (2002) demonstrates the applicability of PIV diagnostics in wake vortex research with towing-tank facilities. PIV measurements were performed on a 1:48 scaled model of a large transport aircraft A340300, towed at 3m/s and 5m/s. The towing tank at the TU Delft Maritime Engineering laboratory has a cross section of $4.22 \times 2.5m^2$ and has a length of $142m$. This measurement setup, presented in figure 2.7, allowed producing a vortex wake that could be analysed in time at a fixed position which corresponds to the streamwise downstream coordinate with respect to the aircraft.

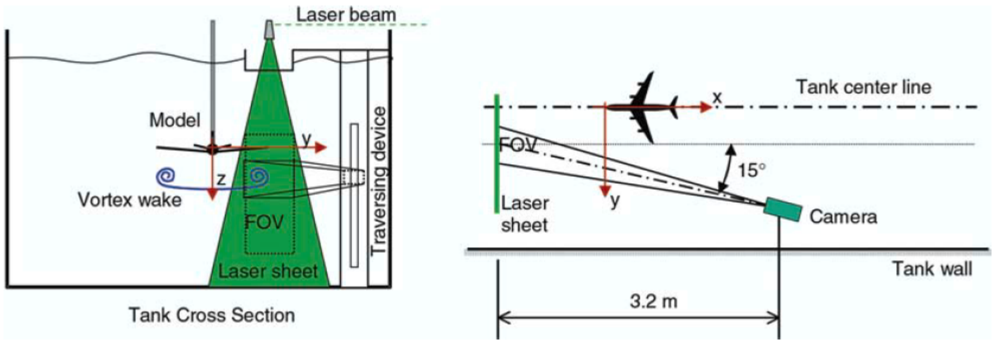

Figure 2.7: Schematic of the experimental setup; towing tank cross section (left); top view (right)(Scarano et al. (2002)).

Jönsson and Loose (2016) investigates the flow field underneath a generic high-speed train. This topic is of special interest for train speeds so high that velocity and pressure fluctuations in the train under flow region are high enough for ballast stones to be lifted. A moving floor is crucial to this research and so experiments are conducted in a $18m$ long steel towing tank with a cross-section of $1.1 \times 1.1m^2$. The 1:50 scaled train model is towed at $4m/s$, which corresponds to a Reynolds number of approximately 2.4×10^5. This study showed that important information can be extracted from downscaled model measurements in a towing tank, however extrapolating the results into full-scale is not always possible and so there is need for full-scale measurements.

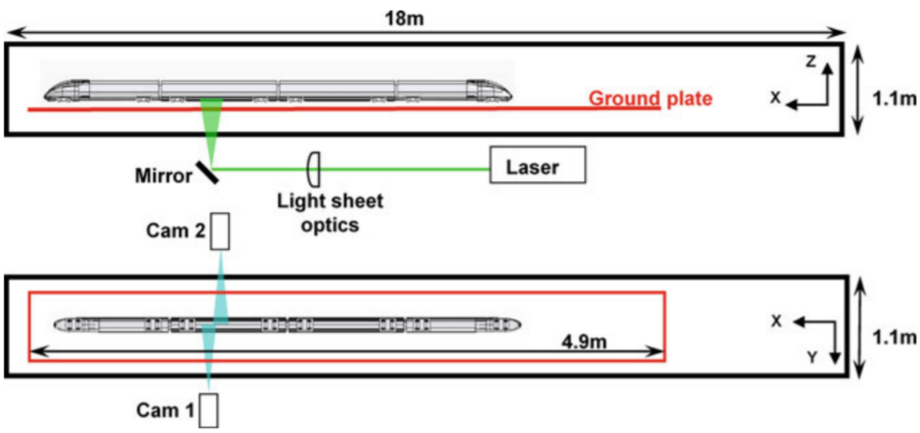

Figure 2.8: Schematic of the experimental setup in a water towing tank (Jönsson and Loose (2016)).

2.3 On-site Application of Particle Image Velocimetry

Despite the technological developments over the past few decades, PIV is still predominantly used in research laboratories and academia. However, sometimes the flow in a laboratory is not a good representation of reality and thus on-site measurements are needed. One such example was mentioned in the previous section, namely the flow field underneath a high-speed train, which is best investigated on a transiting, full-scale train. Henning et al. (2016) performed such an experiment by conducting PIV measurements at the lateral underfloor region of a full-scale high-speed train, passing by at $44m/s$. A schematic of the experimental setup is given in figure 2.9(a). This is the first time on-site PIV measurements are conducted on a transiting object. The velocity fields are captured by planar PIV at four successive planes, each with an approximate size of $0.35 \times 0.6m^2$. The results show vortical structures as well as significant vertical velocity components, which indicates a high three-dimensionality of the flow field. This shows the need for an on-site large-scale PIV system that is able to capture three-dimensional flow.

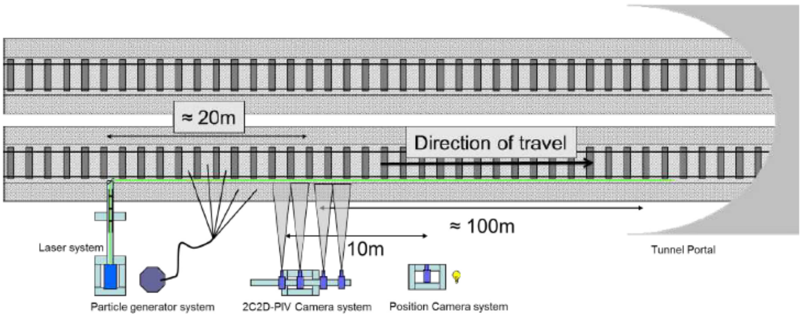

(a) Schematic of the experimental setup.

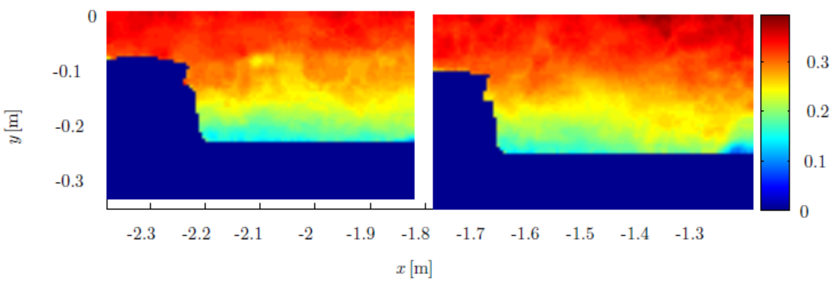

(b) Time-averaged velocity magnitude distribution scaled with the train speed $U_\infty = 44m/s$.

Figure 2.9: Illustration of the measurement setup and corresponding results presented by Henning et al. (2016)

Another great example of this necessity of on-site measurements is presented in the work of Toloui et al. (2014). They used PIV to perform a spatial characterization of the turbulent atmospheric boundary layer. Laboratory studies of these flows are severely constrained by the enormous differences in Reynolds number associated with the limited range of spatial scales achievable in wind tunnel experiments. A schematic representation of the setup is given in figure 2.10(a). The measurement area captured with this PIV setup was roughly $22 \times 55m$, with a spatial resolution of $\approx 0.34m$ and snow particles are used as tracer particles.

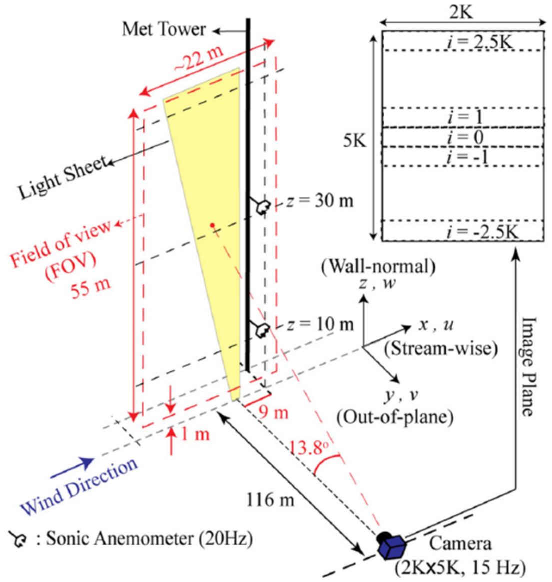

(a) Schematic of the experimental setup

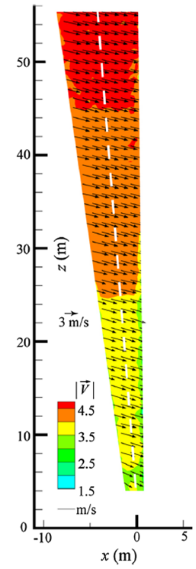

(b) Instantaneous velocity vector fields from PIV measurements

Figure 2.10: Illustration of the measurement and corresponding results presented by Toloui et al. (2014)

Another field of interest where small-scale experiments suffer from scaling issues (i.e. Froude- and Reynolds-number (Re) scaling incompatibility) as well as difficulties in matching the Reynolds number are natural river flows. Blois et al. (2016) employs an Unmanned Aerial Vehicle (UAV) system to remotely, safely and cost effectively gain high-resolution videos of a river water surface. Applying PIV analysis on time-correlated image pairs, which are extracted from the video, made it possible to resolve the velocity field at the water surface. The measurement area is roughly $20 \times 30m^2$ and the foam on the water is used as tracer particles.

2.4 Loads Determination from Particle Image Velocimetry

Loads determination based on wake survey deals with the determination of the momentum deficit of the flow past the object. The theory of such approach will be discussed in detail in section 3.2. From the difference in momentum between the wake and the incoming stream the aerodynamic force is computed. Before PIV existed, this approach was practised by means of multi-hole Pitot probes in wake rakes. Such a wake rake was used by Goett (1939) to determine the profile drag of three different NACA airfoils as well as by Selig et al. (2011), who used it to document the peculiar drag characteristics of low Reynolds number airfoil flows by investigating the non-uniformity of the airfoil profile drag along the span.
In the more recent history Kurtulus et al. (2007) and Van Oudheusden (2013) demonstrated

that, by using this control volume approach, the drag force on a stationary object can be obtained from PIV measurements as well. Regarding moving objects, the approach was applied by Ragni et al. (2011) to determine the aerodynamic forces over propeller blades and by Neeteson et al. (2015), who estimated the drag of a sphere freely falling in water.

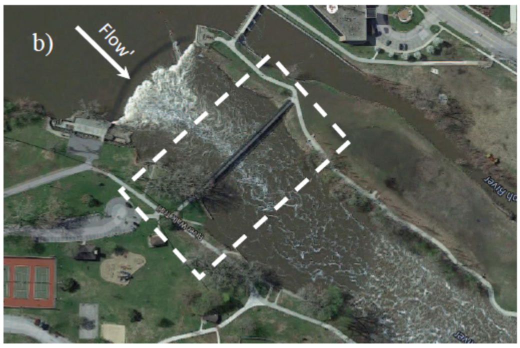

(a) detail of the survey location. The dashed rectangle represents the field of view.

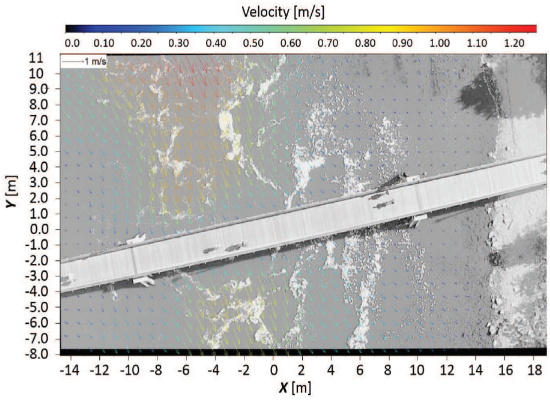

(b) Instantaneous velocity field obtained at the survey location.

Figure 2.11: Illustration of the measurement location and corresponding results presented by Blois et al. (2016)

Chapter 3

Experimental Techniques

In the present study Stereoscopic and Tomographic Particle Image Velocimetry (PIV) are used to visualize the flow in the wake of a transiting body. Therefore this chapter will start with describing the basic principles of this non-intrusive measurement technique in section 3.1. The next section in this chapter, section 3.2, will discuss how to apply the control volume approach to get the drag force on the body from the velocity fields.

3.1 Principles of Particle Image Velocimetry (PIV)

Particle image velocimetry is a non-intrusive measurement technique that measures the velocity flow field. Over the last few decades PIV has gone through a great development and is currently the most popular flow measurement techniques because of its ability to describe a complete velocity field. This non-intrusive measurement technique provides an instantaneous measurement of the flow field in a plane (planar PIV:2D-2 , stereoscopic PIV: 2D-3C) or in a volume (tomographic PIV: 3D-3C). For an overview of the use and for a more in-depth discussion on the working principles of PIV, the reader is referred to the books of Raffel et al. (2006) or Adrian and Westerweel (2011).

3.1.1 Tracer Particles

The choice of the tracer particles is of crucial importance because the velocity of tracer particles is measured instead of the fluid velocity. In the current experiments Helium Filled Soap Bubbles (HFSB) are used as tracer particles, they were chosen based on their fluid mechanical properties (ability to follow the ambient flow) and on their light scattering behaviour (ability to be tracked with the cameras).

Mechanical Properties and Flow Characteristics

For a particle to have the ability to accurately follow the flow and to minimize the velocity lag, the response time of a particle (τ_p) is required to be below the flow characteristic time (τ_f), which is defined as the ratio of a characteristic length scale and a velocity scale. A tracer particle is suitable for a particular flow measurement if the Stokes number ($S_k = \tau_p/\tau_f$) is in the order of 0.1 or less. Properties such as the size and density of the particle play a crucial role in determining its response time, which can be calculated by equation 3.1 (Raffel et al. (2006)):

$$\tau_p = \frac{{d_p}^2 \cdot (\rho_p - \rho_f)}{18 \cdot \mu} \tag{3.1}$$

where d_p is the diameter of the particle, ρ_p is the density of the particle, ρ_f is the density of the fluid and μ is the dynamic viscosity. When a particle is neutrally buoyant ($\rho_p \approx \rho_f$), particles with a large diameter are allowed while still keeping a low response time.

Most of the tracer particles used in PIV however, are heavy particles and when considering them it is obvious that they are far from neutrally buoyant. Raffel et al. (2006) states that the response of a heavy particle to a sudden increase in velocity of the fluid is exponential. The velocity varies according to equation 3.2:

$$v(t) = u\left(1 - exp\left(-\frac{t}{\tau_p}\right)\right) \tag{3.2}$$

From equations 3.1 it is clear that, considering the same particle density, a smaller diameter leads to a lower response time. This is also illustrated in figure 3.1. Reducing the particle diameter too much, however, will lower the light scattering properties of the particle. A compromise will have to be made between both aspects.

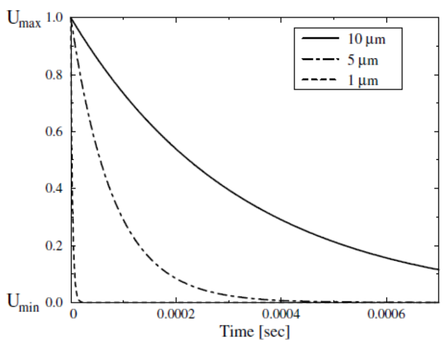

Figure 3.1: Time response of different sized oil particles in a decelerating air flow. Raffel et al. (2006)

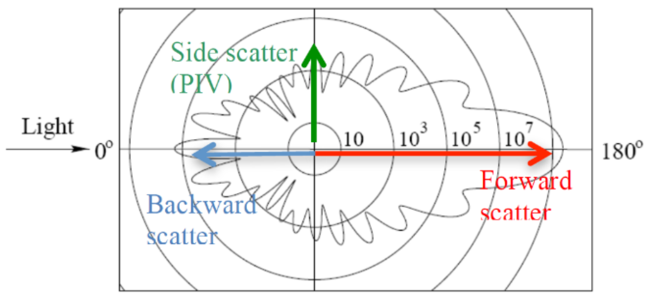

Figure 3.2: Light scattering by a 1 μm oil particle in air. Scarano (2013a)

Light Scattering Properties

Besides the fact that particles need to have a small relaxation time and a high tracking fidelity, they also need to scatter enough light to generate sufficient contrast between the illuminated particles and the background. There are a few factors that determine the scattering properties of a particle: size, shape and relative refractive index of particle to the fluid and the light source. Besides the factors that are dependent on the particle itself, there is also a dependency on the direction of reception or observation of the scattered light. When the particle diameter is larger than the wavelength of illuminating source, Mies light scattering theory is applicable (Raffel et al. (2006)). Figure 3.2 illustrates the polar distribution of the scattered light intensity for an oil particle of $1\mu m$ in air with a wavelength λ of 532 nm according to Mies theory.
Figure 3.2 teaches us that the most advantageous direction of observation is the forward one because its intensity is very high in comparison with the others. However, due to limitations regarding depth of field and optical access, PIV recordings are commonly conducted at 90°.

Helium Filled Soap Bubbles (HFSB)

HFSB are considered as one of the best tracer particles for large-scale PIV given their high scattering cross-section and low response time (Scarano et al. (2015)). In recent years an increase in quantitative low speed experiments that uses HFSB as tracer particles is seen. A few examples are: large-volume pressure measurements from tomographic ptv on a surface mounted cylinder near-wake Schneiders et al. (2016), an experiment in the near wake of vertical axis wind turbines Tescione et al. (2014) or experiments on the mixed convection in the aircraft cabin mock-up (Bosbach et al. (2006)). The response time of the HFSB is found to be in the range from $10\mu s$ to $40\mu s$, depending on the flow rate of the different fluids (Scarano et al. (2015)). The flow characteristic times for both the scaled experiment as well as the full-scale experiment are respectively $66.6ms$ and $12.5ms$, yielding both times in a Stokes number far below 0.1 and thus the HFSB are suitable tracer particles for both experiments. With a density very similar to that of air, the HFSB are able to become as large as 400 μm and still having a low response time (see equation 3.1).
The reason why the HFSB are so attractive for large-scale measurements are their light scattering properties. The large particle diameter results in a huge scattering cross-sections as compared to other tracer particles. The scattering cross-section and scattered intensity are known to be proportional to the square of the particle diameter and so the 100 times larger HFSB have a scattered intensity 10.000 larger than for example DEHS particles.

3.1.2 Illumination

The illumination system ensures that the tracer particles are visible in the recordings. Commonly lasers are employed as light sources for PIV application, as they have the ability to provide pulsed, collimated monochromatic light with high energy density. The laser light can easily be shaped in a thin light sheet without chromatic aberration by spherical and cylindrical lenses.

Pulsed Q-switched solid-state lasers, such as Nd:YAG and Nd:YLF are commonly used for PIV applications. Nd:YLF lasers are often used for high-speed applications since they operate in the kilohertz range and emit light with a wavelength of 527nm. Their pulse energy is equal to 60 mJ at 1 kHz and goes below 10mJ at 10kHz. Nd:YAG lasers provide light with a wavelength of 532nm, a pulse width below 10ns and repetition rates up to 50 Hz. The following parameters should be taken into consideration when choosing the illumination source:

- *The light pulse width* δt must be small so that the particles appear as dots and not as streaks. In other words, the motion of the particles during the pulse exposure must be frozen at one time instant.

- *The pulse separation* Δt must be short enough to capture the particle twice before it leaves the light sheet and long enough to determine the displacement of the particle with a resolution that is sufficiently high.

- *The time interval* ΔT is used to decide if the subsequent velocity fields are correlated in time or not. It is often used by its inverse, namely the acquisition frequency.

3.1.3 Imaging System

The principles of particle imaging are schematically represented by Figure 3.3. The images of the illuminated particles in the object plane are obtained by a CCD camera. The camera is equipped with an objective (lens) which allows the light from the measurement space to be focused on the sensor of the camera (see figure 3.3). The magnification of the system is defined as:

$$M = \frac{z_o}{Z_0} \tag{3.3}$$

where the z_0 is the image distance and Z_0 the object distance. Based on the magnification and focal length (f_c) of the objective, the object distance is determined:

$$\frac{1}{f_c} = \frac{1}{z_0} + \frac{1}{Z_0} \rightarrow Z_0 = f_c\left(1 + \frac{1}{M}\right) \tag{3.4}$$

The combined CCD sensors of the camera form the image plane and capture the intensity of the illuminated particles. The intensity distribution on the image plane is read out from these sensors as a two dimensional array of grey intensity levels, which is the resulting image of the particles. The particle image diameter (d_τ) is the Euclidean sum of the diffraction diameter and the geometrical image diameter:

$$d_\tau = \sqrt{d_{\text{geom}}^2 + d_{\text{diff}}^2} \tag{3.5}$$

where d_{geom} is the geometrical image diameter and d_{diff} is the diffraction diameter. The geometrical diameter can be expressed as:

$$d_{geom} = d_p M \tag{3.6}$$

where d_p is the physical particle diameter. The diffraction diameter is expressed as:

$$d_{diff} = 2.44\lambda(1 + M)f_\# \tag{3.7}$$

where λ the wavelength of the light and $f_\#$ is the f-number. This diffraction diameter is the result of the Fraunhofer diffraction, which is the light diffraction that occurs when the scattered light of the particle, which behaves as a point light source, passes a circular aperture(lens).

In PIV, typically the geometric image diameter is very small compared to the diffraction term. From this it follows that $d_\tau = d_{diff}$. In order to prevent occurrence of peak/pixel locking, which occurs when the size of the diffraction-limited particle images on the sensor becomes too small and thus results in under-sampled particle images, d_τ should be kept at 2-4 pixels Michaelis et al. (2016).

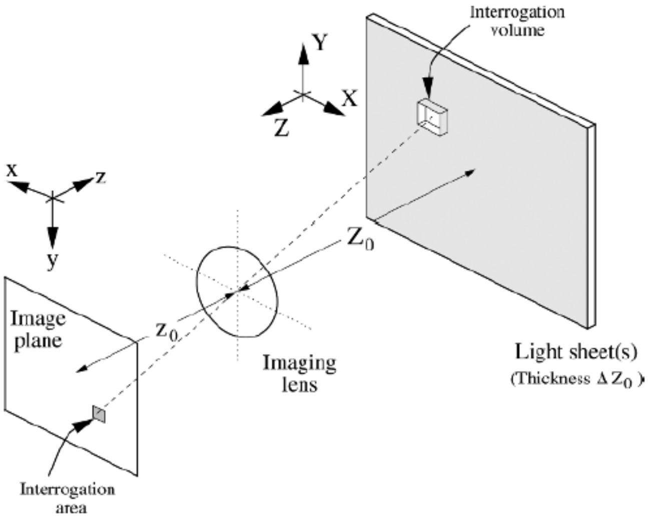

Figure 3.3: Optical arrangement of a PIV system. Raffel et al. (2006)

It is important to image the particles in focus. For the depth of the measurement region this means that the depth-of-field δz should have a thickness equal to that of the laser sheet or more. The depth-of-field can be calculated by the following equation (Raffel et al. (2006)):

$$\delta z = 4.88 \left(\frac{M+1}{M} \right)^2 f_{\#}^2 \lambda \tag{3.8}$$

Following equations 3.5, 3.7 and 3.8 it is observed that the f-number controls two important imaging parameters, i.e. the particle image diameter and the depth-of-field.

3.1.4 Stereoscopic PIV

"Standard" (planar) PIV only measures the projection of the velocity vector onto the laser plane, in two dimensions. For highly three-dimensional measurements the results are affected by the perspective error and the third out-of-plane velocity vector is not measured.
In order to measure this third velocity component, stereoscopic (stereo) PIV is used. Stereoscopic PIV is a three component measurement in plane (2D-3C). Figure 3.4 shows a schematic representation of a stereoscopic PIV setup. Stereoscopic PIV makes use of two cameras, which are placed at an angle with respect to the perpendicular line of the flow and with respect to each other. This geometry allows to measure the out-of-plane velocity component. Typically, the angle between both cameras varies from 60° to 90°. The closer this angle is to 90°, the higher the precision of the measured out-of-plane component. In this setup there is a perspective distortion due to the oblique view of the scene. To correct for this, the back plane is tilted using the Scheimplug criterion, which states that the image plane, object plane, and the lens plane intersect at a common line Raffel et al. (2006).

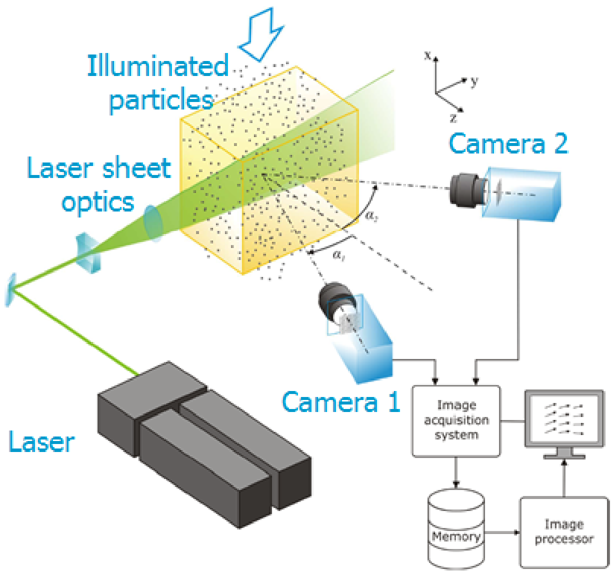

Figure 3.4: Schematic of a stereoscopic PIV measurement system.Scarano (2013a)

The displacement in out-of-plane direction can be reconstructed from the two projected displacement fields if the exact position of the cameras with respect to the measurement plane is known (Raffel et al. (2006)). In order to determine the projected displacement fields a mapping function is needed. This mapping function is obtained by a calibration procedure in which a plate with a known pattern and size is imaged by both cameras. Next, the digital self-calibration procedure is applied to further decrease the calibration error.

3.1.5 Tomographic PIV

It is possible to perform a three component measurement with stereoscopic PIV (Arroyo and Greated (1991)), however, the measurement area is still only a plane. Tomographic PIV allows to perform experiments on a volume (Elsinga et al. (2008)) and leads to obtain the velocity field in the entire volume surrounding the flow field (3D-3C). The principle behind tomographic PIV is shown in figure 3.5.

In tomographic PIV, the particles are not illuminated in one specific plane but in a volume. A minimum of three cameras are used to record the scatter light of the particles. Tilt adapters are used to account for the misalignment between the object midplane and the image plane (Scheimpflug condition). The depth of focus is adjusted by the f-number in such a way that the particles are in focus in the entire volume. The two dimensional images recorded by the cameras are converted to a three dimensional array light intensity discretized over voxels by the tomographic reconstruction algorithm MART. This volume reconstruction brings along an undesired effect, namely the emergence of ghost particles (Scarano (2013b)). Such a ghost particle is observed when the lines of sight of all cameras for actual particles intersect at a point in the object space. In order to know the amount of ghost particles in the reconstructed volume, the reconstruction signal to noise ratio (SNR) can be estimated by reconstructing a domain larger than the illuminated volume. Since these ghost particles will be formed everywhere in the reconstructed domain, the intensity level outside the measurement domain will give an indication on the amount of ghost particles inside the measurement domain.

The relation between object space and image space is defined by a two step calibration procedure due to the required accuracy of tomographic PIV is in the order of a fraction of a voxel. Firstly, a geometrical calibration similar to stereo PIV is performed, followed by a volumetric self-calibration Wieneke (2008a). Self-calibration uses triangulation to determine the 3D position of matching particles. The mapping function of all cameras is then corrected by the found residual triangulation error.

Next, when the tracer particles are inside the measurement volume, images are acquired in time-resolved mode. These images are then used to reconstruct the positions of the particles based on the calibration. Once the particle positions are obtained in the 3D space at each time instant, a 3D cross-correlation algorithm yields the velocity vectors by finding average displacements in each interrogation window.

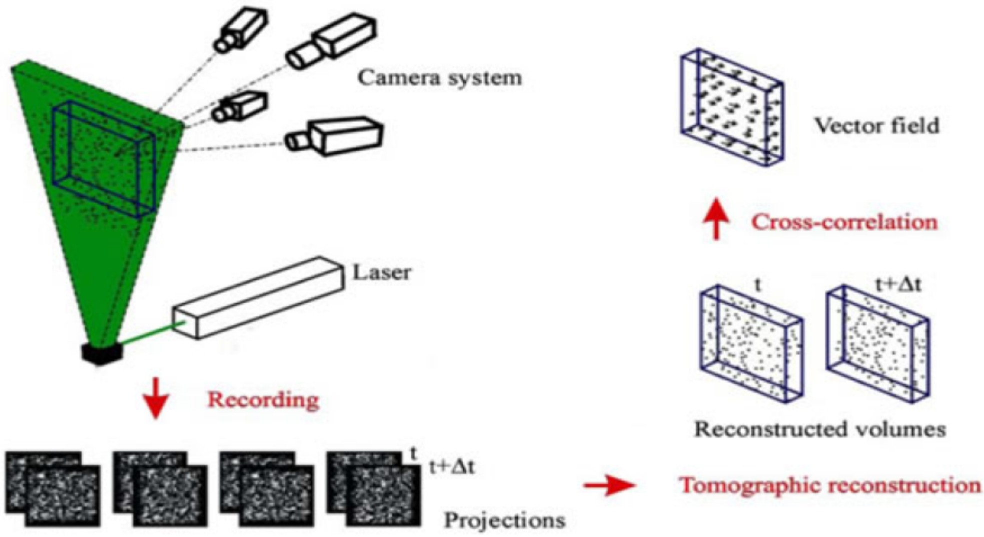

Figure 3.5: Schematic of a tomographic PIV measurement system. Elsinga et al. (2006)

3.2 Loads Determination from PIV

This section describes the approach that is used to calculate the time-average drag on a moving body at a constant speed from the velocity statistics in a wake plane. The forces acting on a body can be calculated by the momentum flux and the pressure in flow field around it. (Anderson (2001)). A schematic representation of the control volume approach is illustrated in figure 3.6. For an incompressible flow, the instantaneous value of the integral drag force, $D(t)$, experienced by the object in a fixed control volume, can be written as:

$$D(t) = -\rho \oiiint_V \frac{\partial u}{\partial t}\, dV - \rho \oiint_S (\mathbf{V} \cdot \mathbf{n}) u \, dS - \oiint_S ((p\mathbf{n} - \tau\mathbf{n})\, dS)_x \tag{3.9}$$

where ρ is the density, V is the control volume, $\mathbf{V}$ is the velocity vector, S is the outer contour and $\mathbf{n}$ is its outward normal vector, p is the pressure, and τ is the viscous stress. The contour $abhi$ in figure 3.6 describes the control volume S, which has to fulfil the following criteria:

1. Segments ai and bh are perpendicular to the flow direction and they need to be sufficiently up- and downstream of the object.

2. Segments ab and ih are streamlines far away from the body.

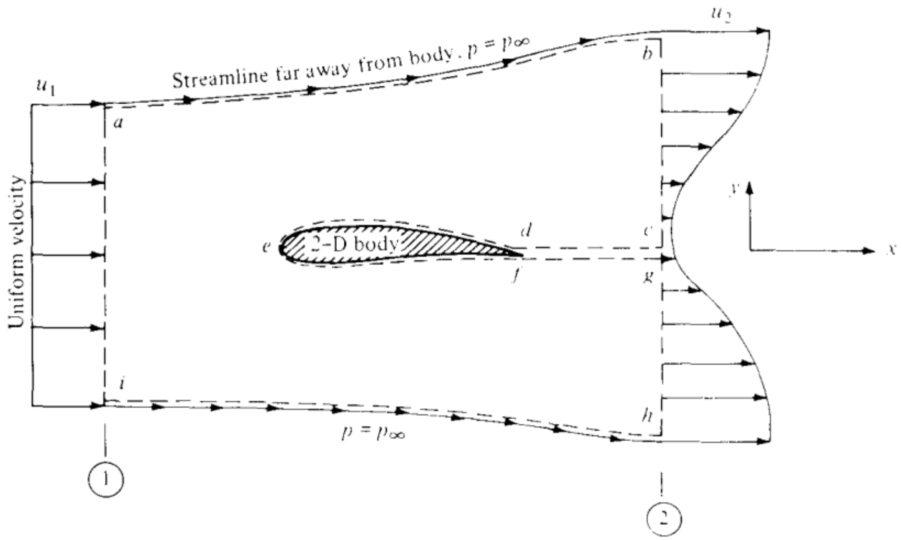

Figure 3.6: Illustration of the control volume approach. Anderson (2001)

The incoming flow U_∞ in figure 3.6 is assumed to be uniform and the flow leaving the control volume is non-uniform due to the presence of the wake of the body. When the earlier mentioned criteria are satisfied in three dimensions (figure 3.6 only shows two dimensions), the viscous stress can be neglected (Kurtulus et al. (2007)). Furthermore along the boundaries ab and ih, $\mathbf{V} \cdot \mathbf{n} = 0$ and the pressure force ($\iint p\, dS$) can be neglected. This simplifies equation 3.9 to:

$$D(t) = -\rho \oiiint_V \frac{\partial u}{\partial t}\, dV + \rho \left(\iint_{S_{ai}} {U_\infty}^2\, dS - \iint_{S_{bh}} u^2\, dS \right) + \left(\iint_{S_{ai}} p_\infty\, dS - \iint_{S_{bh}} p\, dS \right) \tag{3.10}$$

Applying conservation of mass for a control volume and multiplying by U_∞ ($\iint_{ai} \rho {U_\infty}^2\, dS = \iint_{bh} \rho U_\infty u\, dS$) lets us further simplify equation 3.10 to:

$$D(t) = -\rho \oiiint_V \frac{\partial u}{\partial t}\, dV + \rho \iint_{S_{bh}} (U_\infty - u) u\, dS + \iint_{S_{bh}} (p_\infty - p)\, dS \tag{3.11}$$

This expression allows to derive the instantaneous drag of a model from the velocity and pressure statistics in the stationary wake volume, so in a frame of reference moving with the model. In the present experiments, the drag on a transiting model at a constant speed U_M, needs to be computed in a fixed (laboratory) frame of reference. In that case the following changes have to be made to equation 3.11: $U_\infty = U_{env} - U_M$ and $u = u - U_M$ (Ragni et al. (2011)), where U_{env} is the streamwise environmental velocity in the measurement plane prior to the passage of the body and u is the streamwise velocity in the measurement plane after the passage of the body. Ideally the environmental is fully stagnant ($U_{env} = 0$); however, in practise velocity fluctuations are present requiring the measurement of the flow prior to the models passage. Equation 3.11 can be rewritten into:

$$D(t) = -\rho \oiiint_V \frac{\partial u}{\partial t}\, dV + \rho \iint_{S_{bh}} ((U_{env} - U_M) - (u - U_M))(u - U_M)\, dS + \iint_{S_{bh}} (p_\infty - p)\, dS \quad (3.12)$$

which can be simplified to:

$$D(t) = -\rho \oiiint_V \frac{\partial u}{\partial t}\, dV + \rho \iint_{S_{bh}} ((u - U_{env})(U_M - u)\, dS + \iint_{S_{bh}} (p_\infty - p)\, dS \quad (3.13)$$

This equation gives the instantaneous drag force acting on the model. However, in some cases we are more interested in the time-averaged drag force that acts on the model. To come to this, two possible approaches can be followed; one is computing the different instantaneous drag forces over time (neglecting the unsteady term $\frac{\partial u}{\partial t}$) and average over them. A second way to compute the time-average drag force is by decomposing equation 3.13 into the Reynolds average components ($u = \bar{u} + u'$) and averaging both sides of the equation:

$$\overline{D} = \rho \iint_{S_{bh}} (\bar{u} - \overline{U_{env}})(\overline{U_M} - \bar{u})\, dS - \rho \iint_{S_{bh}} \overline{u'^2}\, dS + \rho \iint_{S_{bh}} \overline{u'U'_{env}}\, dS + \rho \iint_{S_{bh}} \overline{u'U'_M}\, dS$$
$$- \rho \iint_{S_{bh}} \overline{U'_M U'_{env}}\, dS + \iint_{S_{bh}} (p_\infty - \bar{p})\, dS \quad (3.14)$$

where $\bar{u}$ is the mean flow component in the wake, u' is the fluctuating component of the streamwise velocity in the wake, U_{env} is the mean flow component in the freestream, and U'_{env} is the fluctuating component of the streamwise velocity in the freestream. Three major contributors to the drag can be seen in equation 3.14:

1. Momentum term: $\rho \iint_{S_{bh}} (\bar{u} - \overline{U_{env}})(\overline{U_M} - \bar{u})\, dS$
2. Reynold stresses: $\rho \iint_{S_{bh}} (-\overline{u'^2} + \overline{u'U'_{env}} + \overline{u'U'_M} - \overline{U'_M U'_{env}})\, dS$
3. Pressure term: $\iint_{S_{bh}} (p_\infty - \bar{p})\, dS$

The momentum term is expected to have the biggest contribution to the drag, followed by the Reynold stresses since they are the result of turbulence in the flow. Experiments by Terra et al. (2017) showed that the pressure term in the wake survey plane can be neglected when it is taken sufficiently downstream (further than five length scales). For this thesis drag will always be computed further than five length scales in the wake and for that reason the pressure term will be neglected in equations 3.13 and 3.14. Results from both approaches will be compared in chapter 6.

Chapter 4

Data Reduction and Analysis

4.1 Data Reduction

The raw images acquired during the experiment were processed with LaVision DAVIS 8.3 software. Transforming the image recordings into the final velocity vector fields is done in multiple stages. A first step is calibration, consisting of a physical calibration and a self-calibration. The different steps following calibration are: image enhancement/pre-processing, tomographic volume reconstruction (only for tomographic PIV), cross-correlation between images and finally post-processing of the vector fields. An illustration of these different steps is given in figure 4.1.

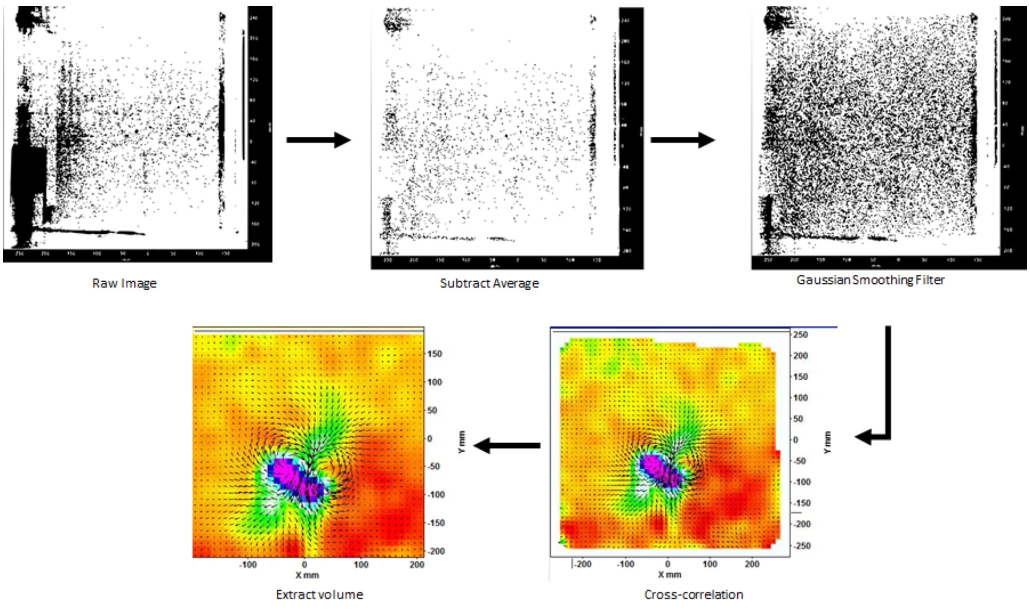

Figure 4.1: Processing steps from raw images to final velocity vector fields.

4.1.1 Calibration

Calibration is used to define an accurate relation between the object space and image space. To obtain this relation, a two step calibration is performed.
Firstly a geometrical calibration in which images of a calibration plate with a known pattern and size are taken. For tomographic PIV calibration, multiple planes in depth are needed to map the whole volume, for stereoscopic PIV images at one plane are sufficient.
The next step further improves the current mapping function by iteratively applying a self-calibration procedure. In the case of stereoscopic PIV, the self-calibration cross-correlates real particle images in order to correct for differences between calibration plate and laser sheet (Wieneke (2005)). The volume self-calibration (Wieneke (2008b)) for tomographic PIV is a bit different. The algorithm makes use of triangulation of particles that were selected based on their brightness. The first step is calculating the forward-projection of the position of the chosen particles in camera one. These locations are then projected back to the next camera. This back-projection forms an epipolar line and around this line a search radius is setup. All particles that fall into the search area are marked as possible candidates. To further reduce the possible matches, this operation is repeated for all the following camera's. When a particle is matched in all cameras, least squares triangulation determines its location in physical coordinates. These coordinates are back-projected to the cameras and a disparity is found between the particle image location and the back-projected physical location. The last two steps are schematically represented for four cameras in figure 4.2.

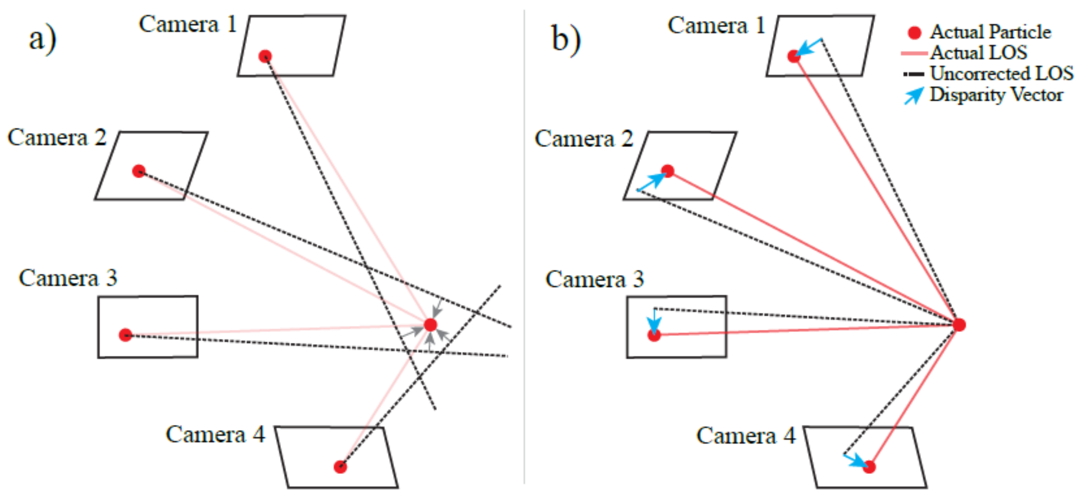

Figure 4.2: The two primary steps of the VSC procedure. a) Least-squares particle triangulation from the uncorrected lines-of-sight; b) backprojection of the triangulated particle position and determination of disparity vector. (Lynch (2015))

4.1.2 Pre-processing

The raw images that were acquired contain background noise arising from object reflections and shadows. Most of these and other kinds of noise can be filtered by image pre-processing, if the reflection however is so strong that it saturates the pixel of the sensor, tracer particles cross this pixel are not imaged and thus cannot be resolved. For this reason such strong reflections should be avoided before starting to acquire. The recordings are pre-processed by performing an average intensity subtraction over time.

4.1.3 Processing

The images from the small-scale experiment and full-scale experiment are acquired from respectively tomographic PIV and stereoscopic PIV. This means that two different processing techniques are needed in order to calculate the vector fields from the acquired images.

Sequential Motion Tracking Enhancement

In case of the small scale experiment the acquired images are analysed by the Sequential Motion Tracking Enhancement algorithm implemented in DaVis 8.3.1. In comparison to stereo and planar PIV, for tomographic PIV an extra step is needed before the images can be analysed, namely a volume reconstruction. The volume reconstruction and cross-correlation are performed with one algorithm, the Sequential Motion Tracking Enhancement (SMTE) algorithm. In this time-marching algorithm, volume reconstruction and cross-correlation are repeated in an iterative procedure whereby the reconstructed volume is based upon an enhanced guess from the last iteration and makes an improved initial guess for the reconstruction at the next time step.
This method has a few advantages compared to the popular MART-algorithm (Lynch (2015)). Firstly, its computational costs is below that of the regular MART-algorithm because fewer MART iterations are required at each time step. Secondly, SMTE is most suited for time-resolved PIV since it only reach convergence after five to ten snapshots. And finally, SMTE is superior to MART in reconstruction quality (in terms of ghost intensity suppression and enhancement of actual particles reconstruction)and measurement precision.

Sliding sum-of-correlation

In case of the full-scale experiment the acquired images are analysed by the sliding sum-of-correlation algorithm proposed by Meinhart et al. (2000) and implemented in DaVis 8.3.1. The velocity differences in the acquired data from the full-scale experiment were rather big, which led to velocity fields full of empty spots when a standard correlation algorithm was used. The Sliding sum-of-correlation algorithm, shown graphically in figure 4.3, calculates the instantaneous correlation functions between image A_i and image B_i with

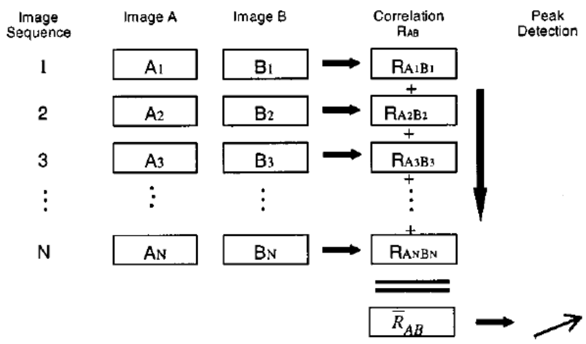

Figure 4.3: Scheme of the Sliding sum-of-correlation algorithm (Meinhart et al. (2000)).

a known time separation Δt. This correlation function is calculated for N sequences of two image pairs. The average of these instantaneous correlation functions over N realizations is calculated by the following equation:

$$\overline{R_{AB}}(s) = \overline{\int\int A(\mathbf{X})B(\mathbf{X}{+}\mathbf{s})d^2\mathbf{X}} = \int\int \overline{A(\mathbf{X})B(\mathbf{X}{+}\mathbf{s})}d^2\mathbf{X} \tag{4.1}$$

It has been proven by Meinhart et al. (2000) that by averaging over the instantaneous correlation functions before signal peak detection, higher quality velocity data can be obtained with less than 0.51 percent erroneous measurements.

4.1.4 Post-processing

Typically the resulting vector field contains outliers and in order to correct for these outliers, post-processing on the vector fields is performed.
A first post-processing algorithm that is applied is the Universal Outlier Detection algorithm. This median based filter, introduced by Westerweel and Scarano (2005), is specifically dedicated to PIV data. The residuals are normalised w.r.t. the median residual:

$$r_0{}^\star = \frac{|U_0 - U_m|}{r_m + \epsilon} \tag{4.2}$$

where U_m is the velocity median, $|U_0 - U_m|$ is the velocity residual r_i and r_m is the median value. Finally ϵ is the minimum acceptable fluctuation level in the measurement data. This filter can be applied to highly turbulent and to laminar flow regions.
A second step in the post-processing is to deal with the empty spaces that may occur in the data set. A linear interpolation is performed over these empty spaces to have a continuous data set.
Finally a second order polynomial is fitted for each vector using a specified amount of neighbouring vectors in all directions. The central vector is then replaced by the value of the fitted polynomial at that central position. This polynomial filtering operation preserves minima and maxima better than Gaussian smoothing.

4.2 Analysis Techniques

In this section the different analysis techniques that were used to analyse the velocity data are briefly discussed. The results of this analysis can be found in the results chapters (chapter 6 and chapter 7).

4.2.1 Drag Computation from Control Volume Approach

Drag from the velocity fields is obtained from the control volume approach for drag computation from PIV data, developed by van Oudheusden et al. (2007). As was discussed in chapter 3, the time-averaged drag force can be computed from instantaneous velocity fields (equation 4.3) as well as from time averaged velocity fields (equation 4.4).

$$\overline{D(t)} = \overline{\rho \iint_{S_{bh}} ((w - U_{env})(U_M - w)\, dS} \tag{4.3}$$

$$\overline{D} = \rho \iint_{S_{bh}} (\overline{w} - \overline{U_{env}})(\overline{U_M} - \overline{w})\, dS - \rho \iint_{S_{bh}} \overline{w'^2}\, dS + \rho \iint_{S_{bh}} \overline{w'U'_{env}}\, dS + \rho \iint_{S_{bh}} \overline{w'U'_M}\, dS - \rho \iint_{S_{bh}} \overline{U'_M U'_{env}}\, dS \tag{4.4}$$

where $\overline{w}$ is the time-averaged streamwise velocity in the wake, w' is the fluctuating component of the streamwise velocity in the wake, $\overline{U_{env}}$ is the time-averaged streamwise velocity in the freestream, U'_{env} is the fluctuating component of the streamwise velocity in the freestream, U_M is the velocity of the model and ρ is the air density.
As was discussed in chapter 3 the pressure term can be neglected when measuring far enough in the wake and so the time-averaged drag force can be determined solely from the momentum term and the Reynolds stresses.

Momentum Term

The momentum term is obtained by integrating the momentum deficit experienced by the flow. In a windtunnel it is sufficient to measure the velocity field in the wake of the object and correct for the freestream velocity of the windtunnel to get the momentum deficit. As was discussed in chapter 3, the freestream velocity in the moving frame of reference is derived from the relative velocity between the body and the environment ($U_\infty = U_{env} - U_M$). In an ideal world the environmental flow would be perfectly quiescent ($U_{env} = 0$). During real experiments U_{env} is however never zero and thus cannot be neglected. For that reason the environmental flow prior to the passage of the model is measured for every run. Figure 4.4 shows the effect of subtracting the environmental flow.

Reynolds Stress Term

The Reynolds stresses are a result of the Reynolds decomposition and time averaging of the continuity and the momentum equations. The fluctuating part of each velocity component is used to determine these Reynolds stresses. The time-averaged Reynolds stresses seen in equation 4.4 are generated by the fluctuating streamwise velocity components in the environment, wake and model velocity. Two of the time-averaged Reynolds stresses appear to contribute to the drag where the other two appear to reduce the drag. In order to obtain the total contribution of the Reynolds stress term in the drag equation, all these Reynolds stresses need to be summed up.

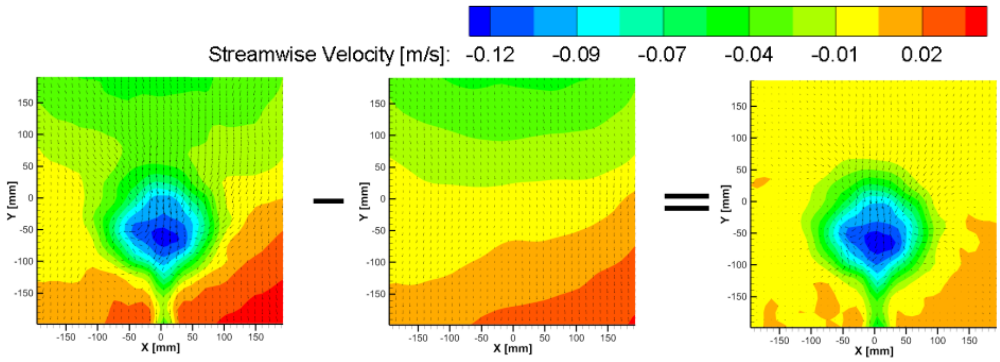

Figure 4.4: Effect of environmental conditions on the momentum deficit in the wake. Left: Flow field in the wake without taking environmental flow into account; Middle: Environmental flow field; Right: Momentum deficit in the wake, taking environmental flow into account.

4.2.2 Vorticity

Vorticity is an important property to obtain information about the fluid circulation and is defined as the curl of the velocity vector field. The equation of the vorticity $\vec{\omega}$ is shown below:

$$\vec{\omega} = \nabla \times \vec{u} = \begin{pmatrix} \frac{\partial w}{\partial y} - \frac{\partial v}{\partial z} \\ \frac{\partial u}{\partial z} - \frac{\partial w}{\partial x} \\ \frac{\partial v}{\partial x} - \frac{\partial u}{\partial y} \end{pmatrix} \tag{4.5}$$

It is important to note that the presence of vorticity does not necessarily mean that there is a vortex. Vorticity as defined by equation 4.5 cannot differentiate between a shear layer and a vortex because it is solely based on velocity gradients. A better, more suitable criteria to identify vortices, is the Q-criterion.

4.2.3 Q-criterion

To make a distinction between vorticity magnitude and shear strain-rate the Q-criterion uses the second invariant of the velocity tensor $\nabla\vec{u}$.

$$\nabla\vec{u} = \frac{\partial u_i}{\partial x_y} = S_{ij} + \Omega_{ij} \tag{4.6}$$

As is seen in equation 4.6 the tensor can be decomposed into a symmetric (S) and antisymmetric (Ω) part. Both tensors are defined by the following two equations:

$$S = \frac{1}{2}(\nabla\vec{u} + \nabla\vec{u}^T) \tag{4.7}$$

$$\Omega = \frac{1}{2}(\nabla\vec{u} - \nabla\vec{u}^T) \tag{4.8}$$

These two tensors are used to define Q:

$$Q = \frac{1}{2}(||\Omega||^2 - ||S||^2) \tag{4.9}$$

Equation 4.9 is a measure of the local balance of the magnitude of vorticity versus the shear-strain rate. For values of $Q > 0$ the circulation outweighs the shear and vice versa. Thus, a vortex is present if Q has a positive value, otherwise it there is a shear layer present.

4.2.4 Phase-Averaging

In order to compare the wake flow topology throughout one dynamic pedal stroke to the wake measurements performed on static leg positions at fixed crank angles, the wake structures which are passing through the measurement plane can be analysed by means of phase-averaging. A phase-averaged velocity field is an average over multiple instantaneous velocity fields, each obtained from different measurement runs, but originating from the same quasi-static leg position. The procedure that connects the correct image in the wake to the crank angle of interest is schematically presented in figure 4.5 and is described in detail below.
The first step in finding the image belonging to the quasi-static leg position of interest is to determine the crank angle at position $T = 0$ in figure 4.5 and determine its difference with the crank angle of interest. With the difference in crank angle known, it is possible to calculate the location of the cyclist at which he had the correct leg position for the last time ($T = -1$ in figure 4.5). At an assumed average convection velocity of $0.61U_{cyclist}$ (Crouch et al. (2016a)), the time (and amount of frames) it takes the flow structures at location $T = -1$ to convect upstream to the measurement plane, can be calculated. The flow structures will arrive there at $T = 1$, and as seen in figure 4.5, the cyclist by then already passed the measurement plane and thus will not be interfering with the flow.

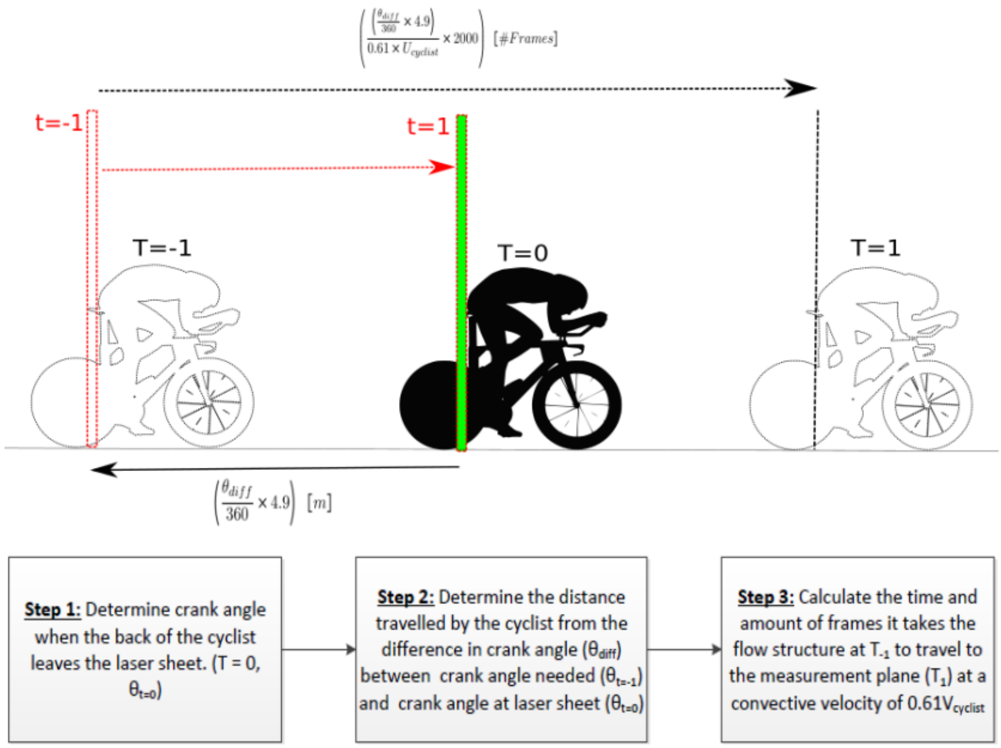

Figure 4.5: schematic of the Phase-locking procedure

Chapter 5

Experimental setup and Acquisition procedure

This chapter gives a description of the Experimental setup and the acquisition procedure for both the small-scale as well as the full-scale experimental campaign. First sections 5.1 and 5.2 will elaborate on the small-scale experiment, after which sections 5.3 and 5.4 discusses the full-scale experiment.

5.1 Setup scaled Ring of Fire

5.1.1 Measurement System and Conditions

In this section a description of the experimental apparatus used for the present experiment is given. In contrast to common practice in aerodynamic research, this experiment has not been performed in a windtunnel, but in a tailor made system. Figure 5.1 gives a schematic representation of the system and figure 5.2 shows a picture of the setup. The model was towed through a 170cm long duct with a cross section of $50x75cm^2$. The duct was equipped with optical access for illumination and imaging, a slot through which the HFSB could be inserted and finally also some doors in order to constrain the bubbles.
The model is a smooth styrofoam sphere with a diameter of 10cm. It is supported by a $20cm$ long, 3cm wide aerodynamic strut with a thickness to chord ratio of 15%. The strut is mounted on a carriage which is towed at constant speed on a rail placed below the bottom wall of the tunnel. The model is towed by a digitally controlled electro motor. The experiment was conducted at five different model velocities. These velocities were set by setting the qc/ms (absolute position over time) of the motor. During the towing, the string was winded around a pulley, however, this process was not identical for every run, which led to small variations in speed. For this reason camera 4 (figure 5.2) was used to accurately

measure the speed of the model per run. A summary of the velocity measurements on each of the five sets is presented in table 5.1.

Table 5.1: Velocity data of the model

Motor setting [qc/ms]	Number of runs	Average velocity [m/s]	One Standard Deviation [m/s]	Reynolds number
106	60	1.076	0.015	7173
119	58	1.212	0.018	8080
132	54	1.336	0.020	8907
146	60	1.476	0.011	9840
160	60	1.622	0.015	10813

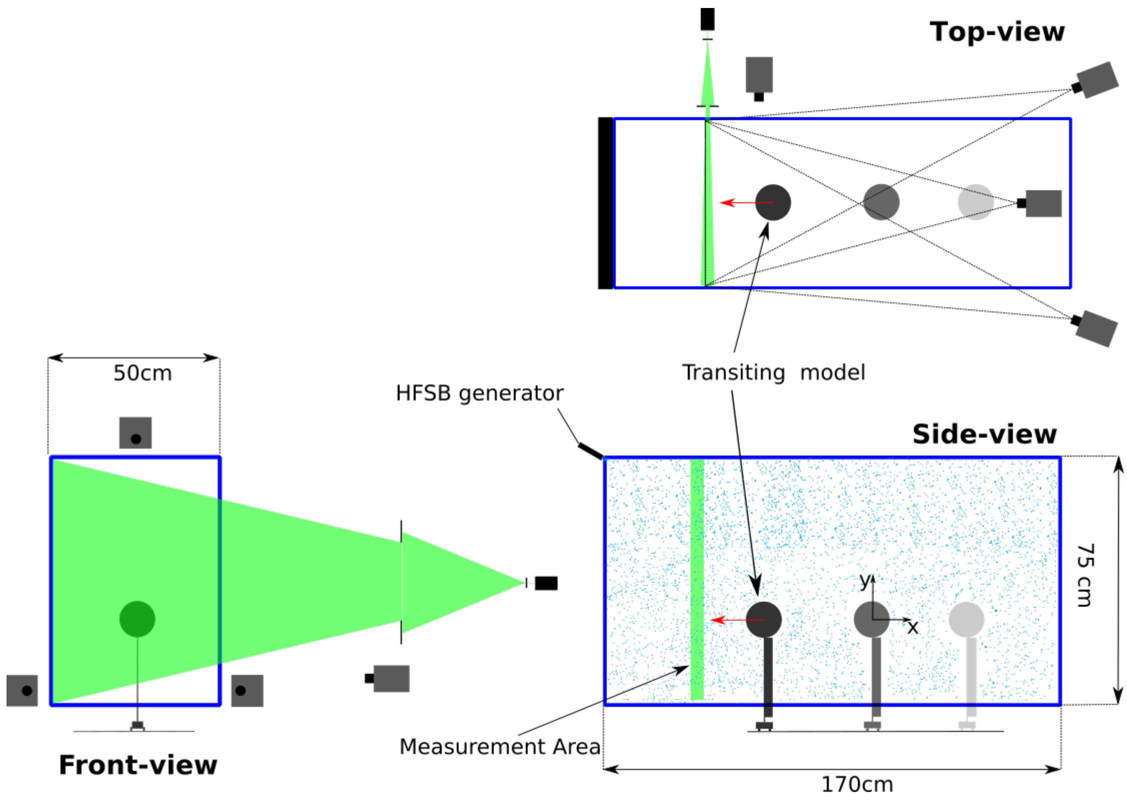

Figure 5.1: Schematic of a setup

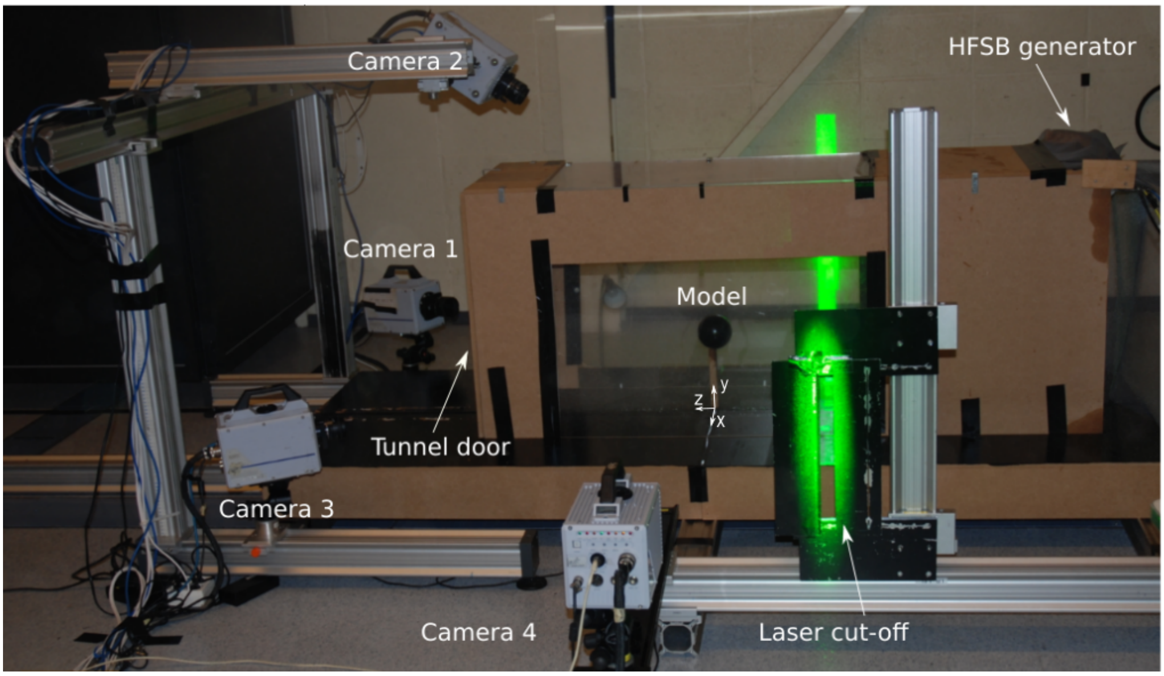

Figure 5.2: Picture of a setup

5.1.2 Tomographic System

In the same way as in the experiments of Terra et al. Terra et al. (2017) time-resolved tomo-PIV measurements have been conducted. A Quantronix Darwin Duo Nd:YAG laser was used for illuminating the measurement area. At a frequency of 1kHz this laser has a nominal pulse energy of 25mJ. Shaping the laser beam into a conical volume was done by a set of spherical and cylindrical lenses. A rectangle of 50cm by 3cm was then cut-out from the elliptical cross section with a light cut-off plate (figure 5.2). The size of the illuminated measurement volume was approximately $50 \times 50 \times 4cm^3$.
The imaging system comprises three Photron Fast CAM SA1 cameras with a resolution of 1024 x 1024 pixels and a pixel pitch of $20\mu m$. Camera 1, 2 and 3 as numbered in figure 5.2 were equipped with respectively a 60mm, a 35mm and a 50mm Nikon lens. For each lens the f-stop was set to f/5.6. Tables 5.2 and 5.3 summarize the specifications of laser and cameras. As mentioned in chapter 3, HFSB were used as tracer particles during the current experiments. They are produced by a wing shaped rake containing ten nozzles. Inside the nozzle the helium, soap and air come together to form bubbles. The fluid flow rates of all three fluids determines the size of the bubbles. This is regulated by a Fluid Supply Unint (FSU), which is provided by LaVision GmbH. At optimal conditions one nozzle generates about 30.000 bubbles per second. The bubbles are inserted at the top end of the tunnel under a small angle, as seen in figure 5.1.
Assuming the earlier described conditions, the seeding density is approximately 3 particles/cm^3 which is equal to 0.04 particles/pixel. PIV acquisition is performed within LaVision Davis 8.3.1 at a frequency of 500 Hz.

Table 5.2: Laser specifications

Quantronix Darwin Duo Nd:YAG laser	
Laser type	Nd:YLF diode pumped
Wave length	527 nm
Pulse energy @1kHz	25 mJ
Pulse repetition rate	0.1-10kHz

Table 5.3: Camera specifications

Photron Fast CAM SA1.1	
Sensor resolution	1024 x 1024 pxl
Pixel size	20 μm
Frame rate (full frame)	5400 fps
Memory capacity	8 GB

5.1.3 Measurement Procedure

As aforementioned, the current experiment was conducted at five different velocities of the sphere (table 5.1). At each nominal model velocity, the experiment was repeated about 60 times. In order to get similar results between different runs, the procedure for conducting a single measurement was pre-described in detail.
At the start of each run the tunnel entrance and exit were closed. The entrance was closed with a wooden door and the exit was closed with a porous material (mosquito net) to avoid overpressure in the duct. The HFSB generator was turned-on and the tunnel started filling up with tracer particles. When, after more or less two minutes, the concentration in the measurements region reached steady-state conditions, the HFSB generator was turned-off. After shutting it down and opening the door, it was necessary to wait 30 seconds to have close to quiescent flow conditions. In order to capture the fully developed wake flow regime past the sphere within the measurement domain, the sphere was put in motion at roughly 40 diameters from the entrance. Last the data acquisition was started. Images were acquired from 3 diameters before passage of the sphere till 8 diameters after passage of the sphere. However, only part of this data was actually stored, namely 20images 2 diameters before the passage of the sphere and the first 7 diameters in the wake of the sphere.

5.2 Data reduction Scaled Ring of Fire

5.2.1 Calibration Procedure

The measured displacements in voxels need to be translated into physical units for further analysis, therefore calibration of the system is a requisite. Next to this, calibration for tomo-PIV also has a second function. It determines the lines-of-sight of each camera throughout the measurement volume, which is essential later on during the volume reconstruction.

Geometrical Calibration

To perform physical calibration of the $50 \times 50 \times 4cm^3$ volume, a type 30 calibration plate was used and its dimensions are shown in table 5.4.

Table 5.4: Geometry Type 30 calibration plate

Geometry Type 30 calibration plate			
Number of planes	2	Mark form	Dot
Width [mm]	300	Mark diameter [mm]	2
Height [mm]	300	Distance mark to mark [mm]	22.5
Thickness [mm]	12	Number of marks in x in each plane	12
Distance plane to plane [mm]	2	Number of marks in y in each plane	12

Images of the plate were taken at three different planes in volume depth (z-direction). One in the middle of the volume ($z = 0mm$), one at the back of the volume ($z = -55mm$) and one at the front of the volume ($z = 55mm$). The plate was translated in z-direction on a beam to acquire images at a constant in-plane position. The calibration was performed using the pinhole camera model of Tsai (1987). This model was chosen for its simplicity and because it describes the cameras positions in terms of physical parameters which are easy to check for correctness.

Volume Self-Calibration

After the physical calibration, the calibration error is still in the order of magnitude of 1 pixel. In order to reduce these errors to below 0.1 pixels, the volume self-calibration of Wieneke Wieneke (2008a) was applied. Firstly the intensity threshold was set to 100 counts, this reduced the amount of used particles under 10,000. An initial search radius of five pixels was chosen and iteratively reduced to one pixel.
Incorrect particle triangulations will generate multiple wrong disparities. Disparities are gathered in bins and within a bin, a peak will form, indicating the most likely disparity. To enhance the disparity peak, and thus making it easier to detect it, 300 images were used. The effect the number of images on the disparity peak is seen in figure 5.3.

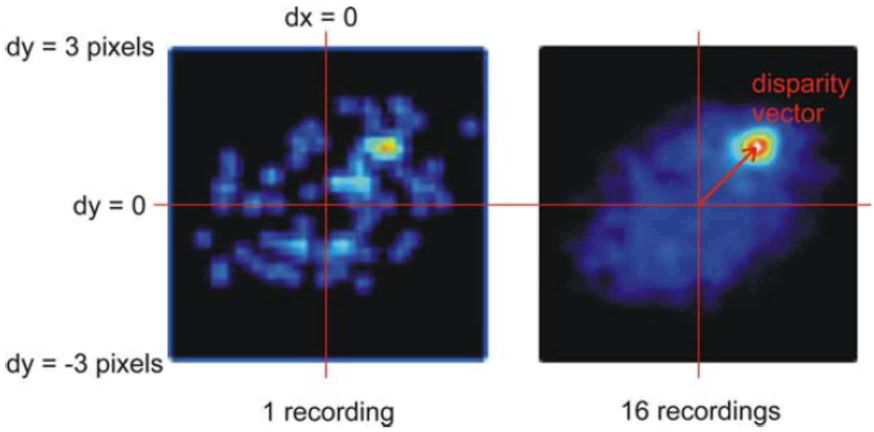

Figure 5.3: Disparity maps for a single image (left) and for 16 images (right).(Elsinga (2008))

5.2.2 Image Pre-processing

The pre-processing consists out of 2 steps, a subtraction of the average to remove reflections and a Gaussian smoothing to further improve the particle images. The applied Gaussian smoothing filter was a 3×3 smoothing filter with a strength of 0.5. After the Gaussian smoothing it is possible to apply a sharpening filter to reduce the ghost intensity level if needed. To check the ghost level intensity and to verify that the final illumination depth is fully illuminated, a z-intensity profile was extracted from a reconstructed object with a larger depth than the measurement region. An average z-intensity profile over 250 reconstructed objects is shown in figure 5.4. The red dashed box in the figure represents the limits of the reconstructed volume in this experiment.

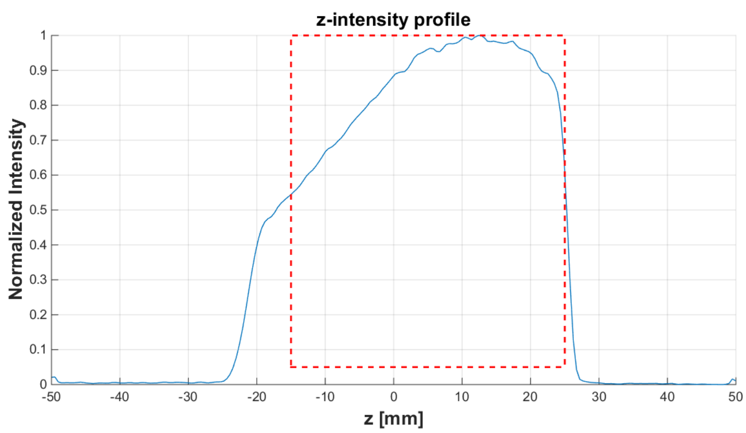

Figure 5.4: Normalized mean z-intensity profile of the reconstructed volume and the limits of the reconstructed volume (red dashed lines)

It is confirmed that the measurement region ($-15mm \leq Z \leq 25mm$) falls completely inside the illuminated region and that there is an excellent Signal to Noise Ratio (SNR)

5.2.3 Sequential Motion Tracking Enhancement

The first step of this two step iterative process, the tomographic reconstruction of the volume, is performed with the MART algorithm as described by Elsinga et al. (2006). Based on the results presented by Lynch (2015), it was chosen to perform five MART iterations. They showed that the quality of reconstruction Q does not improve significantly any more after five MART iterations. The size of the reconstructed volume was $568 \times 549 \times 40$ mm [x × y × z], where the x and y dimensions were set to maximum and the range of depth [z] was chosen to go from -15 till 25 mm.
The particle image density was found to be equal to 0.023 ppp. According to Lynch and Scarano (2015) this means that for a three camera tomographic system the reconstruction quality factor Q is around 0.9. The cross-correlation analysis used interrogation volumes of 96 × 96 × 96 voxels ($43.2 \times 43.2 \times 43.2mm^3$)and an overlap of 75% overlap, which led to 3.3 particles per interrogation region.

5.2.4 Post-processing

To improve the quality of the vector fields post-processing was done. Firstly, the outliers were filtered out by using the universal outlier detection filter (Westerweel and Scarano (2005)). Next the empty spaces were filled by using linear interpolated and finally the edges of the measurement region were cut-off by extracting a volume as seen in the last step of figure 4.1.

5.3 Setup Full-scale Ring of Fire

5.3.1 Cyclist and Bike

In this section detailed information about the cyclist and his bike will be presented. Unfortunately there was a difference in equipment used during both campaigns. The helmet and speed suit worn by the cyclist during the measurements in the OJF and the ones worn during the Ring of Fire measurements were not identical. The helmet that was used, was twice the same model, namely a Giant Rivet TT helmet. However, the helmet used in the OJF is the one used by Team Sunweb in the season 2016- 2017 and the one used during the Ring of Fire experiment was used by Team Giant-Alpecin during the season 2015 - 2016.
The speed suit however, was completely different in both campaigns. During the OJF measurements a long sleeve TT suit from team sunweb (2016-2017) was used and during the Ring of Fire measurements a short sleeve TT suit from Blanco Pro Cycling Team (2013) was used. The main difference between both suits is that the Sunweb suit contains some special aero-

dynamic (rough) fabrics and the Blanco suit is completely made out of a smooth fabric. This means that in theory the Sunweb suit should result in slightly lower drag values at $15m/s$, however, at the velocity in the current study ($8m/s$), this effect can be neglected. All details on the cyclist, the equipment and the bike can be found in table 5.5.

Table 5.5: Cyclist and bike specifications

Details on Cyclist		Details on bike	
Height	184cm	Bike frame	Ridley Cheetah (58cm)
Weight	78kg	Groupset	Ultegra 11-speed
Helmet	Giant Rivet TT	Handlebar	Deda Dabar Bull Horn
Suit[1]	Long sleeve TT suit Team Sunweb / Short sleeve TT suit Team Blanco	Aerobars	Deda Parabolica 2
		Wheels	50mm No Brand carbon clinchers

5.3.2 Ring of Fire

Outdoor Laboratory and Safety

Similar to the scaled experimental setup discussed earlier in this chapter, a tailor made system was build. This system shows a lot of resemblance to the small scaled system, for example the model, in this case the cyclist, needs a long runway to reach the required speed before entering the tunnel. Due to a lack of space inside the High speed lab of the TU Delft, the Ring of Fire setup was build in the backyard of the lab. The biggest difference between the scaled Ring of Fire and this one is that, instead of tomographic PIV, now stereoscopic PIV was used. Performing the experiment outside meant that every day in the morning the whole setup had to be built up and in the night, it needed to be taken apart again. Stereoscopic PIV was chosen over tomographic PIV since the limited thickness of the measurements plane did not allow to capture the out of plane velocity gradients. Next to that it is also a lot less time consuming to setup and calibrate compared to tomographic PIV.
Figure 5.5 gives a schematic representation of the setup and a picture of the setup is given in figure 5.6. The coordinate system was oriented as shown in figure 5.5. The cyclist had a runway of 30 meters to accelerate before entering a six meter long, three meters wide and two meters heigh tent. After exiting the tent there was a 20m long brake zone. The tent was equipped with optical access for illumination by means of a laser cut-off plate at four meters distance measured from the entrance of the tent (see figure 5.6). The laser head was placed at a distance of eight meters perpendicular to this cut-off plate and at a height of roughly 75cm. The cameras were positioned at the entrance of the tent with a view angle of 60° between them. The seeding system was placed inside the tent and pointing towards the laser sheet.

[1]Different suits used at each campaign.

At the entrance of the tent the door was removed (see figure 5.6), but in order to keep the seeding inside the tunnel while filling it, the back door of the tent was kept closed.

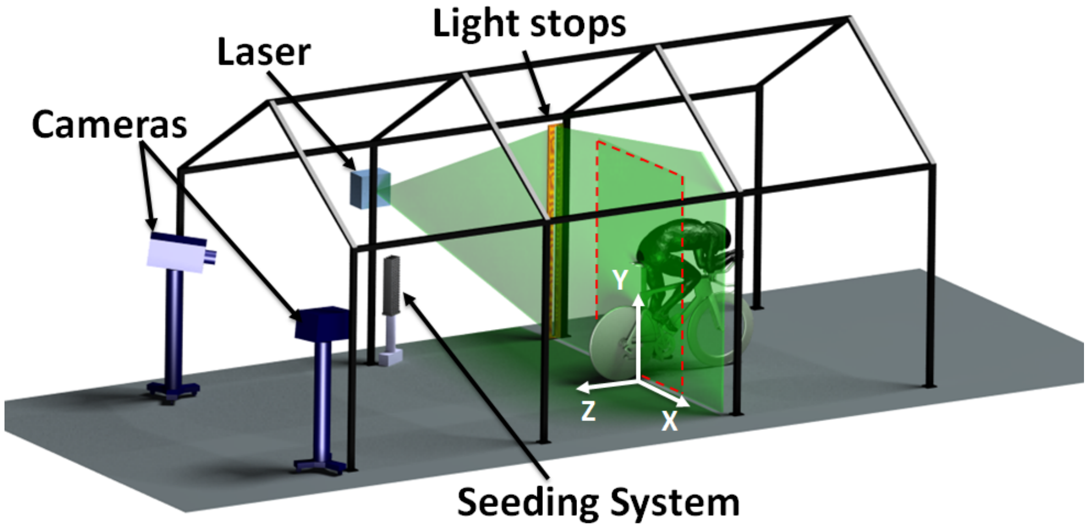

Figure 5.5: Schematic view of the Ring of Fire setup.

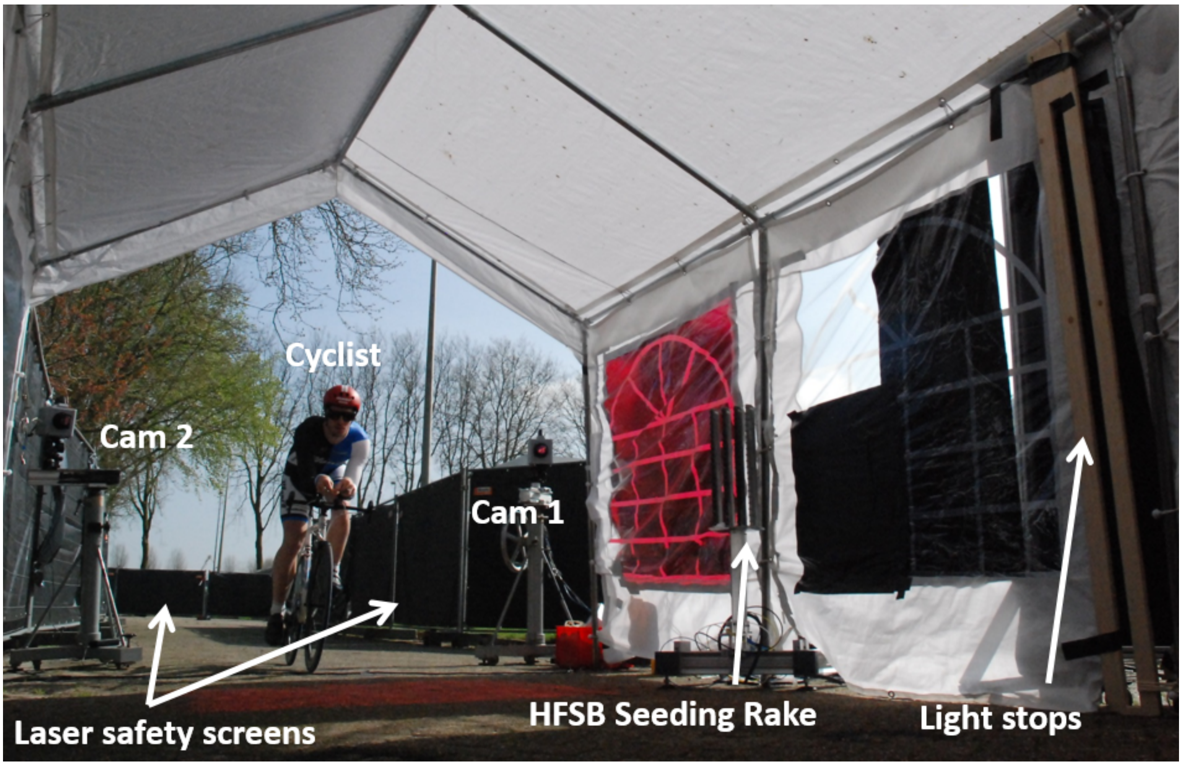

Figure 5.6: Picture of the Ring of Fire setup.

Bringing the setup outside of the controlled lab environment meant that extra care and attention was required regarding safety. The biggest safety hazard for sure was bringing the laser outside. To avoid scattered laser light ending up in the eyes of bystanders, participants or even pilots flying over, the whole area was surrounded by laser safety screens. A few of the screens can be seen in the background of figure 5.6 and a schematic ground plan that shows the locations of all the screens can be seen in figure 5.7. To keep optical access to the measurement region one side of the tent was covered by using a Lee Magenta filter instead of the safety screens. For redundancy, a black foil that blocks the laser light was applied to the windows of the tent and the part of the roof where the laser directly hit.

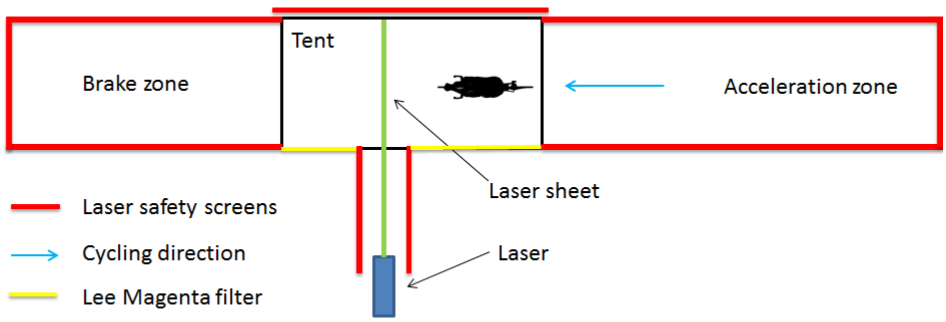

Figure 5.7: Schematic of the setup of laser safety screens during the Ring of Fire measurement campaign (not to scale).

Other safety measures were, among other things, the use of laser safety goggles by all participants, use of mouth caps by all participants to protect against breathing in the HFSB and placement of warning signs at all entrances to the area.

Design of Experiment

This section describes the equipment and parameters that were used for setting up the large-scale Stereoscopic PIV experiment. The field of view was equal to $1000 \times 1700mm^2$ and is shown in figure 5.5 by the red dashed line. The velocity of the cyclist was around $8m/s$, which led to a Reynolds number of 3.17×10^5 based on a torso length of $600mm$.
The PIV equipment consists of the following components; An HFSB seeding system, two high speed cameras, an illumination source, a programmable timing unit and an acquisition computer with DaVis software installed on it. More details on the exact used equipment are presented in table 5.6.
From the laser sheet thickness it follows that the maximum allowed out-of-plane displacement was $7.5mm$ and so, based on a maximum velocity of $15m/s$, it was chosen to acquire images at a frequency of $2kHz$ with an exposure time of $3\mu s$. Both the $1MPx$ high speed cameras were equipped with fixed focal length objectives of $50mm$, daylight filters and with Scheimpflug adapters to account for the angle between the image plane and the object plane. With this objectives installed on the cameras, at a distance of four meters from the measurement plane, the magnification factor was 0.0125. To ensure that the particles are in focus in the entire depth of the volume, the apertures of the cameras were set to a value of $f/5.6$, which was sufficiently above the calculated limit value of $f_{\#} = 1.33$ (based on the depth of field). The

digital image resolution was $1.76mm/px$.

The seeding generator is a four wing rake that contains 80 nozzles. At nominal working conditions each individual nozzle produces $30,000$ particles per second. The total production rate of the system is thus 2×10^6 particles/s. The nozzles are placed in a grid formation, 20 nozzles in vertical direction by 4 nozzles in horizontal direction. With a vertical spacing of $2.5cm$ and a horizontal spacing of $5cm$, the cross sectional area of the seeding generator is $47.5 \times 15cm^2$. A digital Fluid Supply Unit (FSU) provided by LaVision controls the flow rate of the three components of the HFSB. The production rate of the bubbles seemed to be stable at pressures of 1.8 bar for Helium, 3.0 bar for air and 2.7 bar for soap. The particle image diameter for this particular settings of the cameras and seeding rake was calculated by using equation 3.5. The physical particle has a reported diameter of $400\mu m$ (Scarano et al. (2015)), which at a object distance of four meters translates in a particle image diameter of $8.85\mu m$, which is smaller then the pixel pitch of $20\mu m$.

Table 5.6: Equipment used for large scale stereoscopic PIV experiment

Illumination		Imaging	
Laser	Quantronix Darwin Duo Nd:YAG laser	High speed Cameras	Photron Fast CAM SA1.1
Wave length	527 nm	Sensor resolution	1024 x 1024 pxl
Pulse energy @1kHz	25 mJ	Pixel size	20 μm
Pulse repetition rate	0.1-10kHz	Frame rate (full frame)	5400 fps
Optics	Cylindrical and spherical lenses	Memory capacity	8 GB
		Objectives	2× Nikon $f = 50mm$
Seeding		**Data collection**	
Tracer particles	Helium Filled Soap Bubbles (HFSB)	software	DaVis v8.3.1 - LaVision
HFSB generator	Fluid Supply Unit (FSU) - LaVision	Computer	Acquisition computer - LaVision
Seeding Rake	80 nozzles divided over 4 vertical wings		
Timing			
Programmable Timing Unit (PTU)	High Speed Controller - LaVision		

Measurement Procedure

The experiment was conducted at two different cycling positions, a time trial position and an upright position. The cyclist was asked to go through the tunnel twenty times in both positions with a constant velocity of $8m/s$. The exact velocity in the measurement area was measured per run by the two cameras at the entrance of the tunnel. Table 5.7 presents the details on the velocity measurements.

Table 5.7: Velocity data Full-scale Ring of Fire

Time trial Position		Upright Position	
Number of runs	20	Number of runs	20
Mean velocity[m/s]	8.35	Mean velocity [m/s]	8.41
Standard deviation[m/s]	0.79	Standard deviation[m/s]	1.05

As was the case for the scaled experiment, also here the differences between individual runs should be minimized to be able to compare them to each other. For that reason a detailed description of the procedure for conducting a single measurement was created.
At the start of each measurement, the exit in the back of the tent was closed off by the tent sail. The HFSB generator was turned-on and the tent started filling up with tracer particles. When the seeding in the measurement sheet was sufficiently high, a sign was given to the cyclist to start. At that time the back door was opened and data acquisition started. As was the case in the small experiment, also here only part of all the acquired data is stored. In the freestream, 600 images before the passage of the cyclist, 100 images are saved and in the wake 2300 images are stored, starting from the moment the athlet′s back leaves the measurement area. During the whole measurement the seeding system kept on producing bubbles to maintain the seeding density in the tunnel.
Since the cyclist was peddling during the runs it was important to define a reference frame for the crank angles. The 0° crank position corresponds to the crank being horizontal, with the right leg forward and the left leg back.

5.3.3 Open-Jet Facility

The measurement campaign in the Open Jet Facility (OJF) was performed in order to determine a reference drag value to compare to the Ring of Fire measurements. It is an atmospheric closed-loop windtunnel with an open test section. The tunnel exit has an octagonal shape with a dimension of $2.85 \times 2.85m^2$. A 500kW electric motor is installed to run a fan that can generate wind speeds upto 35m/s in the test section. In order to reduce the turbulence level in the test section, the settling chamber is equipped with five dense wire meshes. The smooth flow is then passed through a contraction into the test section. The turbulence levels in the test section have been found to be 0.5% of the velocity (Hoekstra). Behind the test section the air is cooled by a 350kW radiator to maintain a constant temperature. A schematic representation of the OFJ-TUD is given in figure 5.8.

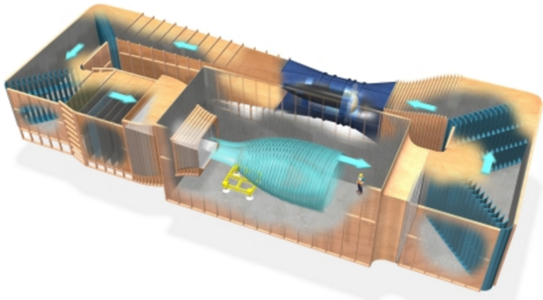

Figure 5.8: Schematic view of the Open Jet Windtunnel Facility of the TUD.

The balance used for drag measurements was an external 6-component balance build by NLR. The maximum nominal load range of the axial force (drag force) is $F_x = \pm 250N$ with a maximum error of 0.06%. On top of this balance, a platform was build and connected to the end of the contraction. The platform simulates the road on which the cyclist rides. As is seen in figure 5.9, the bike is mounted on top of it, and in the same time connected to the balance by four vertical struts, two connected to the front axle and two connected to the rear axle.

Figure 5.9: Cyclist in OJF.

The measurements were performed at six different velocities: from $6m/s$ till $11m/s$ with an increment of $1m/s$. At every velocity, the drag at four different leg positions was measured. Two asymmetric leg positions, one where the left crank is pointing downwards and the other one with the right crank down, and two symmetric leg positions, one with the left crank to the front and the other with the right crank to the front. Per velocity an average was computed over the four positions to get to the final drag force and drag area (C_DA). This set of measurements were performed in time trial position.

5.4 Data reduction Full-scale Ring of Fire

5.4.1 Calibration Procedure

Geometrical Calibration

A scaled-up version of this calibration plate was used. With exception of the thickness, the dimensions of the plate were four times bigger than the Type 30 plate. The exact dimensions of this "BIG" calibration plate are given in table 5.8. For the geometrical calibration the pin-hole model was used.

Table 5.8: Parameters of calibration plate "BIG"

Width [mm]	1200	Number of marks X	13
Height [mm]	1200	Number of marks Y	12
Thickness [mm]	40	Mark size [mm]	8
Plane to plane distance [mm]	20	Mark to mark distance [mm]	90

Self-Calibration

To perform a self-calibration the entire measurement region was filled with tracer particles and a set of 220 images were acquired at a frequency of 2kHz. The wind that blew through the tent produced enough turbulence in order for the self-calibration to be performed. The measurement plane was divided into interrogation windows of $32 \times 32px$ with an overlap of 75%. The self calibration procedure (Wieneke (2008b)) decreased the maximum disparity error from 0.6px to 0.1px.

5.4.2 Image Pre-processing

Figure 5.10(a) shows an example of a raw image. A lot of background noise and reflections are observed and as mentioned earlier, these should be avoided as much as possible. The recordings are pre-processed by performing an average intensity subtraction over time. After applying this filter the background noise was reduced to less than 10 counts and the averaged light intensity of the brightest particles was somewhere in the region of 100 to 150 counts, resulting in an image SNR of about 10. The result of the filter on figure 5.10(a) can be seen in 5.10(b).

5.4.3 PIV Time-series Sliding Sum-of-Correlation

By using sliding sum of correlation the velocity vector fields were determined from the average over seven consecutive correlation maps (obtained from eight images) which were calculated between two images with a time separation of $2 \times 10^{-3}s$ (four frames). The particle image density was 0.09 ppp, with interrogation windows of 64×64 pixels ($113 \times 113mm^2$) and an overlap of 75%, this led to 23.04 particles per interrogation region and one vector every $28mm$. The largest observable length scale with this setup was $1800mm$, the smallest was $28mm$ (size of an interrogation window), which results in a Dynamic Spatial Ratio of $\approx 60 : 1$. The Dynamic Velocity Range, which is defined as the ratio of the maximum measurable velocity to the minimum resolvable velocity (Raffel et al. (2006)), is found to be $\approx 100 : 1$. The maximum measurable streamwise velocity here is $15m/s$ and the minimum resolvable velocity is equal to $0.15m/s$ (Adrian (1997)).

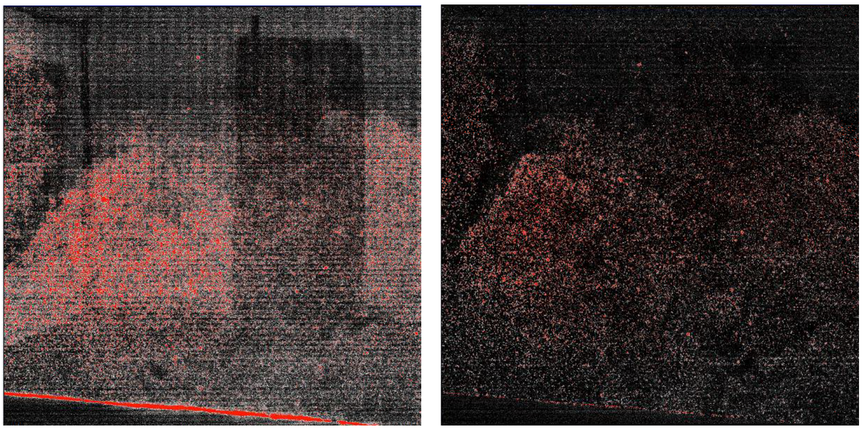

(a) (b)

Figure 5.10: (a) Raw image (b)Pre-processed image.

5.4.4 Post-processing

First the outliers were filtered out by using the universal outlier detection filter (Westerweel and Scarano (2005)), followed by a linear interpolation between empty space to fill them up. Next the empty edges of the measurement region were cut-off. Finally, in order to reduce the extent of the noise fluctuations, a spatial smoothing is performed by using a Gaussian Smoothing operator with a 3×3 pixel kernel. A vector field before and after post-processing is shown in figure 5.11.

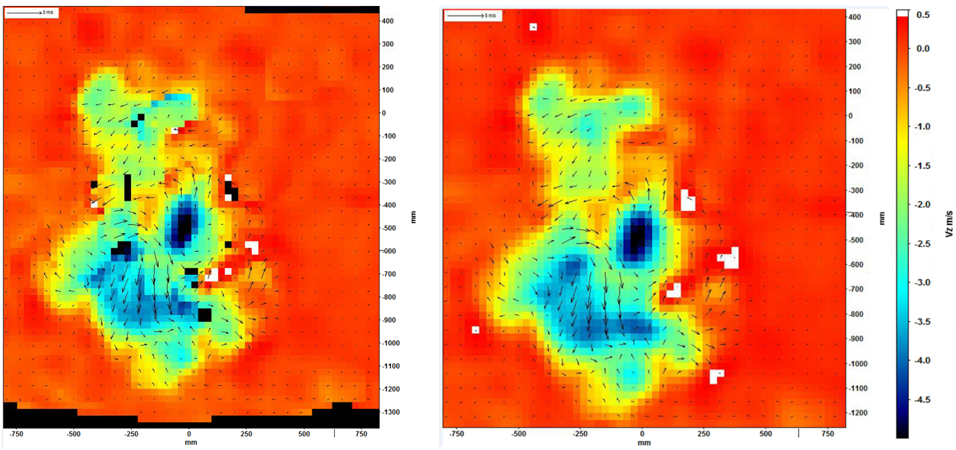

(a) (b)

Figure 5.11: (a) Vector field before post-processing (b)Vector field after post-processing.

Chapter 6

Results Scaled Ring of Fire

In the following chapter the results of the scaled experiment are discussed and compared to literature. The flow topology of both the instantaneous and time-averaged flow fields are examined in section 6.1. In section 6.2 the drag values are computed from both cases and compared to each other and literature. In order to neglect the contribution of the pressure to the drag force, all drag calculations are performed from $Z/D = 5$ onwards.

6.1 Flow Kinematics

6.1.1 Instantaneous flow field

Six consecutive instantaneous velocity fields in the XY-plane are shown in figure 6.1. The time is made non-dimensional with respect to the velocity of the sphere and its diameter:

$$t^{\star} = \frac{tU_{\infty}}{D} \tag{6.1}$$

where D is the diameter of the sphere and U_{∞} is the velocity of the sphere. $t^{\star} = 0$ corresponds to the moment that the back of the sphere just leaves the measurement volume. The translation in space between each time step in figure 6.1 corresponds to one sphere diameter in negative z-direction. Figure 6.1 presents the streamwise velocity in z-direction in the wake of the sphere. Close to the sphere, in the near wake, a velocity peak is observed. The further the sphere moves in z-direction, the smaller the velocity deficit in the measurement region becomes. This flow regime is in agreement with the characteristics of the mean flow in the wake of sphere that was found by Jang and Lee (2008) and by Constantinescu and Squires (2003). The negative streamwise velocity that is observed below the sphere ($X/D \sim 0, Y/D < -1$)

can be ascribed to the aerodynamic strut that is used to support the sphere.
Figure 6.2 shows the instantaneous streamwise velocity in the YZ-plane. In order to construct this velocity field, a Galilean transformation is applied to the data because the frame of reference was not yet consistent with the moving object. Once this is done, the instantaneous velocity fields of different time increments are combined to one elongated velocity field in streamwise direction. The same flow characteristics that are observed in figure 6.1, namely high peak velocities in the near wake of the sphere and a negative streamwise velocity below the sphere, are again visible in the YZ-plane. A closer look at this instantaneous velocity fields shows us a non-dimensional maximum reverse flow velocity of about $-0.6m/s$ at $Z/D = 0.6$. This is in consistency with the results presented by Terra et. al. Terra et al. (2017).

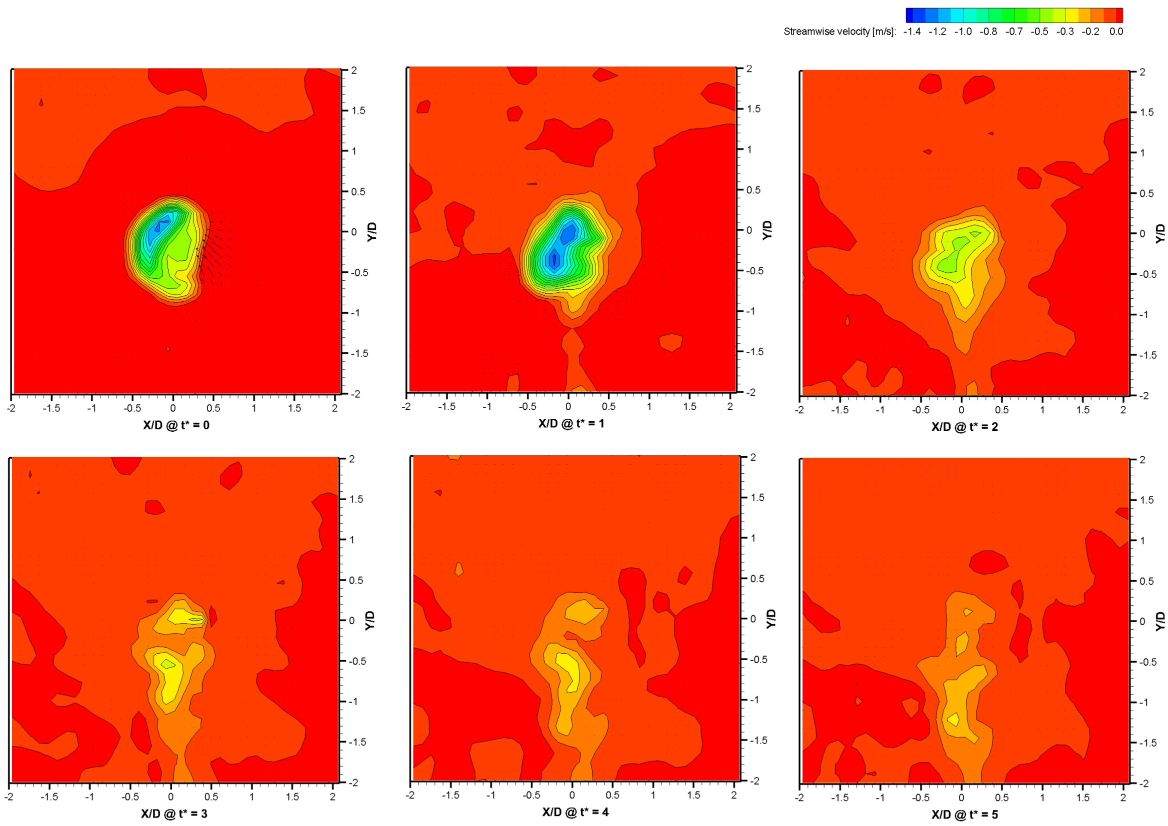

Figure 6.1: Instantaneous streamwise velocity u in the XY-plane at six time instances, $t^\star = 0$, $t^\star = 1$, $t^\star = 2$, $t^\star = 3$, $t^\star = 4$, $t^\star = 5$ for a sphere velocity of 1.332 m/s.

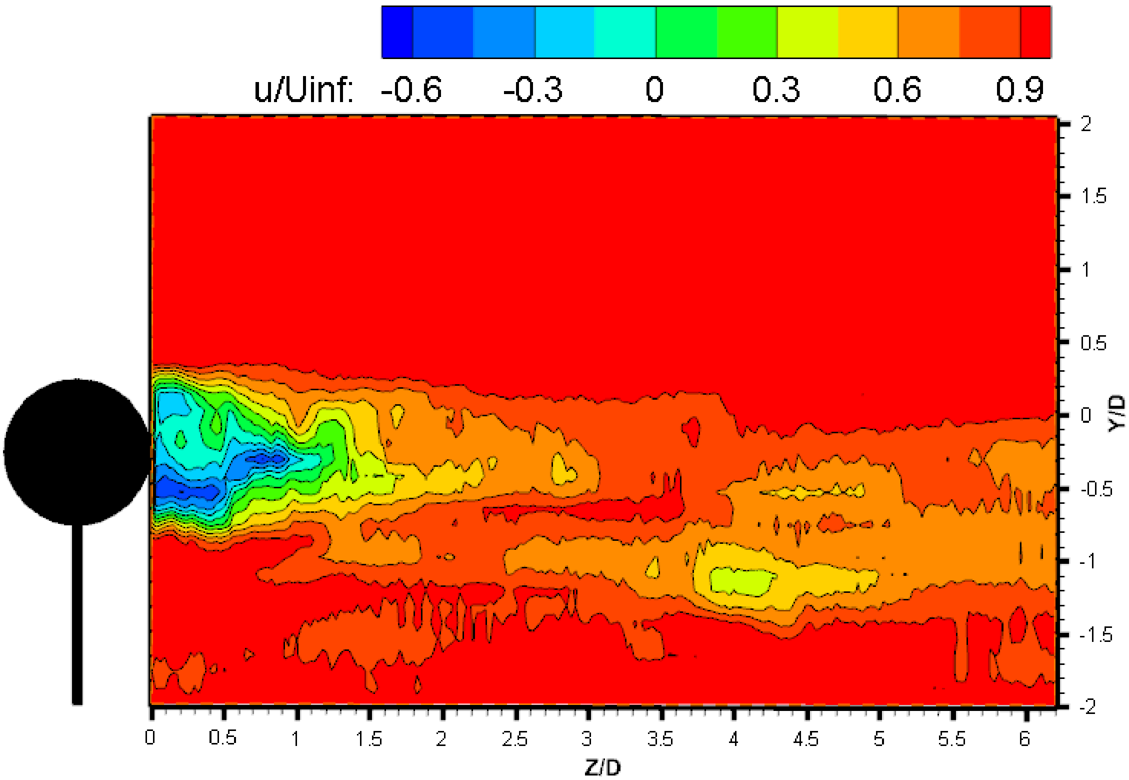

Figure 6.2: Non-dimensional instantaneous streamwise velocity in the YZ-plane at X/D=0 for a sphere velocity of 1.465 m/s.

6.1.2 Time-averaged flow field

In this next section the time averaged velocity and fluctuating velocity per nominal model velocity are presented. In section 3.2, equation 3.14 also makes use of the pressure fields to determine loads from time-averaged data. However, Terra et al. (2017) showed that from five diameters in the wake onwards, the pressure term becomes very small and can be neglected. For this reason the drag force results that are presented in section 6.2 are calculated only from five diameters and beyond. Time-average pressure fields are thus not used in this thesis and will not be further presented.
The time-average data is presented in the same reference frame, using the same non-dimensional variables as are used for presenting the instantaneous velocity fields. Figure 6.3 shows the streamwise velocity distributions in the middle XY-plane for the five tested velocities at $Z/D = 5$. Table 5.1 gives the number of instantaneous velocity fields used to produce the time-averaged velocity fields in figure 6.3, defines the average velocity per test case and gives the spread of this velocity data in terms of one standard deviation. The velocity field is rather axis-symmetric, which is to be expected for the flow past a sphere. The circular shape of the wake is altered only at the bottom of the measurement domain due to the presence of the supporting strut.

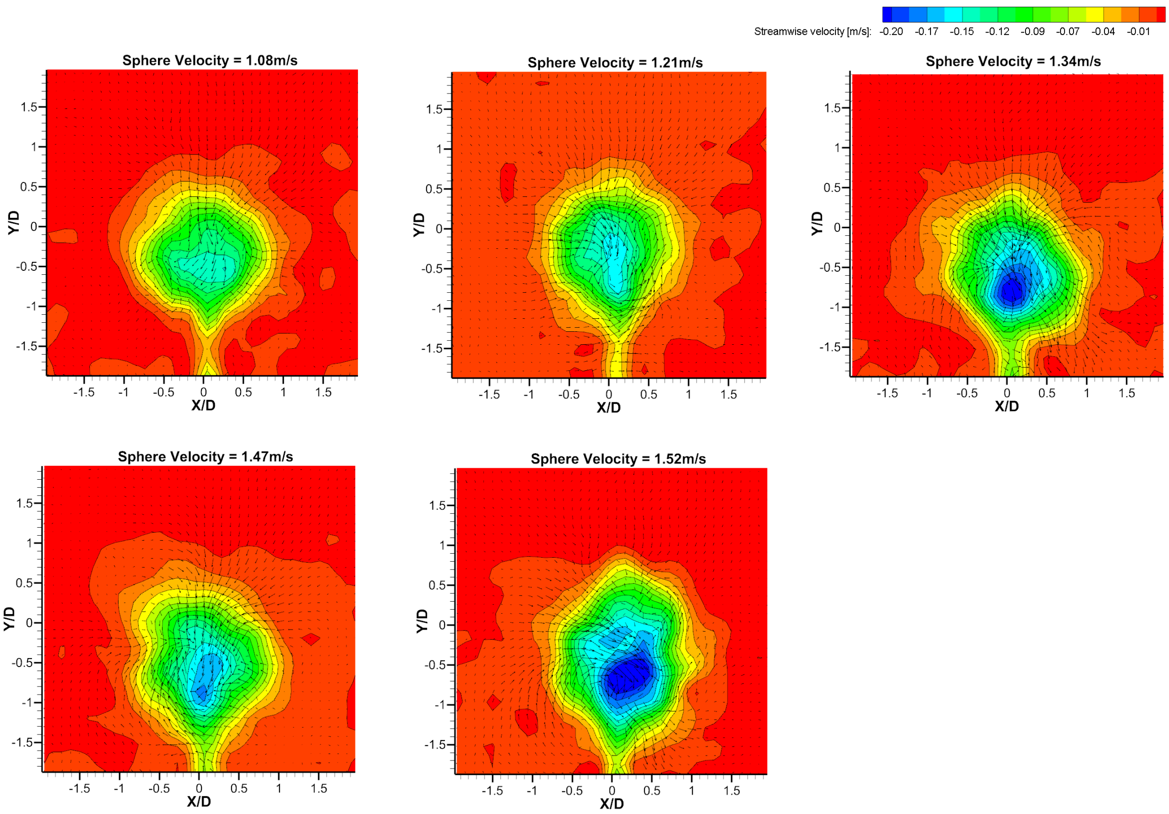

Figure 6.3: Time-average streamwise velocity in the XY-plane at $Z/D = 5$ for the five tested sphere velocities

6.2 Flow Dynamics

The time-average aerodynamic drag coefficient, as mentioned in section 3.2, can be computed from the time-averaged velocity field or from the instantaneous velocity fields. As is found by Terra et al. (2017), the pressure term in the right hand side of equation 3.14 and equation 3.11 can be neglected from $Z/D = 5$ onwards. The drag coefficient is computed from instantaneous as well as time-averaged velocity fields at $Z/D = 5$ for the five sets of velocities presented in table 5.1. A comparison between both is given in figure 6.4 and table 6.1.

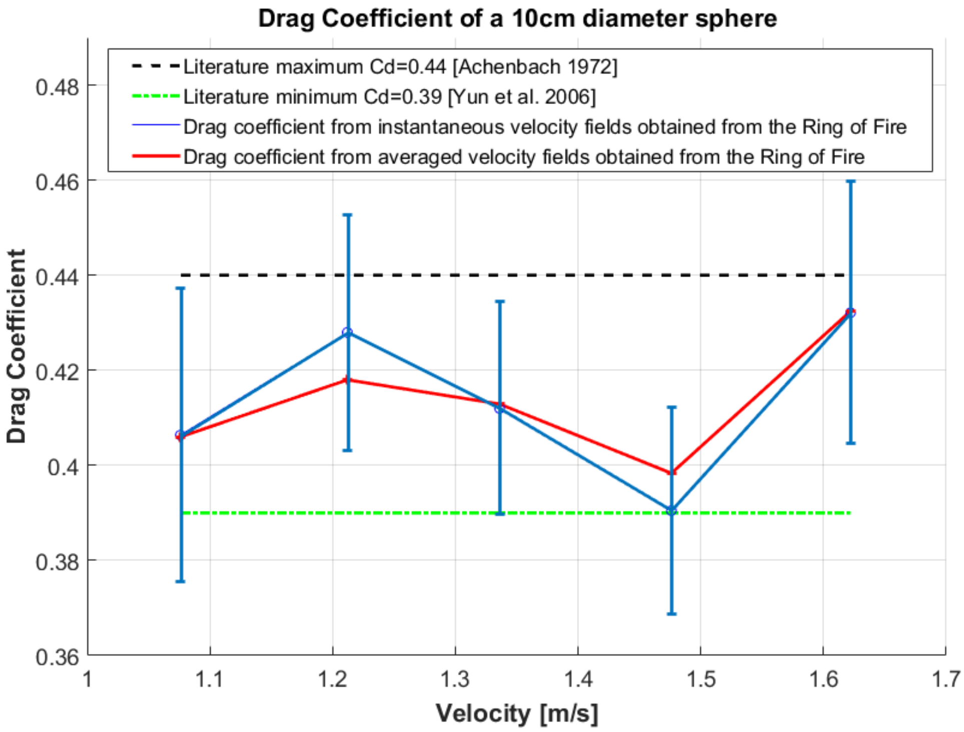

Figure 6.4: Experimental averaged drag coefficient of the sphere from ±60 samples versus velocity.

The drag coefficient obtained from the Ring of Fire is plotted in figure 6.4 together with the upper and lower limit values as found in literature. The lower drag coefficient equals 0.39 and is found by Yun et al. (2006), the upper drag coefficient equals 0.44 and is found by Achenbach (1972). The Reynolds numbers in both cases were respectively 10,000 and 20,000. It is observed that the results from both instantaneous and time-averaged velocity fields fall nicely inside this domain. Next to that, the difference between them never reaches more than two percent. The exact values and their difference are presented in table 6.1.

Table 6.1: Experimental averaged drag coefficient per velocity for both methods and their difference

Average velocity [m/s]	Cd from time-averaged velocity field	Cd from instantaneous velocity fields [Uncertainty]	Difference in Cd
1.076	0.4060	0.4064 [0.0309]	0.0004
1.212	0.4180	0.4224 [0.0236]	0.0044
1.336	0.4129	0.4120 [0.0224]	0.0009
1.476	0.3983	0.3905 [0.0218]	0.0078
1.622	0.4324	0.4321 [0.0276]	0.0003

It is concluded that both methods for drag computations are valid to use since the difference between both is only 2%. Further drag values presented in this thesis will be obtained from the instantaneous velocity fields, since this simplifies the processing procedure and it allows to determine the uncertainty on the average drag value. These uncertainties are shown in figure 6.4 and table 6.1. The uncertainty on the mean value is calculated by using equation 6.2.

$$U_{\overline{Cd}} = \frac{2 \cdot \sigma_{Cd}}{\sqrt{N}} \tag{6.2}$$

where $U_{\overline{Cd}}$ is the uncertainty on the mean value, σ_{Cd} is the standard deviation and N is the number of samples.
Re-writing this equation lets us determine the number of samples needed for convergence till a certain uncertainty is reached. Per velocity set the standard deviation for 60 samples is known and assuming that this will remain constant when increasing the number of samples, the required number of samples for convergence can be calculated. This is done per velocity set and the results are presented in table 6.2.

Table 6.2: Number of samples needed per velocity for convergence.

Average velocity [m/s]	Number of samples used	Averaged Cd	2 Standard Deviations	Number of samples for a uncertainty ≤ 2%
1.076	60	0.4064	0.2393	867
1.212	58	0.4224	0.1797	452
1.336	54	0.4120	0.1628	391
1.476	60	0.3905	0.1690	469
1.622	60	0.4321	0.2135	611

During the experimental campaign only 60 measurement per velocity are acquired. The amount of samples can be increased by "over-sampling" the time-resolved measurement. This means that multiple uncorrelated instantaneous velocity fields in the wake can be taken from one measurement. Over-sampling in this way is possible since the drag is expected to be independent of the distance of the measurement plane behind the sphere. The question then arises when the velocity fields are uncorrelated. To determine this, the autocorrelation coefficient is calculated. Details on this can be found in appendix A. Following the analysis in appendix A the amount of samples is increased from 60 till 180. This is not even close to the required amount, but already the uncertainty is dropped significantly for the different velocity sets (see table 6.3). Unsurprisingly, if the average drag coefficient is plotted against the number of samples it is observed that 180 samples is not enough for convergence. Figure 6.5 shows this by presenting the drag coefficient versus number of samples for the velocity set equal to $1.212 m/s$.

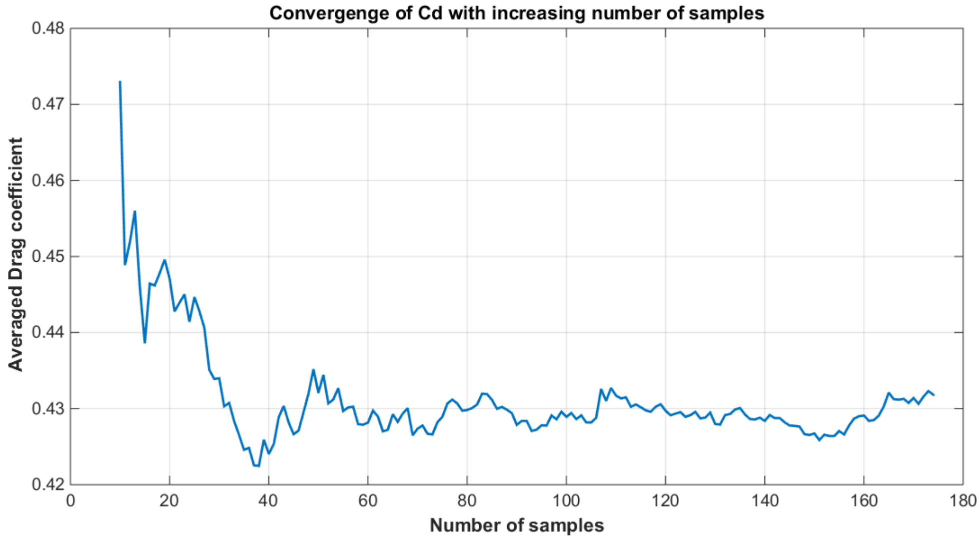

Figure 6.5: Convergence of the drag coefficient with increasing number of samples ($\overline{V}$ = $1.212[m/s]$).

Table 6.3: Uncertainty quantification

Velocity $[m/s]$	Uncertainty 60 samples [%]	Uncertainty 180 samples [%]
1.076	7.60	3.9
1.212	5.6	3.4
1.336	5.4	3.2
1.476	5.5	2.8
1.622	6.4	3.5

Figures 6.6 and 6.7 show the final results obtained from 180 uncorrelated samples in the wake for every velocity. The red dashed line in figure 6.6 shows the results when corrected for the blockage effect. The blockage correction lowered the drag coefficient by 3.15%. From table 5.1 it was found that for the range of Reynolds numbers in this experiment a more or less constant drag coefficient is expected. This constant trend is more or less observed in figure 6.6, with an outlier in velocity set 1.5.

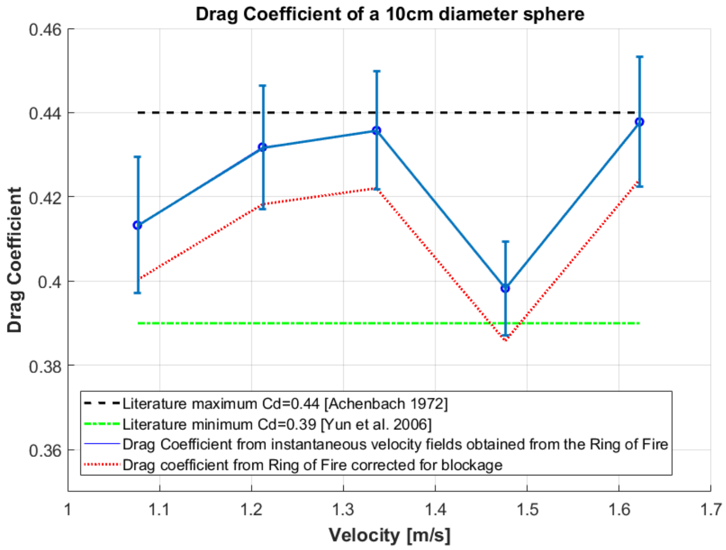

Figure 6.6: Final Cd values obtained from 180 uncorrelated samples.

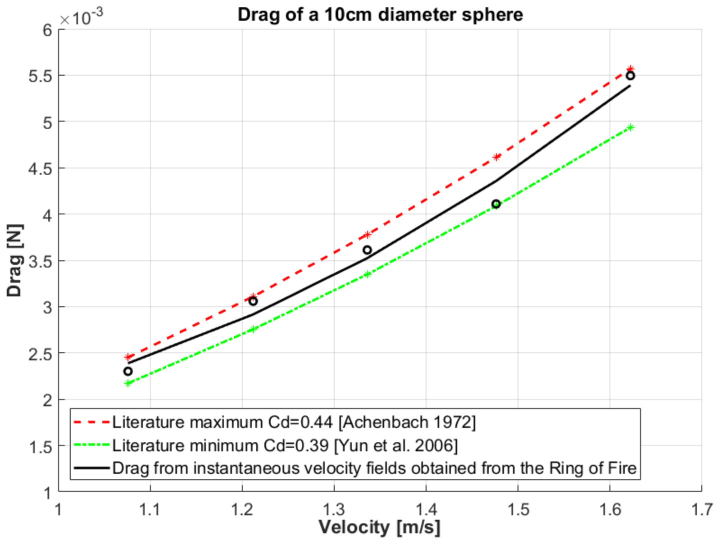

Figure 6.7: Final Drag from 180 uncorrelated samples.

The experimental time-averaged drag for the different velocities is plotted in figure 6.7. It is known that the Drag $\propto U^2$ and so a quadratic relation is expected. With exception of again velocity set $1.5m/s$, this trend is clearly visible. The fact that, compared to the other results, velocity set $1.5m/s$ has lower drag values can have multiple reasons. The measurements were conducted over the time span of a few days, and so it is possible that the measurement conditions changed between days.
The estimation of the drag coefficient at five different velocities is seen to fall within the range of reported values in literature. Furthermore all of these values are estimated with an

accuracy of about 5%. In comparison to the work of Terra et al. (2017), the drag coefficient is computed only at a few locations far downstream the wake (five, six and seven sphere diameters) without taking the pressure field into consideration. Finally it should be mentioned that for these measurements the contribution of the supporting strut was not subtracted from total contribution.

Chapter 7

Results full-scale Ring of Fire

This chapter presents the results obtained from the Ring of Fire measurements. As shown in figures 7.1 and 7.2, by combining individual images over time, applying the data reduction techniques described in chapter 4 and averaging over multiple runs, a time-averaged velocity field and vorticity field is obtained. The aim of this section is to, firstly, validate the flow-fields of the cyclist in time-trial position by comparing them to literature, more specific with the measurements of Shah (2017), Crouch et al. (2014) and Crouch et al. (2016b). Before comparing the results to literature however, the flow-field will be discussed in detail. Next, the drag forces for the time trial position are evaluated from the three-dimensional velocity fields. The drag forces that are obtained are then compared to balance measurements. Finally the flow-fields and drag values of the cyclist in up-right position will be analysed and compared to the time-trial position.

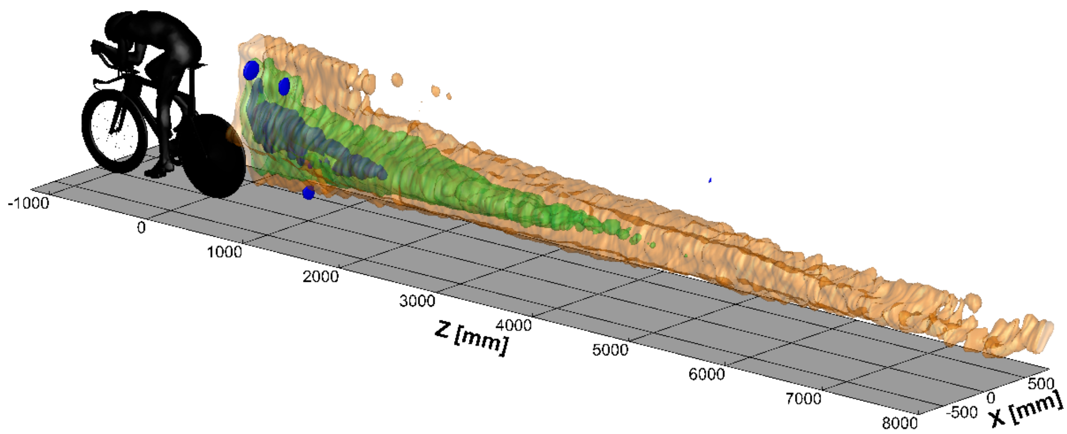

Figure 7.1: Time-average spatial development of non-dimensional streamwise velocity in the wake of the cyclist. Iso-surfaces correspond to w/W_∞ = 0.55 (blue), w/W_∞ = 0.7 (green) and w/W_∞ = 0.85 (orange).

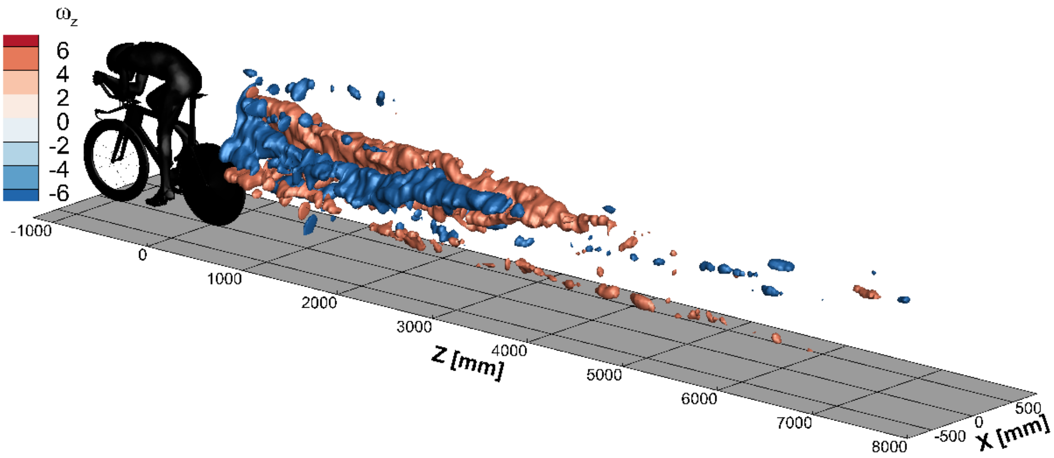

Figure 7.2: Time-average spatial development of streamwise vortex sructures in the wake of the cyclist. Iso-surfaces correspond to $\omega_z = -6s^{-1}$ and $\omega_z = 6s^{-1}$

7.1 Flow Kinematics

This first part discusses the time-averaged flow field in the wake of the cyclist in time-trial position. The three-dimensional flow-fields and development of vortical structures obtained from PIV at $8m/s$ are presented and discussed here. The streamwise velocity fields are presented in a frame of reference moving with the cyclist. This means that for $w/W_\infty = 0$ the flow velocity equals the cyclist velocity and for $w/W_\infty = 1$ the air is still.

7.1.1 Near wake

Figure 7.3 presents the results found in the upper half (above the back wheel) of the near wake at a plane 300mm from the back of the saddle. Figures 7.3(a) and 7.3(b) show respectively the streamwise and in-plane velocity components. The peak streamwise velocity is observed from the saddle height till the lower back and their is a clear distinction between the wake of the cyclist and the surrounding 'still' air. The in-plane velocity components show a significant downwash behind the curved back of the cyclist. Furthermore figures 7.3(b), 7.3(c) and 7.3(d) show the presence of the inner thigh vortices. Both the downwash and the inner thigh vortices were also found by Shah (2017) and Crouch et al. (2014).

7.1.2 Streamwise Velocity fields

Figure 7.4 shows non-dimensional, phase-locked time-averaged streamwise velocity fields in the XY-plane at nine different locations in the wake. Each plane in figure 7.4 corresponds not only to a different location but also to a different crank angle. Location and crank angle for each of the planes can be found in the caption of figure 7.4. Ten instantaneous velocity fields, selected from twenty passages of the cyclist, are used to estimate the statistical average. The selection was made in such a manner that the leg position of the athlete is equal in every run. It is observed that the measured velocities have a strong dependency on the distance of the measurement plane in the wake. The peak velocity in the plane taken closest to the cyclist (Z=400mm) is roughly 55% of the velocity of the cyclist, where in the furthest plane in figure 7.4 (Z=3400mm) the peak velocity has dropped to only 30% of the velocity of the cyclist. Next to this it is also seen that close to the cyclist the wake is rather narrow, more or less following the shape of the cyclist, whereas further downstream the wake clearly broadens in the lower half. The highest velocity peaks are observed in the region between the cassette assembly (Y=275mm) and the saddle height (Y=1050mm), so behind the lower half of the cyclist.

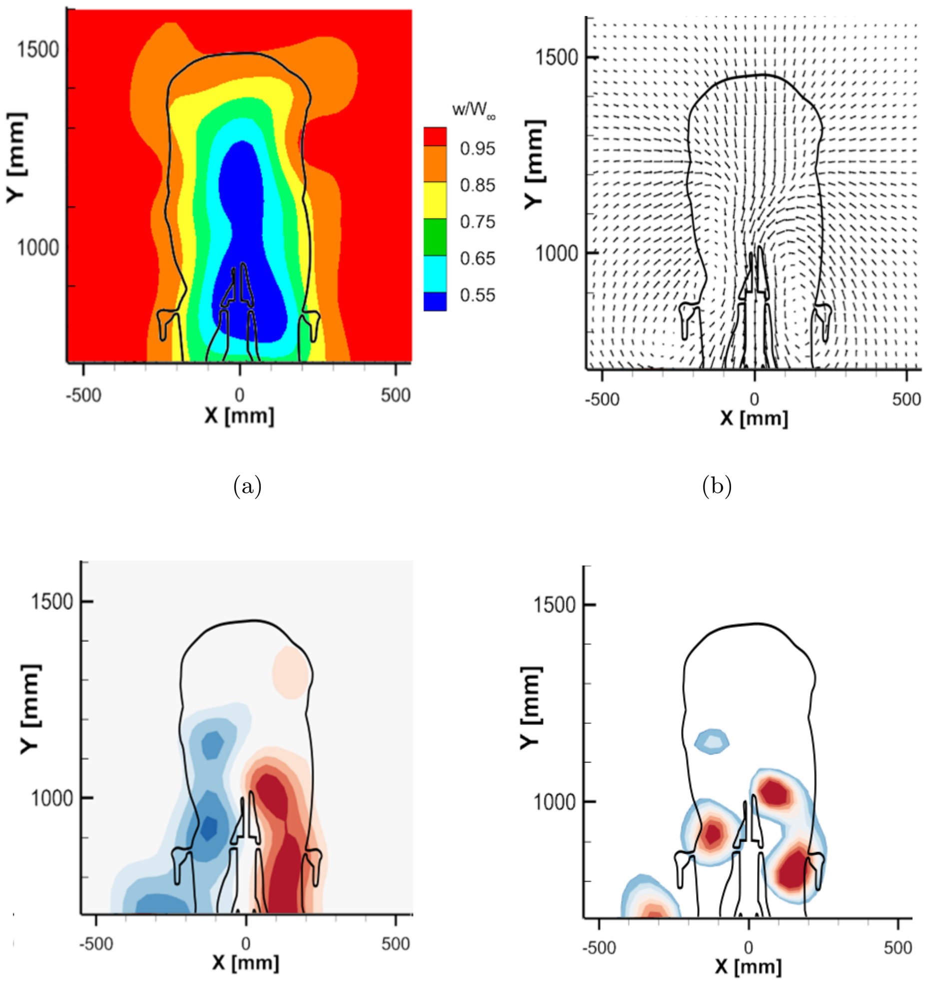

(a) (b)

(c) (d)

Figure 7.3: XY-plane at 300mm in the near wake of the cyclist at a crank angle of 130° presenting (a) Non-dimensional streamwise velocity (b) In-plane velocities (c) Vorticity field (d) Q-criterion

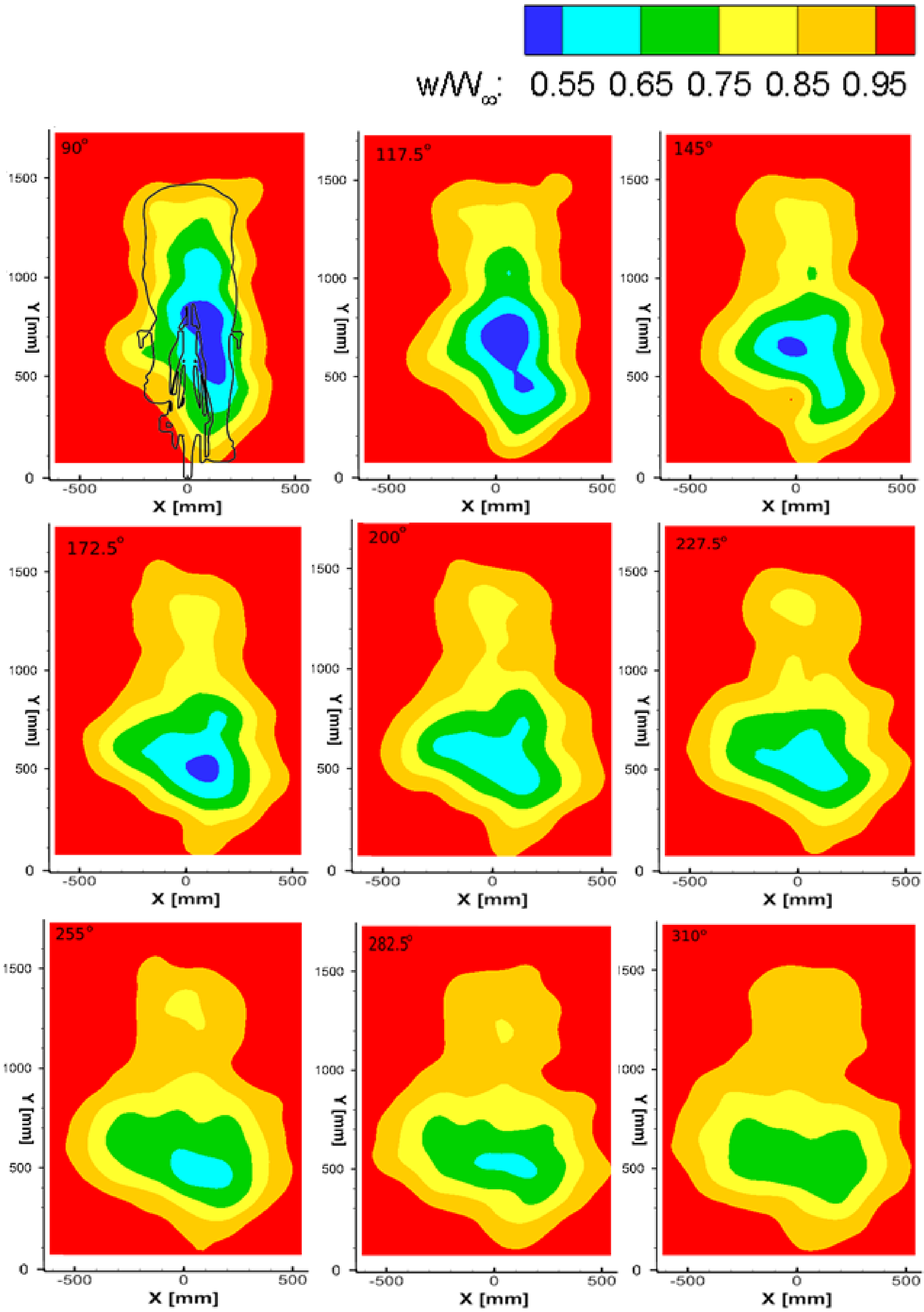

Figure 7.4: Phase-locked time-averaged, non-dimensionalized streamwise velocity in the XY-plane at multiple distances, Z = [400,775,1150,1525,1900,2275,2650,3025,3400][mm] (TLBR).

Figure 7.5 presents the streamwise velocity distribution in multiple XZ-planes and figure 7.6 presents the streamwise velocity distribution in multiple YZ-planes. The observations made in figure 7.4 are confirmed in figures 7.5 and 7.6. It is seen again that the top part of the wake is smaller then the bottom half and next to that it is confirmed that the highest peak velocities are in the center YZ-plane close to the cyclist from Y=275mm tot Y=1050mm. Next to this figures 7.5 and 7.6 also show that the wake starts off axis symmetric around the Z-axis but as it moves further downstream it starts moving to the side of the measurement region and starts diverging due to the asymmetric leg position. Eventually the wake becomes too wide to be still fully captured inside the measurement area.

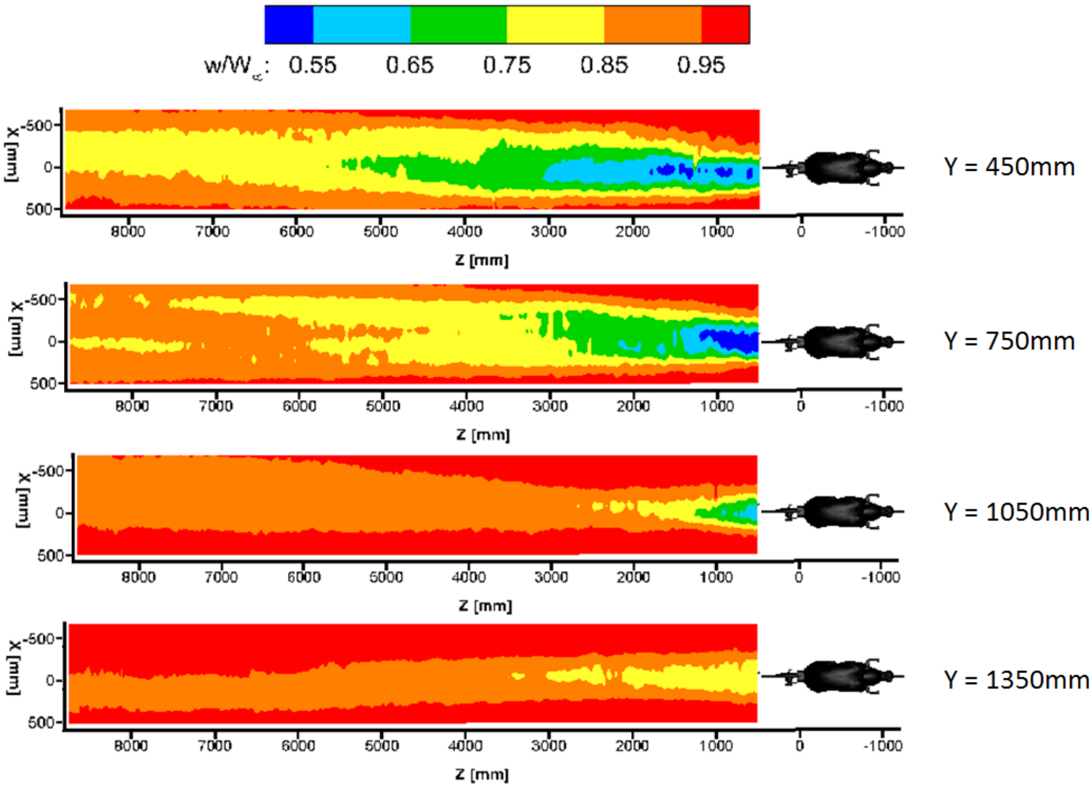

Figure 7.5: Time-averaged streamwise velocity in the wake of the cyclist at different XZ-planes at Y = [450,750,1050,1350][mm].

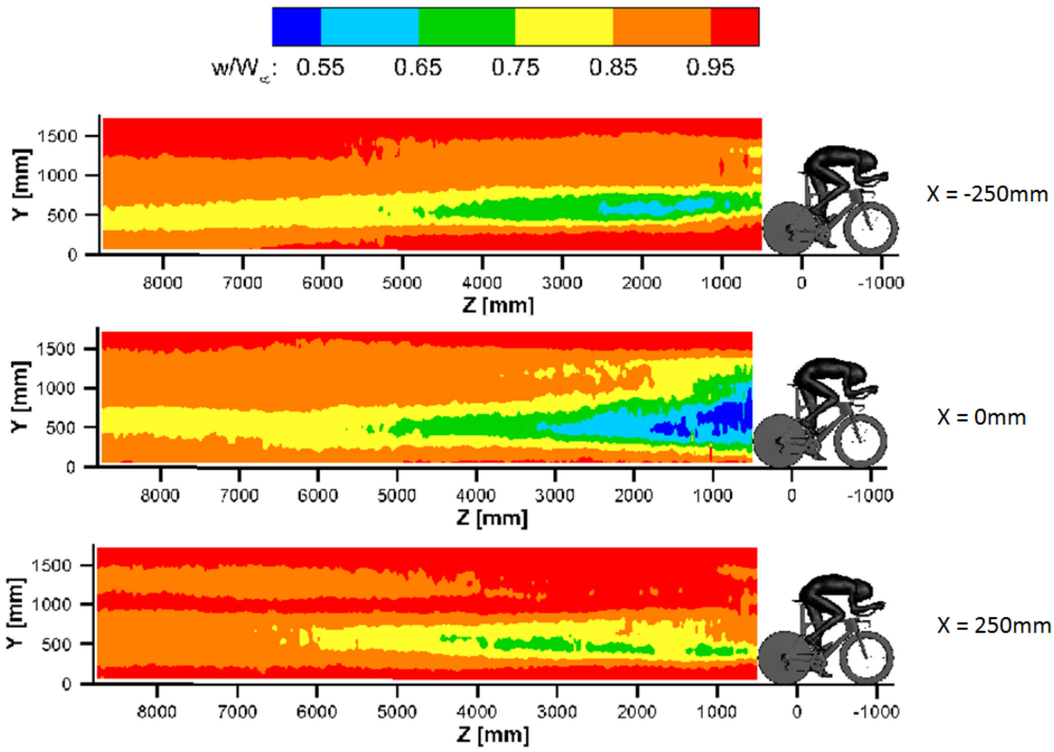

Figure 7.6: Time-averaged streamwise velocity in the wake of the cyclist at different YZ-planes at X = [-250,0,250][mm].

7.1.3 Vorticity field

The streamwise vorticity (ω_z) at multiple XY-planes in the wake of the cyclist is presented in figure 7.7. Some clear counter-rotating vortex pairs are identified close to the cyclist, see plane one in figure 7.7. The biggest one is originating from the inner thighs and consists of a large counter-clockwise rotating (blue) vortex and a large clockwise rotating (red) vortex at a height of roughly Y=1000mm. Vortices originating near the inner thighs were also observed by Crouch et al. (2014) and Shah (2017). Another smaller vortex pair is observed at Y=450mm, this pair emanates from the right foot that is in downward position at that time. Other vortices that might originate on the upper body may either merge or annihilate with the vortices originating on the lower body.

Figure 7.8 presents the time-averaged streamwise vorticity distribution in multiple XZ-planes. The two big vortical structures originating from the inner thighs are clearly visible. As the cyclist moves further away from the measurement plane, the vortices moving away from each other and become smaller in magnitude until they are dissipated.

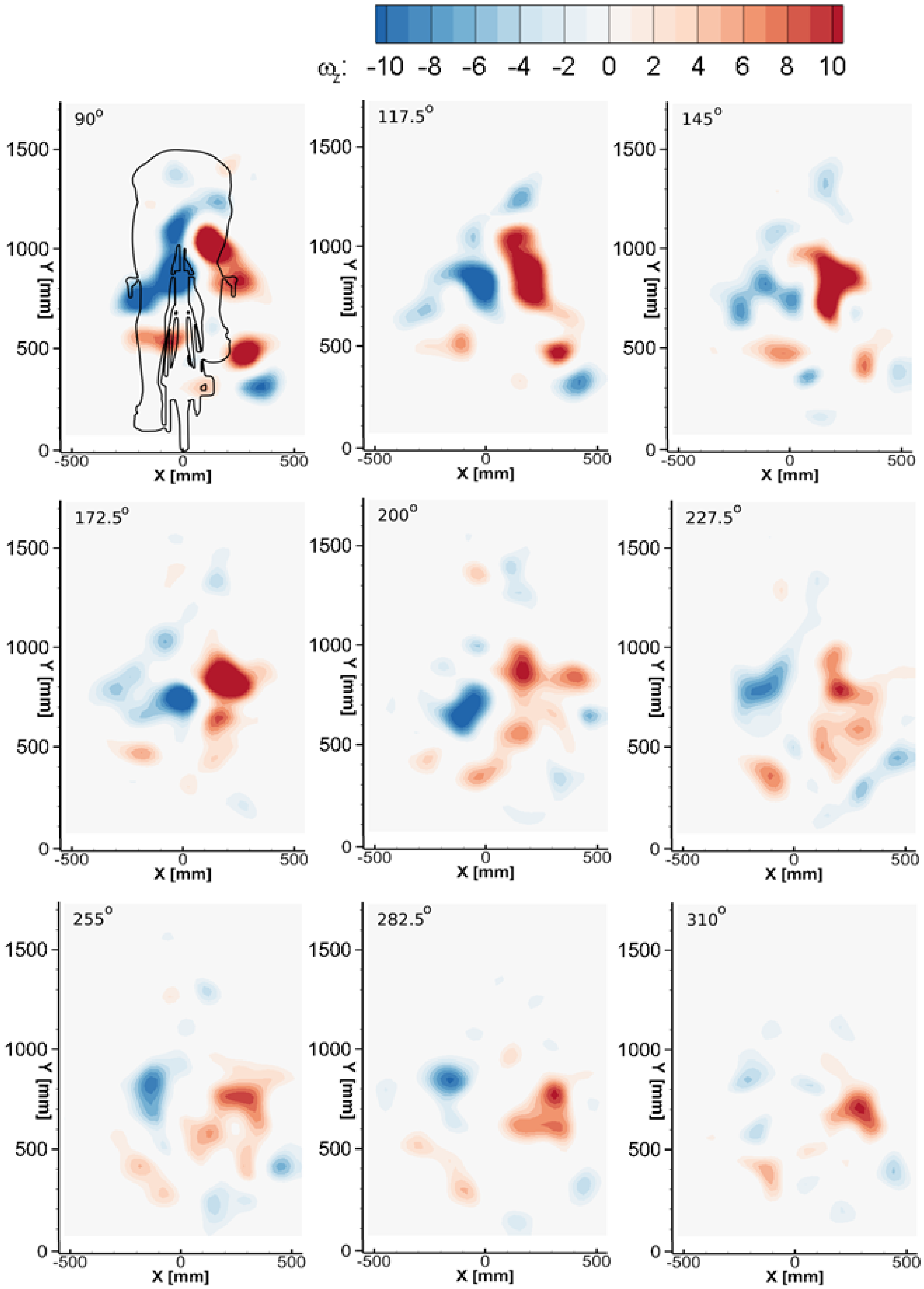

Figure 7.7: Phase-locked time-averaged streamwise vorticity ($\omega_z[s^{-1}]$) at different XY-planes at Z = [400,775,1150,1525,1900,2275,2650,3025,3400][mm] (TLBR).

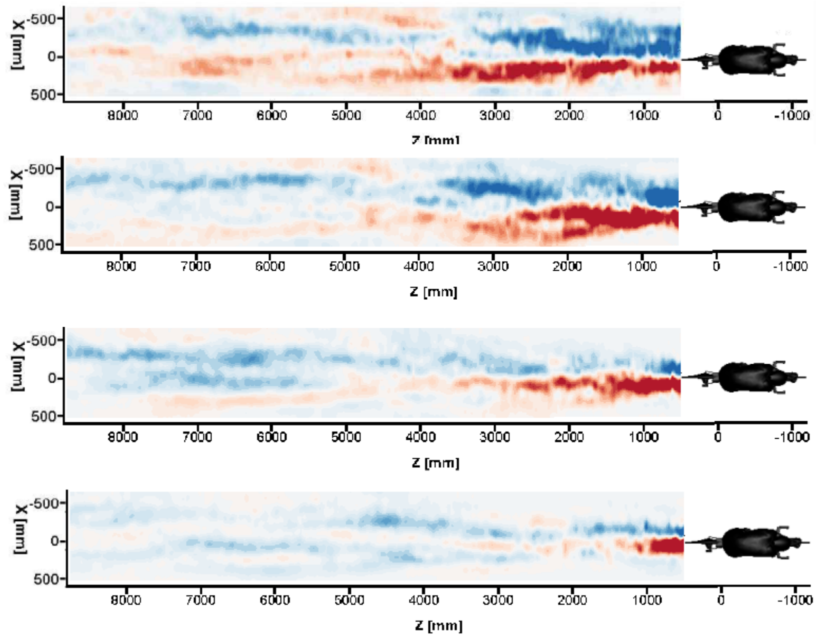

Figure 7.8: Time-averaged streamwise vorticty in the wake of the cyclist at different XZ-planes at Y = [750,850,950,1050][mm].

7.1.4 Comparison to literature

In order to validate the flow field and results obtained by the Ring of Fire, the studies performed by Shah (2017), Terra et al. (2016), Crouch et al. (2014) and Crouch et al. (2016a) are used for comparison. These studies were performed on a static model and to make a valid comparison, phase-locking is applied to the dynamic results obtained by the Ring of Fire. The results from the Ring of Fire presented below are time-averaged, phase-locked results at a plane 800mm behind the rear-most point on the saddle. The results corresponds to a crank angle of 90°. Firstly, the streamwise velocity fields are compared to the results found by (Shah, 2017). It has to be mentioned that the results from Shah (2017) were obtained at a freestream velocity of $14m/s$ with a crank angle of 270°. Next a comparison of the in plane velocity field is given. Thirdly, the large-scale structures in the flow are compared by means of the location and signs of the streamwise vortices. It has to be mentioned that in the study of Shah (2017) and Terra et al. (2016) the right leg is raised and in the case of Crouch et al. (2014), Crouch et al. (2016a) and the current study the left leg is raised.
Figure 7.9 shows a comparison in the averaged streamwise velocity fields between the current study (left) and the study by Shah (2017) (right).

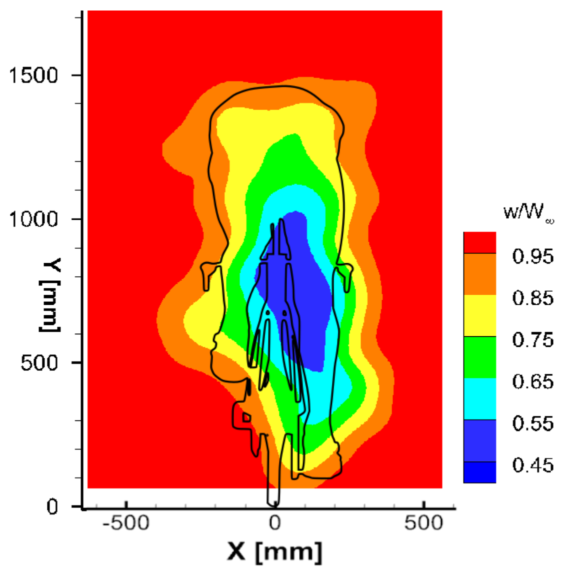

(a)

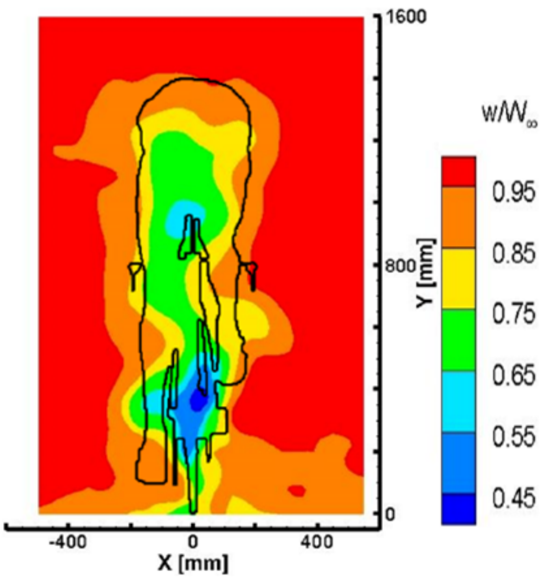

(b)

Figure 7.9: (a) Non-dimensionalized streamwise velocity (w/W_∞) obtained from current study ($Re = 3.17 \times 10^5$). (b) Non-dimensionalized streamwise velocity (w/W_∞) obtained from experiments of Shah (2017) ($Re = 5.74 \times 10^5$).

The streamwise velocity fields in figure 7.9 show some clear similarities, such as the peak deficit in the wake, which is 45% of the freestream velocity in both cases. However, the location of this peak velocity is not the same and the area of the peak velocity (and by extension the whole wake area) is larger in the current study. The Reynolds number, which is only half in the current study, may explain this difference. When the Reynolds number is larger, the boundary layer transition on the surface of the cyclist moves to the front which likely leads to a delayed separation on certain parts of the cyclist (e.g. legs) which causes the momentum deficit to be lower and the wake to contract. Next to the same peak velocity, the velocity fields also show similar large-scale structures, for example, a clear bulge is visible near the raised leg in both velocity fields. Figure 7.10 shows the contour of $w/W_\infty = 0.9$ for the current study (figure 7.10(a)) and for different velocities in the study of Shah (2017) (figure 7.10(b)). Like mentioned before, the wake structures are very similar, due to the difference in Reynolds number however, the wake structure of the current study is a bit wider. A key observation in figure 7.10 is that the contour of the wake of the current study does not interact with the floor at all, whereas in the study of Shah (2017) the wake has a big interaction with the floor of the windtunnel. The reason for this is that in the real world, and in the current study, the cyclist is moving and the air and road are fixed, in the study of Shah (2017) a fixed-floor windtunnel pushes wind across a cyclist and floor that are not moving. This causes a boundary layer to develop and interact with the wake of the cyclist.

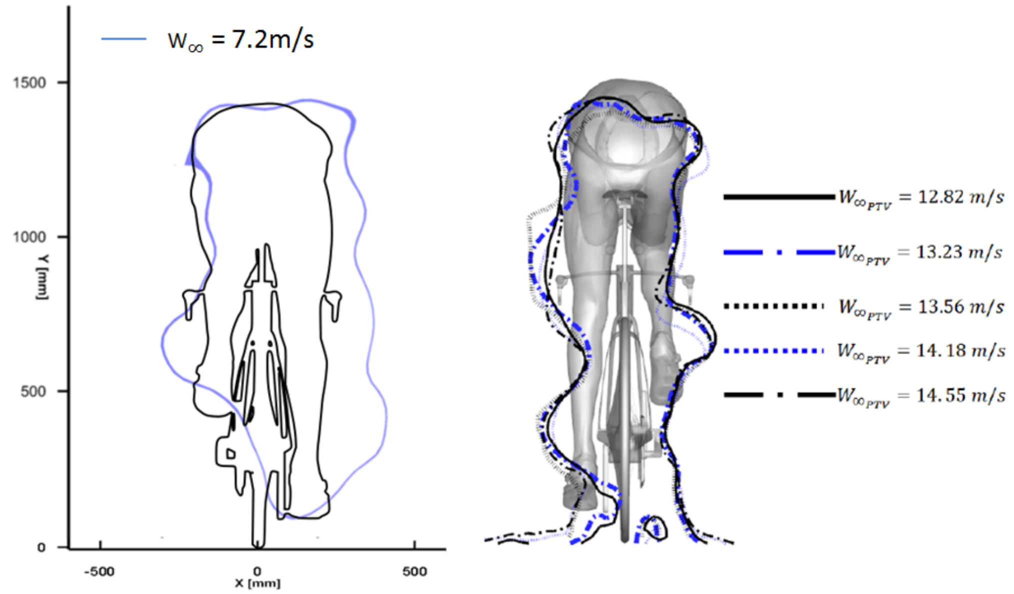

(a) (b)

Figure 7.10: (a) Contours of $w/W_\infty = 0.9$ for a velocity of the cyclist of $8m/s$ obtained from the current study ($Re = 3.17 \times 10^5$). (b) Contours of $w/W_\infty = 0.9$ for a range of incoming velocities obtained from experiments of Shah (2017) ($Re = 5.74 \times 10^5$).

Figure 7.11 presents the in-plane velocity components for both the current study and the study of Shah (2017). The overall flow structures are comparable to those found by Shah (2017), however they are much clearer visible in the study of Shah (2017). The latter can be attributed to the higher Reynolds number and the larger statistical ensemble compared to the current study. However, what stands out immediately, is the presence of the inner thigh vortex below the location of the hips and the absence of the upper hip vortex pair, both of them were observed by Crouch et al. (2014) in the near wake. At the location of the planes in figure 7.11 (Z=800mm) however, the later is probably not perceptible any more due to decay by cross-diffusive annihilation (Crouch et al. (2014)). The location of the downwash, that arises from the curved back of the cyclist, observed in figure 7.11(a) is in line with observations made by Shah (2017) (figure 7.11(b)) and Crouch et al. (2014). Other flow characterisitics that can be observed in 7.11(a) and that are in agreement with Shah (2017) and Crouch et al. (2014) are, among others, vortical structures near the feet and flow entrainment into the low-pressure wake.

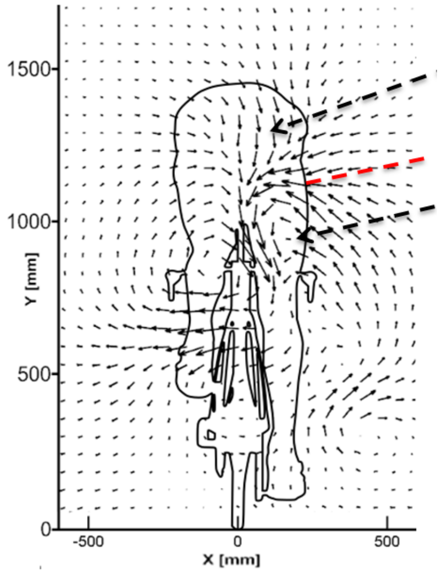

(a)

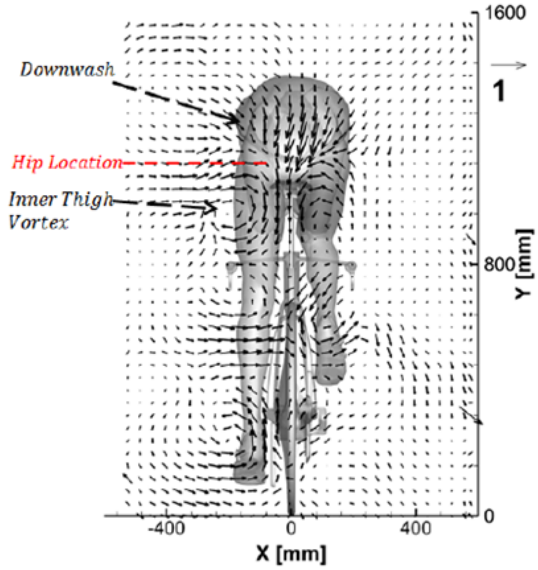

(b)

Figure 7.11: (a) In-plane velocity vectors obtained from the current study ($Re = 3.17 \times 10^5$). (b) In-plane velocity vectors obtained from the study of Shah (2017) ($Re = 5.74 \times 10^5$).

Figure 7.12 shows a comparison of the vorticity field at a plane 800mm behind the most-rear point of the saddle found in the current study (figure 7.12(a)) and found by Shah (2017) (figure 7.12(b)). The magnitude of the vorticity depends on the velocity and grid size of the measurement and so only a qualitatively comparison (sign and location) of the vorticity fields can be made. Earlier studies by Crouch et al. (2014), Terra et al. (2016) and Shah (2017) reported on the presence of upper and lower hip vortices, inner thigh vortices and vortices from the feet. In figure 7.12(a) both inner thigh vortices as well as two vortices originating from the right foot are visible, the vortices from the left foot are less clear. The location of primary streamwise vortices in figure 7.12(a) has a lower position in the wake where the leg is raised, and a higher one where the leg is extended. The above mentioned observations concerning the sign and location of the streamwise vortices are in agreement with the findings by Crouch et al. (2014) and Shah (2017).

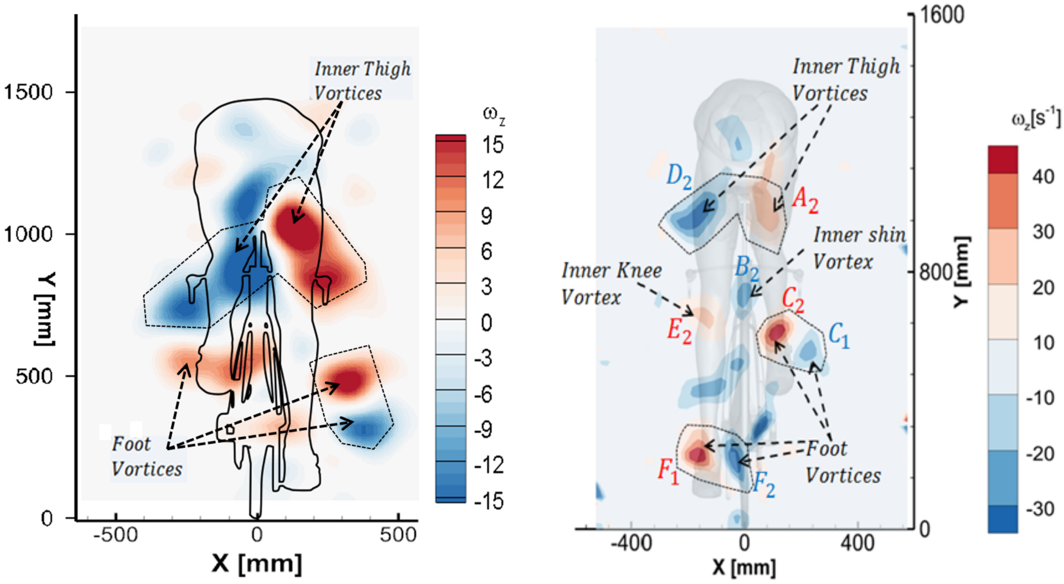

(a) (b)

Figure 7.12: (a) Streamwise vorticity (ω_z) obtained from the current study ($Re = 3.17 \times 10^5$). (b) Streamwise vorticity (ω_z) obtained from the study of Shah (2017) ($Re = 5.74 \times 10^5$).

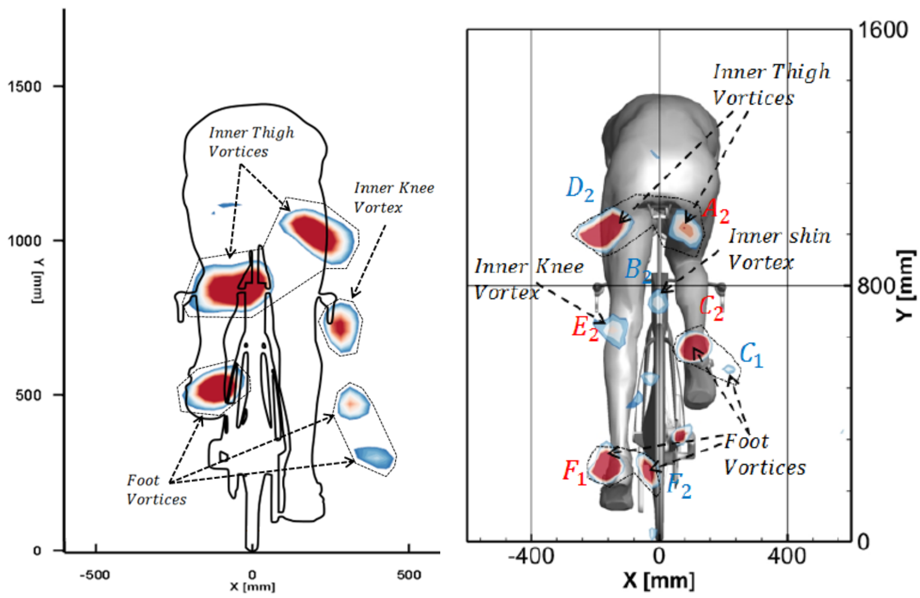

(a) (b)

Figure 7.13: (a) Q obtained from the current study ($Re = 3.17 \times 10^5$). (b) Q obtained from the study of Shah (2017) ($Re = 5.74 \times 10^5$).

Furthermore, the hip vortices found by Crouch et al. (2014) are not seen in the current study. The reason for this can be the different angle of the upper body with respect to the flow direction, in the case of Crouch et al. (2014) the model was positioned slightly upright which causes the hip vortices to arise from the lower portion of the back. In the current study as well as that of Shah (2017) and Terra et al. (2016), the cyclist/model has a flatter position on the bike which causes the magnitude of these hip vortices to decrease. Instead of the hip vortices, Shah (2017) observed a strong downwash and the non-zero vorticity near the back arch (figure 7.12(b)). Both are also found in the current study as can be seen in figures 7.3(b) and 7.12(a).
As was mentioned in chapter 4, plotting vorticity shows all non-zero vorticity and thus also velocity gradients that are only due to shearing motions. For this reason the Q-criterion is used for the identification of true vortices ($Q > 0$). Figure 7.13 confirms the presence of the inner thigh vortices and foot vortices. Next to that, the inner knee vortex that was observed by Shah (2017) (figure 7.12(b)), also became visible in figure 7.13(a) and it is confirmed that the downwash from the upper part of the back is caused by shearing motions in that region.

7.2 Flow Dynamics

This section presents the results for the drag force of the cyclist in time trial position. The drag force is computed from the instantaneous velocity fields by using equation 3.13 and neglecting the pressure term since it is negligibly small (Shah (2017)).

7.2.1 Variations in drag over time for individual measurements

The drag has been found to vary with the location in the wake. The variation within an individual run as well as between a few runs, is shown in figure 7.14. Note that the drag forces for each individual run is computed with respect to the measured velocity of the cyclist associated to that run and that they are already corrected for the freestream.

The drag force and drag area in figure 7.14 are calculated without taking pressure into account (Terra et al. (2016)), which explains the increase in drag in the near wake. After three meters the values more or less stabilizes to a 'constant value', meaning that the drag force and drag area fluctuate around a mean value with fluctuations not bigger than $0.025[m^2]$ in case of the drag area. It is observed that for a few runs (pointed out by arrow in figure 7.14), starting from around five meter in the wake, the drag force and drag area are decreasing in magnitude. Taking a closer look at the velocity fields of those particular runs tells us that the wake translates to the left or right over time. After a while part of the wake move outside the measurement plane and thus a big part of the momentum deficit in the wake will not be measured, causing the calculated drag to drop. Examples of a 'good' run and a 'bad' run are shown in figure 7.15, where instantaneous velocity fields at 6.5 meter in the wake of respectively run20 (fig. 7.15(a)) and run30 (fig. 7.15(a)) are presented. For the above mentioned reasons only the drag values from three meters till five meters in the wake are seen fit to be used for analysis and comparison.

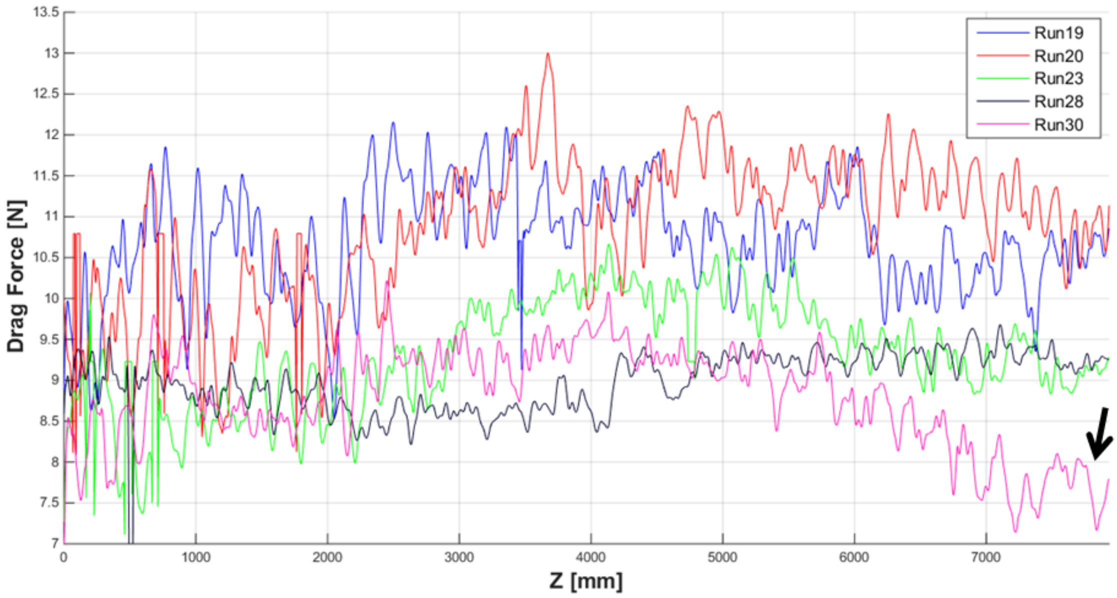

(a)

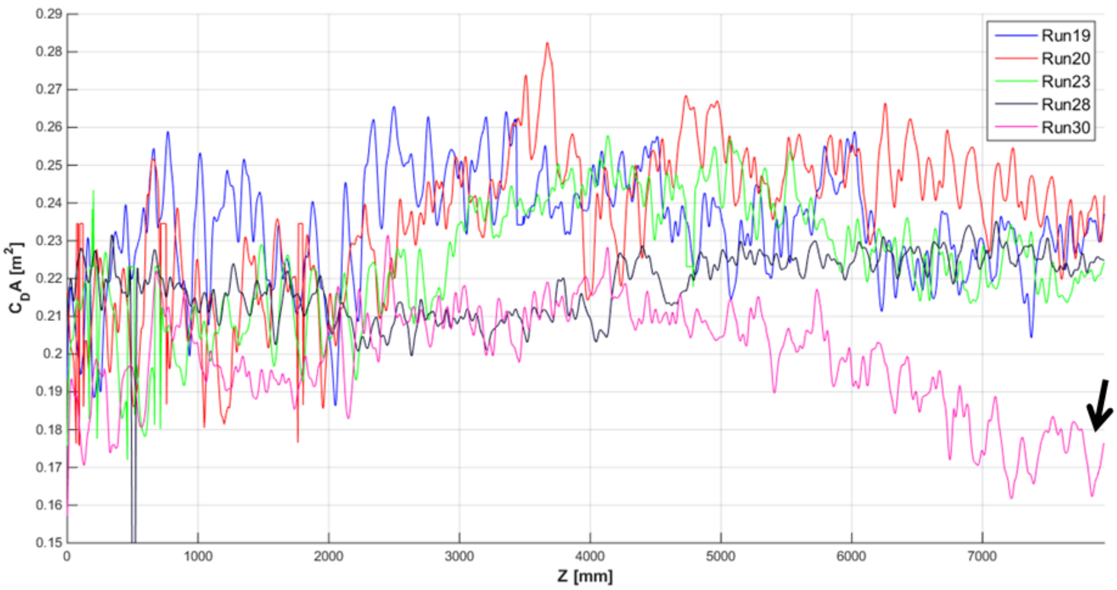

(b)

Figure 7.14: (a) Variations in instantaneous drag force for different individual runs. (b) Variations in instantaneous drag area C_DA for different individual runs.

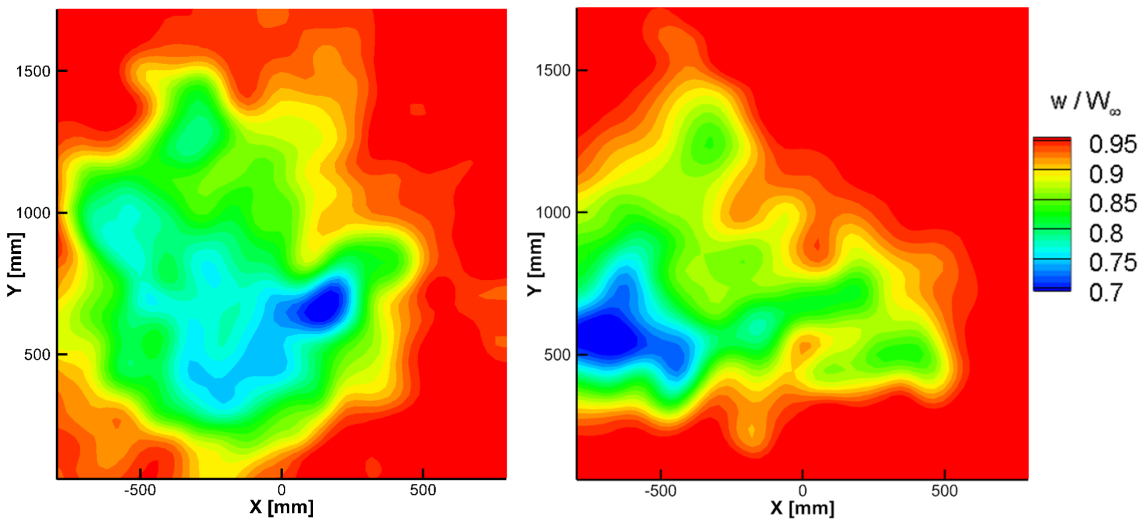

(a) (b)

Figure 7.15: Instantaneous streamwise velocity fields at 6.5meter in the wake of respectively (a) Run 20. (b) Run 30.

7.2.2 Comparison to balance measurements

Figure 7.16 presents the time-averaged drag area versus location in the wake for the cyclist in time trial position and compares those values to the results from balance measurements. The time averaged drag area shows only small variations, no larger than 5% and an uncertainty of only ±5%, keeping in mind that only ten individual runs were used, this result is very promising. However, the difference between the drag area from balance measurements and from the PIV data is roughly thirty percent. This has two reasons, the first is that the drag computations from PIV are performed on an extracted area in the wake and some momentum deficit is lost in this operation with a lower drag force as a result ($\Delta C_D A \approx 0.01$). Next to that, the balance measurement results are expected to be higher than the Ring of Fire ones. Compared to windtunnel measurements, the wake of the cyclist in the Ring of Fire set-up does not interact with the ground, see figure 7.10. At a velocity of $13.5m/s$, Shah (2017) showed that in the windtunnel the first $15cm$, starting from the floor, contribute to the drag force by $5N(\Delta C_D A = \pm 0.05)$. In the current study the lower $15cm$ in the wake have a negligible contribution to the drag force and since Crouch et al. (2014) showed that the drag area ($C_D A$) for a cyclist is constant for a wide range of Reynolds numbers, the contribution of the lower $15cm$ to the $C_D A$ value found by Shah (2017) can be subtracted from the drag area found by the balance measurements performed for the current study. It is assumed that the correction for the ground interaction based on the results found by Shah (2017) is an underestimation because, as was mentioned earlier, the wake in the study of Shah (2017) is smaller and so the ground effects is expected to be smaller as well. Applying these corrections reduces the difference between balance and PIV to ten percent (green line in figure 7.16).

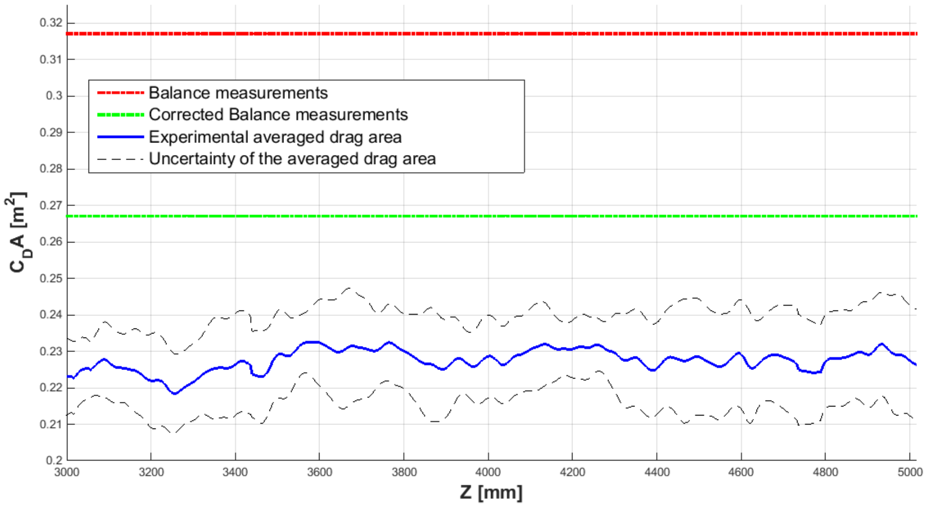

Figure 7.16: Time-averaged drag area of the cyclist in Time Trial position obtained from ten individual runs.

7.3 Analysis upright position

In order to show that the Ring of Fire set-up can measure differences in drag, this section analyses the results from a cyclist in upright position and compares it to the time trial position of the cyclist. All results presented in this section are obtained at a plane $800mm$ behind the cyclist, where the right leg of the cyclist is fully stretched. Previous studies such as the one of Zdravkovic et al. (1996) and Grappe et al. (2010) have shown that a clear difference in drag force is found when comparing both positions. The first part of this section will compare the flow field in the wake after which the drag forces will be compared.

Figure 7.17(a) shows the non-dimensionalized, time averaged streamwise velocity in the wake of the cyclist in upright position, which is found to be similar to the case where the cyclist was in time trial position (figure 7.9(a)). Both the peak velocities in the wake are found behind the lower half of the cyclist as well as it is seen that the area of momentum deficit is bigger behind the stretched leg compared to the raised leg. In order to compare the shapes of both wakes (time trial and upright position), the time-averaged contours of $w/W_\infty = 0.9$ are plotted in 7.17(b). As expected the wake of the cyclist in upright position is taller than the one of the cyclist in time trial position. Next to this, a big bulge is seen in the wake of the upright case at the height of the right hip/thigh, which is not present in the case of the time trial case. A possible explanation for this bulge is, due to the change in position of the cyclist, the flow starts to separate at the hip/thigh of the cyclist, causing a vortex to form. Figure 7.18 confirmes this theory by showing the presence of a strong vortex at the location of the bulge.

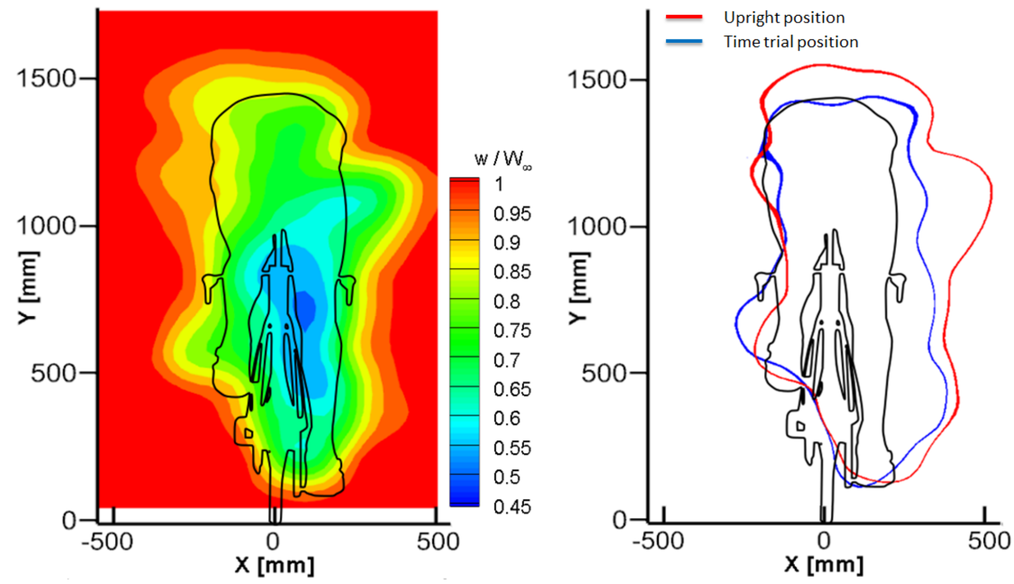

(a) (b)

Figure 7.17: (a) Time-averaged streamwise velocity at a plane 800mm behind the cyclist obtained from ten runs. (b) Time-averaged contours of $w/W_\infty = 0.9$ for both upright and time trial position at a velocity of the cyclist of $8m/s$.

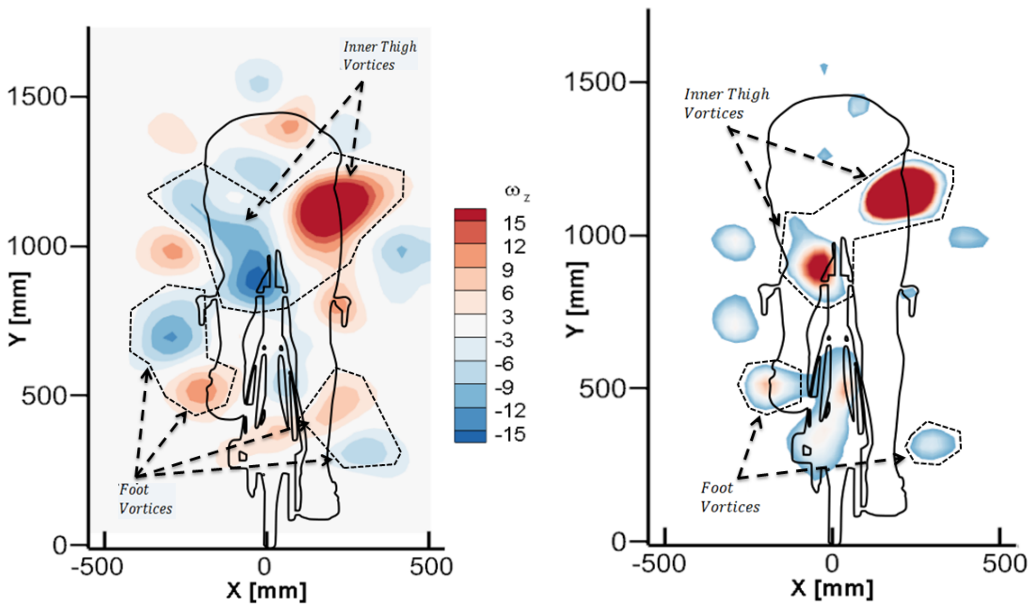

(a) (b)

Figure 7.18: (a) Time-averaged vorticity at a plane 800mm behind the cyclist obtained from ten runs. (b) Time-averaged Q-criterion at a plane 800mm behind the cyclist obtained from ten runs.

Figure 7.18 presents the streamwise vorticity (left) and Q-criterion (right) in the wake of the cyclist in upright position. Two inner thigh vortices as well as four foot vortices are observed. The location of the inner thigh streamwise vortex originating from the raised leg (lower and towards the center plane) as well as the location of the inner thigh streamwise vortex originating from the stretched leg (higher and further out) are in agreement with the results from the time trial position in the current study (figures 7.12(a) and 7.13(a)) as well as with the findings of Shah (2017) and Crouch et al. (2014). Furthermore there are some smaller vortices noticeable in figure 7.18, it is however not clear from the data if these are the secondary streamwise vortices that were observed by Crouch et al. (2014) or if this is noise.

Figure 7.19 presents the time-averaged drag area versus location in the wake for the cyclist in time trial position as well as in upright position. As expected the drag area in upright position is clearly higher, around twenty-five percent, and is almost constant, with only small variations not larger than 5% and an uncertainty of ±5%. In other studies from Grappe et al. (2010) and Defraeye et al. (2010), the drag area in upright position is found to be respectively 0.299 and 0.270. Next to that, Defraeye et al. (2010) also finds the difference between time trial position and upright position to be in the order of twenty-five-percent. It can thus be stated that the drag area for the cyclist in upright position obtained by the Ring of Fire set-up is in agreement with literature.

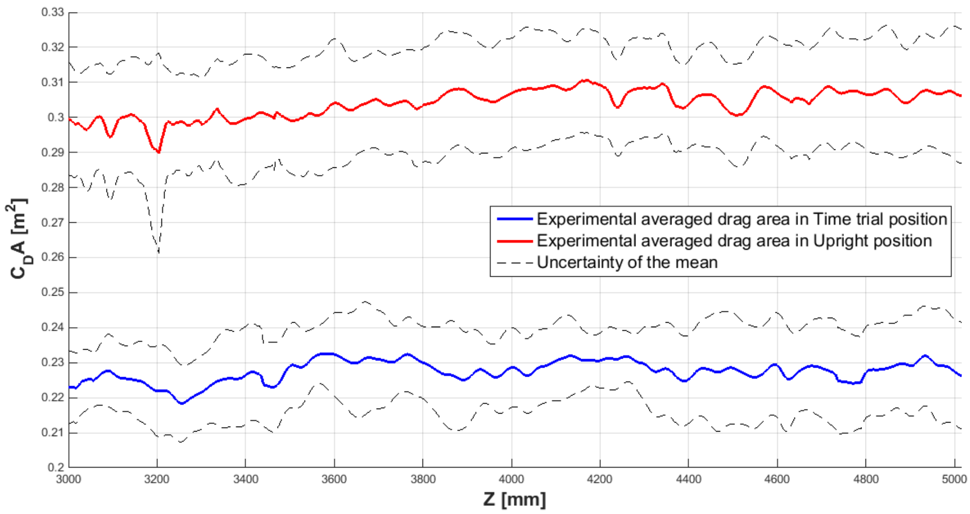

Figure 7.19: Time-averaged drag area of the cyclist in time trial position and upright position, both obtained from ten runs.

Chapter 8

Conclusion and Recommendations

This thesis presents a feasibility study of a novel aerodynamic measurement system that can be operated outside of a windtunnel. The proposed system makes use of the large-scale particle image velocimetry technique. The in-field measurements offer better representation of real world conditions because the cyclist is moving instead of the surrounding air, no supporting structures are necessary and there is no limitation in size, so no inaccuracies due to scaling and Reynolds number effects. The potential of the proposed system is investigated by means of an experimental study on a transiting cyclist at $8m/s$, visualizing the flow field in the wake of the cyclist and obtaining its drag from a control volume approach. Section 8.1 presents the conclusions that follow from the present work, which is followed by recommendations for future research and development in section 8.2.

8.1 Conclusions

Typically aerodynamic measurements in sports are conducted in a windtunnel or by numerical simulations on a steady model. The Ring of Fire system proposed in this thesis relies on in-field, large-scale PIV and conducts aerodynamic measurements during the athlete's motion, which allows for new measurements (accelerations and curved paths) compared to the steady state models in a wind tunnel. The use of HFSB as seeding for the PIV allows these large-scale measurements. From this the thesis objective is formulated as follows:

"Assess the feasibility of an on-site aerodynamic measurement system (Ring of Fire) based on large-scale PIV for full-scale applications in speed sports. Further, test the accuracy of the system by comparing the drag values obtained at multiple different velocities from a scaled test setup."

To fulfil the research objective, the accuracy and characteristics of the Ring of Fire system are to be examined experimentally. First a small-scaled Ring of Fire was build, studying the flow in the wake of a $10cm$ diameter sphere and its drag forces at five different velocities ranging from $U_{sphere} = 1.1m/s$ till $U_{sphere} = 1.6m/s$ by means of Tomographic PIV. The results, obtained from a sample size of 180 uncorrelated samples per velocity set, show a time-resolved wake structure that is similar to those observed in literature. The computed drag coefficients of the sphere for Reynolds numbers in the order of $\mathcal{O}(10^4)$ have an accuracy of 5% and are within the range as found in literature.

The potential of the proposed Ring of Fire system is tested on a full-scale, cycling athlete at $8.0m/s$ in time-trial position as well as in upright position. One second of time-resolved stereoscopic PIV data in the wake of the cyclist is acquired at 2kHz for twenty runs per position, which leads to a time-averaged flow field in the wake of the athlete of $25m^3$. Dividing the measurement area into interrogation windows of $113 \times 113m^2$ and applying cross-correlation between images yields in a structured dataset with a velocity vector every 28mm, a Dynamic Velocity Range (DVR) of 100:1 and a Dynamic Spatial Range (DSR) of 60:1 for the system.

The averaged large-scale wake structure, obtained from a set of ten passages of the athlete, shows great resemblance to wake measurements available from literature (Crouch et al. (2014); Terra et al. (2016); Shah (2017)). The peak momentum deficit is comparable to the ones reported earlier and behind the stretched leg the amount of momentum deficit is larger than behind the raised leg. Furthermore, the vortices originating from the hips and thighs as well as from the feet are observed, which is in agreement with literature. However a striking difference in the lower 15cm of the wake is observed when comparing the Ring of Fire to the previous mentioned studies. The latter make use of a fixed-floor windtunnel and supporting struts, causing a boundary layer to grow and start interacting with the wake of the athlete. The air in the Ring of Fire prior to the passage of the cyclist is standing still, not creating a boundary layer, and thus no interactions of the wake with the ground are seen, yielding a more accurate capturing of the wake. An observation made during processing the data is that in some cases the wake tends to translate to the left or the right and by doing so moving out of the measurement area.

Furthermore, the obtained data is used for drag force computation by applying a control volume approach. The individual drag values computed are highly fluctuating within a single run and in some cases, where the wake moves out of the measurement plane, the drag is estimated lower than it is in reality. The variation within the nominal values of the averaged drag area obtained by the Ring of Fire are seen to be less than 5%. The uncertainty on this mean value is around 5%. Without applying any corrections to the calculated drag area from balance measurements however, they are found to be 40% higher compared to the drag area found from the PIV data. After correcting for the wake ground interaction the difference is lowered till 10%. This can have multiple causes, but these are not further investigated in this thesis.

The results obtained from the large-scale experiment demonstrate the feasibility of the on-site aerodynamic measurement system (Ring of Fire) for a full-scale industrial application and thus the thesis objective is reached. The results from this study can be taken as a basis for potential improvements of the system in the future, which are identified in the next section.

8.2 Recommendations

The Ring of Fire is still in its infancy, which means that many aspects for further development can be thought of. This section lists some of these as recommendations for future work. The final goal of the Ring of Fire project is to develop a system that can perform on-site aerodynamic measurement of an athlete in his or her training environment and knowing the accuracy of the measurements. To do so, the data acquiring time need to be reduced significantly. In the experiment described in chapter5 one measurement took between five and ten minutes, if for example one intends to perform measurements on a cyclist on a velodrome it would be ideal if one measurement could be acquired every round ($\approx$ 1min). Two bottlenecks in the experiment are observed, firstly the time it takes to homogeneously fill the measurement area with tracer particles, secondly the selection and saving process of the required data.
It is believed that the time to seed the measurement area in a homogeneous way can be reduced by positioning the seeding nozzles in a more optimal way, in order to create a curtain of seeding particles in the measurement area.
In the current experiment it was a rather devious and time consuming work to select and save the data, instead of manually determining the speed of the cyclist and looking for the correct frames to save, one can think of an algorithm that automates the selection and saving of data based on the measured location and velocity of the athlete.

It is also recommended to further investigate and improve the accuracy of the system. A first step can be to investigate the effect of peak locking on the accuracy. Additionally, one could investigate the possibilities towards an adaptive-resolution algorithm that processes the data with respect to its location in the wake. The peak velocities in the wake tends to decay away from the athlete, this means that the optimal spatial resolution and acquisition frequency is different close to the athlete and far away.

To get a better understanding of the drag force computation and its accuracy, an in depth investigation of all components of the drag force (Momentum, pressure and Reynolds stresses) is recommended. This can give an idea if some terms, and in the end the drag force, are over or under estimated.

Other applications will bring along other possible recommendations for improvement, for example a bigger tent may be needed when testing multiple cyclists in a certain formation. The recommendations mentioned above however, are thought of to be applicable to a broad spectrum of applications.

Bibliography

Elmar Achenbach. Experiments on the flow past spheres at very high reynolds numbers. *Journal of Fluid Mechanics*, 54(3):565575, 1972.

R.J. Adrian. Dynamic ranges of velocity and spatial resolution of particle image velocimetry. *Measurement Science and Technology*, (8):1393–1398, july 1997.

R.J. Adrian and J. Westerweel. *Particle Image Velocimetry*. Cambridge University Press, 2011.

J. Anderson. *Fundamentals of Aerodynamics*. McGraw Hill, 2001.

M P Arroyo and C A Greated. Stereoscopic particle image velocimetry. *Measurement Science and Technology*, 2(12):1181, 1991.

N. Barry, D. Burton, J. Sheridan, and N.A.T. Brown. Flow interactions between two inline cyclists. *19 th Australian Fluid Mechanics Conference*, 2014.

Nathan Barry, David Burton, John Sheridan, Mark Thompson, and Nicholas A. T. Brown. Flow field interactions between two tandem cyclists. *Experiments in Fluids*, 57(12):181, Nov 2016.

G. Blois, J.L. Best, K.T. Christensen, V. Cichella, A. Donahue, N. Hovakimyan, A. Kennedy, and I. Pakrasi. Uav-based piv for quantifying water-flow processes in large-scale natural environments, jul 2016.

Johannes Bosbach, Matthias Khn, Markus Rtten, and Claus Wagner. Mixed convection in a full scale aircraft cabin mock-up. 6:1–9, 06 2006.

B. Celis and H.H. Ubbens. Design and construction of an open-circuit wind tunnel with specific measurement equipment for cycling. *Procedia Engineering*, (147):98 103, 2016.

V. Chabroux, M.N. Mba, P. Sainton, and D. Favier. Wake characteristics of time trial helmets using piv-3c technique. In *15th Int Symp on Applications of Laser Techniques to Fluid Mechanics*, jul 2010.

G.S. Constantinescu and K.D. Squires. Les and des investigations of turbulent flow over a sphere at re = 10,000. *Flow, Turbulence and Combustion*, 70(1):267–298, Jan 2003.

T.N. Crouch, D. Burton, M.C. Thompson, N.A.T. Brown, and J. Sheridan. Flow topology in the wake of a cyclist and its effect on aerodynamic drag. *JFM*, 748:5–35, 2014.

T.N. Crouch, D. Burton, M.C. Thompson, N.A.T. Brown, and J. Sheridan. A comparison of the wake structures of scale and full-scale pedalling cycling models. *Procedia Engineering*, (147):13–19, 2016a.

T.N. Crouch, D. Burton, M.C. Thompson, N.A.T. Brown, and J. Sheridan. Dynamic leg-motion and its effect on the aerodynamic performance of cyclists. *Journal of Fluids and Structures*, 65:121–137, 2016b.

T. Defraeye, B. Blocken, E. Koninckx, P. Hespel, and J. Carmeliet. Aerodynamic study of different cyclist positions: Cfd analysis and fullscale wind-tunnel tests. *Journal of Biomechanics*, 43(7):1262 – 1268, 2010.

G. E. Elsinga, F. Scarano, B. Wieneke, and B. W. van Oudheusden. Tomographic particle image velocimetry. *Experiments in Fluids*, 41(6):933–947, Dec 2006.

G.E. Elsinga. *Tomographic particle image velocimetry and its application to turbulent boundary layers*. PhD thesis, TU Delft, jun 2008.

Gerrit E. Elsinga, Bernhard Wieneke, Fulvio Scarano, and Andreas Schröder. *Tomographic 3D-PIV and Applications*, pages 103–125. Springer Berlin Heidelberg, 2008.

Giuseppe Gibertini and Donato Grassi. Cycling aerodynamics. pages 23–47, 2008.

H.J. Goett. Experimental investigation of the momentum method for determining profile drag. *NATIONAL ADVISORY COMMITTEE FOR AERONAUTICS*, (660), 1939.

F. Grappe, R. Candau, A Belli, and J.D. Rouillon. Aerodynamic drag in field cycling with special reference to the obree's position. *Ergonomics*, 40(12):1299–1311, 2010.

M. D. Griffith, T. Crouch, M. C. Thompson, D. Burton, and J. Sheridan. Elite cycling aerodynamics: Wind tunnel experiments and cfd, 2012.

R.K. Hanna. Can cfd make a performance difference in sport. *Engineering of Sport*, (4): 17–30, 2002.

J. Hart. Cser exhibition at the royal institution. https://www.slideshare.net/JohnHart21/cserroyalinstitutionexhibition, 2014.

A. Henning, H. Richard, T Kowalski, T. Gries, S. Huntgeburth, and S. Loose. Full-scale piv measurement on high-speed trains, jul 2016.

J. Hoekstra. Open jet facility brochure, tu delft. `http://www.lr.tudelft.nl/en/organisation/departments/aerodynamics-wind-energyflight-performance-and-propulsion/facilities/wind-tunnel-lab/open-jet-facility-hsl/`. Accessed: 2017-09-24.

Young Il Jang and Sang Joon Lee. Piv analysis of near-wake behind a sphere at a subcritical reynolds number. *Experiments in Fluids*, 44(6):905–914, Jun 2008.

Mattias Jönsson and Sigfried Loose. *Experimental Investigation of the Flow Field Underneath a Generic High-Speed Train and the Effects of Ground and Train Roughness*, pages 21–36. 2016.

C. Jux. Robotic volumetric particle tracking velocimetry by coaxial imaging and illumination. Master's thesis, TU Delft, jul 2017.

D.F. Kurtulus, F. Scarano, and L. David. Unsteady aerodynamic forces estimation on a square cylinder by tr-piv. *Experiments in Fluids*, (42):185196, 2007.

le Tour de France. Tour de france 2017 classifications after the stage 21, jul 2017. URL http://www.letour.fr/le-tour/2017/us/classifications.html.

C.M. Leong, Y. Moon, V. Wu, T. Wei, and S. Peters. Dpiv measurements of olympic skeleton athletes (fluid dynamics video). https://arxiv.org/abs/1010.2792, oct 2010.

K. P. Lynch and F. Scarano. An efficient and accurate approach to mte-mart for time-resolved tomographic piv. *Experiments in Fluids*, 56(3):66, Mar 2015.

Kyle Lynch. *ADVANCES IN TIME-RESOLVED TOMOGRAPHIC PARTICLE IMAGE VELOCIMETRY*. PhD thesis, TU Delft, dec 2015.

Francesco Mariani, Claudio Poggiani, Francesco Risi, and Lorenzo Scappaticci. Formula-sae racing car: Experimental and numerical analysis of the external aerodynamics. *Energy Procedia*, 81:1013 – 1029, 2015.

K. Matsuuchi, T. Miwa, T. Nomura, J. Sakakibara, H. Shintani, and B.E. Ungerechts. Unsteady flow field around a human hand and propulsive force in swimming. *Journal of Biomechanics*, 42(1):42 – 47, 2009.

W. Meile, W. Mller, and E. Reisenberger. Ski-jumping aerodynamics: Model-experiments and cfd-simulations. pages 183–216, 2008.

C.D. Meinhart, S.T. Wereley, and J.G. Santiago. A piv algorithm for estimating time-averaged velocity fields. *Journal of Fluids Engineering*, 122(2):285–289, 2000.

D. Michaelis, D.R. Neal, and B. Wieneke. Peak-locking reduction for particle image velocimetry. *Measurement Science and Technology*, 27(10), sep 2016.

N.J. Neeteson, S. Bhattacharya, D.E. Rival, D. Michaelis, D. Schanz, and A. Schrder. Pressure-field extraction from lagrangian flow measurements, 2015.

M. Raffel, C. Willert, S. Wereley, and J. Kompenhans. *Particle Image Velocimetry, a practical guide*. Springer Berlin Heidelberg, second edition, 2006.

D. Ragni, B.W. van Oudheusden, and F. Scarano. Non-intrusive aerodynamic loads analysis of an aircraft propeller blade. *Experiments in Fluids*, (51):361–371, 2011.

Lars Sætran and Luca Oggiano. Skin suit aerodynamics in speed skating. pages 93–105, 2008.

F. Scarano. Experimental aerodynamics. Delft University of Technology, 1 edition, 2013. Course reader, Flow Measurement Techniques (AE4-180)., 2013a.

F Scarano. Tomographic piv: principles and practice. *Measurement Science and Technology*, 24(1), 2013b.

F. Scarano, C. van Wijk, and L.L.M. Veldhuis. Traversing field of view and ar-piv for mid-field wake vortex investigation in a towing tank. *Experiments in Fluids*, (33):950–961, 2002.

F. Scarano, S. Ghaemi, G. Caridi, J. Bosbach, U. Dierksheide, and A. Sciacchitano. On the use of heliumfilled soap bubbles for largescale tomographic piv in wind tunnel experiments. *Experiments in Fluids*, 56(42), 2015.

Jan F. G. Schneiders, Giuseppe C. A. Caridi, Andrea Sciacchitano, and Fulvio Scarano. Large-scale volumetric pressure from tomographic ptv with hfsb tracers. *Experiments in Fluids*, 57(11):164, Oct 2016.

A. Sciacchitano, G.C.A. Caridi, and F Scarano. A quantitative flow visualization technique for on-site sport aerodynamics optimization. *Procedia Engineering*, (112):412–417, 2015.

M.S. Selig, R.W. Deters, and G.A. Williamson. Wind tunnel testing airfoils at low reynolds numbers. 49th AIAA Aerospace Science meeting, 2011.

Y. H. Shah. Drag analysis of full scale cyclist model using large-scale 4d-ptv. Master's thesis, TU Delft, July 2017.

H. Takagi, S. Shimada, T. Miwa, S. Kudo, R. Sanders, and K. Matsuuchi. Unsteady hydrodynamic forces acting on a hand and its flow field during sculling motion. *Human Movement Science*, oct 2014.

W. Terra, A. Sciacchitano, and F. Scarano. Evaluation of aerodynamic drag of a full-scale cyclist model by large-scale tomographic-piv, 2016.

W. Terra, A. Sciacchitano, and F. Scarano. Aerodynamic drag of transiting objects by large-scale tomographic-PIV. 18th International Symposium on the Application of Laser and Imaging Techniques to Fluid Mechanics, 2017.

G. Tescione, D. Ragni, C. He, C.J. Simo Ferreira, and G.J.W. van Bussel. Near wake flow analysis of a vertical axis wind turbine by stereoscopic particle image velocimetry. *Renewable Energy*, 70:47 – 61, 2014.

M. Toloui, S. Riley, J. Hon, K. Howard, L. P. Chamorro, M. Guala, and J. Tucker. Measurement of atmospheric boundary layer based on super-large-scale particle image velocimetry using natural snowfall. *Experiments in Fluids*, (55), may 2014.

R. Tsai. A versatile camera calibration technique for high-accuracy 3d machine vision metrology using off-the-shelf tv cameras and lenses. *IEEE Journal on Robotics and Automation*, 3(4):323–344, August 1987.

B. W. van Oudheusden, F. Scarano, E. W. M. Roosenboom, E. W. F. Casimiri, and L. J. Souverein. Evaluation of integral forces and pressure fields from planar velocimetry data for incompressible and compressible flows. *Experiments in Fluids*, (43):153162, 2007.

B.W. Van Oudheusden. Piv-based pressure measurement. *Measurement Science and Technology*, 24, 2013.

Jerry Westerweel and Fulvio Scarano. Universal outlier detection for piv data. *Experiments in Fluids*, 39(6):1096–1100, Dec 2005.

B. Wieneke. Stereo-piv using self-calibration on particle images. *Experiments in Fluids*, 39 (2):267–280, Aug 2005.

B. Wieneke. Volume self-calibration for 3d particle image velocimetry. *Experiments in Fluids*, 45(4):549–556, Oct 2008a.

B. Wieneke. Volume self-calibration for 3d particle image velocimetry. *Experiments in Fluids*, (45):549–556, jun 2008b.

A. Winkler and A. Pernpeintner. Improving the performance of a bobsleigh by aerodynamic optimization (p212). pages 329–338, 2008.

G. Yun, D. Kim, and H. Choi. Vortical structures behind a sphere at subcritical reynolds numbers. *Physics of Fluids*, 18(015102), 2006.

M.M. Zdravkovic, M.W. Ashcroft, S.J. Chisholm, and N Hicks. Effect of cyclists posture and vicinity of another cyclist on aerodynamic drag. *The Engineering of Sport*, pages 21–28, 1996.

Appendix A

Autocorrelation

Autocorrelation determines the similarity between samples as a function of the time difference between them. For the scaled Ring of Fire experiemt the autocorrelation coefficient of the streamwise velocity fluctuations at two windows of 9x9vectors in the wake of the sphere is calculated by using equation A.1. Window one is situated behind the center of the sphere and window two is situated in the freestream (see figure A.1).

$$r_k = \frac{\sum_{i=1}^{N-k} (Y_i - \bar{Y})(Y_{i+k} - \bar{Y})}{\sum_{i=1}^{N} (Y_i - \bar{Y})^2} \tag{A.1}$$

The autocorrelation is calculated from $Z/D = 5$ till $Z/D = 8$ since this is the region that will be used for drag calculations. The red horizontal line displayed in the two left plots in figure A.1 correspond to the 95% confidence band. Samples are said to be uncorrelated when the autocorrelation coefficient falls below this value. It is seen that, in the region with high velocity fluctuations, two samples become uncorrelated after 40 lags, which in this case is equal to one diameter of the sphere. Per velocity set, the drag was computed at stations one diameter apart, respectively at $Z/D = 5$, $Z/D = 6$ and $Z/D = 7$. By over-sampling, the amount of samples is thus increased from 60 to 180 per velocity set.

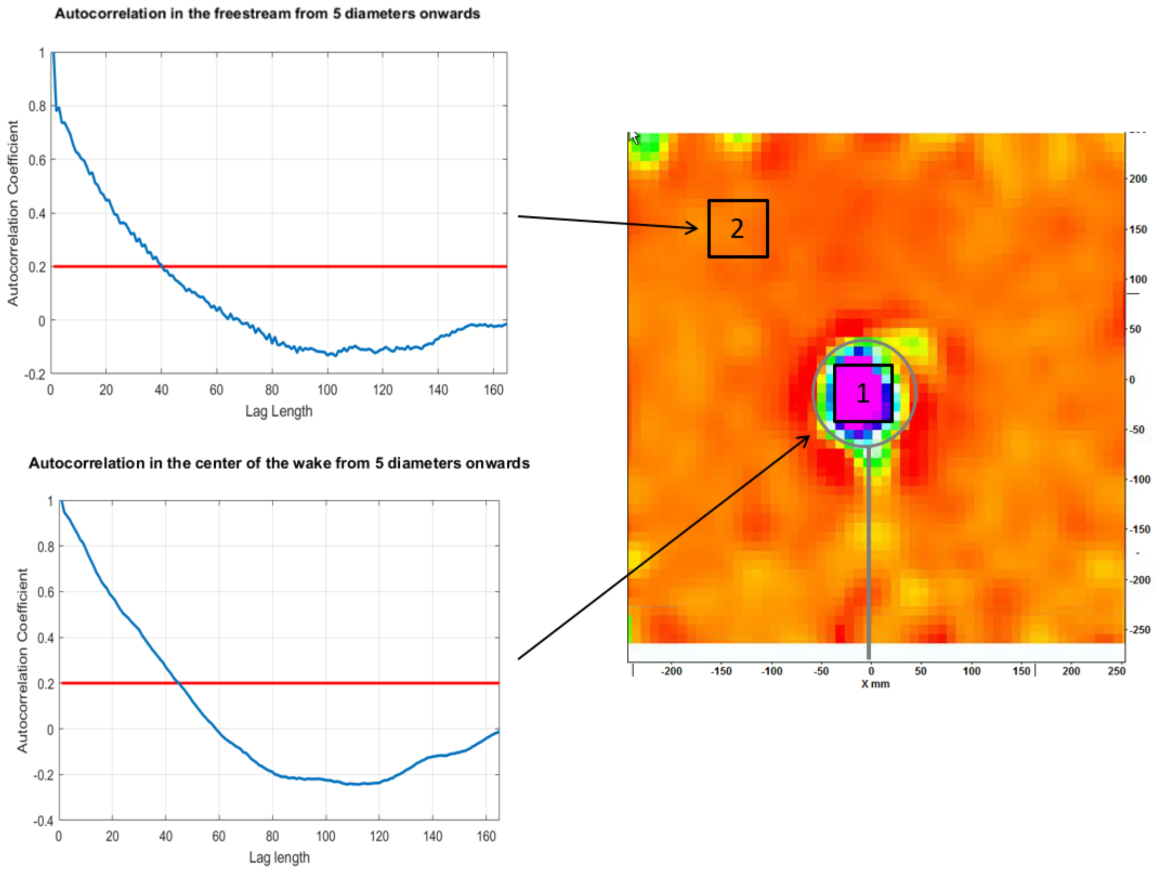

Figure A.1: Autocorrelation function of the streamwise velocity in a 9x9 window at two locations in the wake. Velocity of the sphere is 1.318m/s